

**RL-TR-95-109**  
**Final Technical Report**  
**June 1995**



# **OPTIMIZATION AND TESTING OF THE MULTICHANNEL ADAPTIVE OPTICAL PROCESSOR**

**Dynetics, Inc.**

**R.J. Berinato, M.C. Zari, M.C. Budge, Jr.,  
and K.O. Williams**



*APPROVED FOR PUBLIC RELEASE; DISTRIBUTION UNLIMITED.*

**19950927 043**

**DTIC QUALITY INSPECTED 5**

**Rome Laboratory  
Air Force Materiel Command  
Griffiss Air Force Base, New York**

This report has been reviewed by the Rome Laboratory Public Affairs Office (PA) and is releasable to the National Technical Information Service (NTIS). At NTIS it will be releasable to the general public, including foreign nations.

RL-TR-95-109 has been reviewed and is approved for publication.

APPROVED: *Michael E. Turbyfill*

MICHAEL E. TURBYFILL, 1LT, USAF  
Project Engineer

FOR THE COMMANDER:

*Donald W. Hanson*

DONALD W. HANSON  
Director of Surveillance & Photonics

If your address has changed or if you wish to be removed from the Rome Laboratory mailing list, or if the addressee is no longer employed by your organization, please notify RL (OCPC) Griffiss AFB NY 13441. This will assist us in maintaining a current mailing list.

Do not return copies of this report unless contractual obligations or notices on a specific document require that it be returned.

# REPORT DOCUMENTATION PAGE

Form Approved  
OMB No. 0704-0188

Public reporting burden for this collection of information is estimated to average 1 hour per response, including the time for reviewing instructions, searching existing data sources, gathering and maintaining the data needed, and completing and reviewing the collection of information. Send comments regarding this burden estimate or any other aspect of this collection of information, including suggestions for reducing this burden, to Washington Headquarters Services, Directorate for Information Operations and Reports, 1215 Jefferson Davis Highway, Suite 1204, Arlington, VA 22202-4302, and to the Office of Management and Budget, Paperwork Reduction Project (0704-0188), Washington, DC 20503.

1. AGENCY USE ONLY (Leave Blank)		2. REPORT DATE June 1995		3. REPORT TYPE AND DATES COVERED Final Dec 93 - Dec 94	
4. TITLE AND SUBTITLE OPTIMIZATION AND TESTING OF THE MULTICHANNEL ADAPTIVE OPTICAL PROCESSOR				5. FUNDING NUMBERS C - F30602-94-C-0020 PE - 62702F PR - 4600 TA - P1 WU - PY	
6. AUTHOR(S) R.J. Berinato, M.C. Zari, M.C. Budge, Jr., and K.O. Williams					
7. PERFORMING ORGANIZATION NAME(S) AND ADDRESS(ES) Dynerics, Inc. P.O. Drawer B Huntsville AL 35814-5050				8. PERFORMING ORGANIZATION REPORT NUMBER N/A	
9. SPONSORING/MONITORING AGENCY NAME(S) AND ADDRESS(ES) Rome Laboratory (OCPC) 25 Electronic Pky Griffiss AFB NY 13441-4515				10. SPONSORING/MONITORING AGENCY REPORT NUMBER RL-TR-95-109	
11. SUPPLEMENTARY NOTES Rome Laboratory Project Engineer: Michael E. Turbyfill, 1LT, USAF/OCPC/ (315) 330-3147					
12a. DISTRIBUTION/AVAILABILITY STATEMENT Approved for public release; distribution unlimited.				12b. DISTRIBUTION CODE	
13. ABSTRACT (Maximum 200 words)  This final report documents the continued design, hardware implementation, and testing of an acousto-optic (AO) multichannel adaptive optical processor (MADOP) for application to the cancellation of multipath jamming interference in advance surveillance applications. The work described in this report was performed for the Photonics Center at Rome Laboratory (RL) and represents the third year of Dynerics support on this project. The key program objective of this effort was the integration and testing of the MADOP hardware with the C-band radar testbed at the RL Surveillance and Photonics Directorate. To meet this objective, a number of improvements were made to the MADOP hardware and software, and laboratory testing was performed to ensure correct operation of the system. The successful integration of the MADOP with the C-band radar testbed was achieved, and testing of jammer cancellation in a number of configurations was performed. Performance results included 30-dB cancellation of narrowband tone jammers and 15- to 20-dB cancellation of wideband (8-MHz) noise jammers.					
14. SUBJECT TERMS  Adaptive processing, Acousto-optics, Optical signal processing				15. NUMBER OF PAGES 114	
				16. PRICE CODE	
17. SECURITY CLASSIFICATION OF REPORT UNCLASSIFIED	18. SECURITY CLASSIFICATION OF THIS PAGE UNCLASSIFIED	19. SECURITY CLASSIFICATION OF ABSTRACT UNCLASSIFIED	20. LIMITATION OF ABSTRACT UL		

## TABLE OF CONTENTS

	<u>Page</u>
1. INTRODUCTION.....	1-1
2. MADOP ALGORITHM OVERVIEW .....	2-1
2.1 PROBLEM DEFINITION.....	2-1
2.2 ADAPTIVE CANCELLATION ALGORITHM .....	2-4
2.3 MULTIPATH CONSIDERATIONS.....	2-6
3. MADOP HARDWARE CONFIGURATION .....	3-1
3.1 OVERVIEW OF THE ARCHITECTURE .....	3-1
3.2 TIME-INTEGRATING CORRELATOR FOR WEIGHT FUNCTION CALCULATION.....	3-1
3.3 AOTDL FILTER .....	3-12
3.3.1 Onsite Support Period One.....	3-12
3.3.2 Onsite Support Period Two .....	3-24
3.3.3 Onsite Support Period Three.....	3-25
3.4 SINGLE-LOOP ELECTRONIC CANCELLER.....	3-26
3.5 DIGITAL COMPUTER INTERFACE .....	3-36
4. MADOP SYSTEM TESTING.....	4-1
4.1 LABORATORY TESTING.....	4-1
4.1.1 Onsite Support Period One.....	4-1
4.1.2 Onsite Support Period Two .....	4-6
4.2 INTEGRATION WITH THE C-BAND RADAR TESTBED.....	4-12
4.3 C-BAND RADAR TESTBED MADOP TESTING .....	4-20
5. CONCLUSIONS AND RECOMMENDATIONS.....	5-1
5.1 CONCEPT EVALUATION IN REALISTIC JAMMER SCENARIOS.....	5-1
5.2 MADOP HARDWARE IMPROVEMENTS.....	5-1
5.3 FURTHER TESTING OF THE MADOP IN A PHASED ARRAY RADAR .....	5-2
APPENDIX A. LISTING OF DATAPLOT MATLAB PROGRAM FOR CORRELATION TESTING .....	A-1
APPENDIX B. MATLAB SIMULATION OF THE ELECTRONIC CANCELLER.....	B-1
REFERENCES .....	R-1

## LIST OF ILLUSTRATIONS

<u>Figure</u>	<u>Title</u>	<u>Page</u>
2-1	Two-Dimensional Operational Scenario for MADOP.....	2-2
2-2	Surveillance Radar Simplified Schematic With Adaptive IF Processing .....	2-3
2-3	Classical Multichannel LMS Adaptive Filter .....	2-5
2-4	MADOP Configuration for Implementing an IIR Filter .....	2-11
3-1	MADOP System Layout for Two Channels.....	3-2
3-2	Range Window Verification of 3- $\mu$ s Aperture.....	3-2
3-3	Window Uniformity: Linear Array Output.....	3-4
3-4	Window Uniformity: 2-D Camera Output.....	3-4
3-5	Range Window Centering Using 10-MHz Noise Inputs .....	3-5
3-6	Dynamic Range Test Signal Generation Layout .....	3-5
3-7	Dynamic Range Tests.....	3-6
3-8	Representative Detector Output.....	3-8
3-9	Spectral Content of Detector Output.....	3-8
3-10	Bandpass Filter Placed Around Wideband (Desired) Information .....	3-9
3-11	Correlation Output After Filtering.....	3-9
3-12	8-MHz Jammer Correlation (Receive Mode Only) .....	3-11
3-13	8-MHz Jammer Correlation (T/R Switching Mode) .....	3-11
3-14	8-MHz Correlation With T/R Noise .....	3-13
3-15	Spectrum of CCPD Output .....	3-13
3-16	Single A/O Cell T/R Noise .....	3-14
3-17	Single AO Cell T/R Noise Spectrum .....	3-14
3-18	Filtered T/R Noise.....	3-15
3-19	T/R Noise After Filtering .....	3-15
3-20	Filtered Correlation Spectrum (With T/R Contributions).....	3-16
3-21	Filtered Correlation (With T/R Contributions) .....	3-16
3-22	Anamorphic Lens Arrangement.....	3-18

## LIST OF ILLUSTRATIONS (Continued)

<u>Figure</u>	<u>Title</u>	<u>Page</u>
3-23	AOTDL Frequency Response: Onsite Support Period 1.....	3-22
3-24	AOTDL Frequency Response for 25-MHz Span.....	3-22
3-25	AOTDL Output for Single Tone Input: AOSLM Frequency 1.....	3-23
3-26	AOTDL Output for Single Tone Input: AOSLM Frequency 2.....	3-23
3-27	AOSLM Optical Interference Frequency Response.....	3-24
3-28	AOTDL Frequency Response: Onsite Support Period 2.....	3-25
3-29	Frequency Response From ZSC-1-2 Through 5.0- $\mu$ s Delay Through AMP 20502 Through AOTDL.....	3-26
3-30	Original MADOP Configuration.....	3-27
3-31	Electronic Canceller Configuration.....	3-28
3-32	MADOP With Electronic Canceller.....	3-29
3-33	Response of Electronic Canceller for a Phase Difference of 100°.....	3-30
3-34	Response of Electronic Canceller for a Phase Difference of 80°.....	3-31
3-35	Response of Electronic Canceller for a Phase Difference of 40°.....	3-32
3-36	Effects of Saturation on Electronic Canceller Performance.....	3-33
3-37	Phase Errors of Vector Modulator: In-Phase Control Voltage = -1 V.....	3-34
3-38	Phase Errors of Vector Modulator: In-Phase Control Voltage = -5 V.....	3-34
3-39	Phase Errors of Vector Modulator: In-Phase Control Voltage = -10 V.....	3-35
3-40	Schematic Diagram of dc Amplifier With 33 dB of Gain.....	3-35
4-1	Tone Cancellation, Signals Generated at AOTDL.....	4-2
4-2	Tone Cancellation, Signals Generated at AOTDL, Reduced Tap Power.....	4-2
4-3	DSB-SC Spectrum.....	4-3
4-4	DSB-SC Cancellation, Signals Generated at AOTDL.....	4-3
4-5	500-ns Cancelled Pulse, Signals Generated at Correlator.....	4-4
4-6	Reference Pulse.....	4-4
4-7	Reference Pulse Spectrum.....	4-5
4-8	Cancelled Pulse Spectrum.....	4-5

## **LIST OF ILLUSTRATIONS (Continued)**

<b><u>Figure</u></b>	<b><u>Title</u></b>	<b><u>Page</u></b>
4-9	MADOP Configuration for Initial Testing During Onsite Support Period 2.....	4-7
4-10	0.6-ms Pulse Cancellation.....	4-8
4-11	1.2-ms Pulse Cancellation.....	4-8
4-12	80-MHz Tone Cancellation.....	4-9
4-13	Setup With Tektronix AM4001 Differential Amp.....	4-10
4-14	Main Channel Signal Containing Jammer at 73.25 MHz and Target Return at 80.5 MHz .....	4-11
4-15	Error Signal Showing SJR ~25 dB .....	4-11
4-16	Reference Input for a 2-MHz Pulse.....	4-13
4-17	Cancelled Signal for a 2-MHz Pulse .....	4-13
4-18	Reference Signal Input Wideband Noise.....	4-14
4-19	Cancelled Signal for Input Wideband Noise.....	4-14
4-20	Reference Input for a 100-ns Pulse, 500-ns PRI .....	4-15
4-21	Cancelled Signal for Input 100-ns Pulse.....	4-15
4-22	Modified Architecture to Place Gain in dc Circuit Prior to Integrators.....	4-16
4-23	Reference Single-Tone Signal .....	4-17
4-24	Cancelled Signal for Input Single Tone With dc Gain in System Yielding 36-dB Cancellation.....	4-17
4-25	C-Band Array Structure.....	4-18
4-26	C-Band Receiver Configuration .....	4-19
4-27	Remote Signal Source Configuration .....	4-20
4-28	MADOP Integration With C-Band Test Radar .....	4-21
4-29	MADOP AO Subsystems at the C-Band Radar Test Facility.....	4-21
4-30	MADOP Configuration Used During First Three Sets of Tests .....	4-22
4-31	Results From the First Set of C-Band Radar Tests - Tone Jammer, Pulse Target, Open Loop Control Via HP 83623A.....	4-24
4-32	Results From the Second Set of C-Band Radar Tests - Noise Jammer, No Target, Closed Loop Through HP 83623A .....	4-26

# LIST OF ILLUSTRATIONS (Concluded)

<u>Figure</u>	<u>Title</u>	<u>Page</u>
4-33	Results From the Third Set of C-Band Radar Tests - Tone Jammer, No Target, Closed Loop Through Synthesizer in Computer.....	4-27
4-34	Results From the Third Set of C-Band Radar Tests - Noise Jammer, No Target, Closed Loop Through Synthesizer in Computer.....	4-28
4-35	MADOP Configuration Used During Fourth Set of Tests.....	4-30
4-36	C-Band Radar Azimuth Antenna Patterns.....	4-31
4-37	Results From the Fourth Set of C-Band Radar Tests - Tone Jammer, Tone Target, Both Signals From C-Band Radar.....	4-33
4-38	Results From the Fourth Set of C-Band Radar Tests - Noise Jammer, Pulse Target, Both Signals From C-Band Radar.....	4-35

Accession For	
NTIS CRA&I	<input checked="" type="checkbox"/>
DTIC TAB	<input type="checkbox"/>
Unannounced	<input type="checkbox"/>
Justification .....	
By .....	
Distribution / .....	
Availability Codes	
Dist	Avail and / or Special
A-1	

## LIST OF TABLES

<u>Table</u>	<u>Title</u>	<u>Page</u>
2-1	Feasibility Demonstration Goals.....	2-4
3-1	SNR Calculations as Function of Data File, Feature Implementation, and Data Collection Optimization.....	3-10
3-2	AOTDL Filter Performance Measurements: Onsite Support Period One .....	3-21

## LIST OF ABBREVIATIONS

2-D	two-dimensional
ac	alternate current
A/D	analog-to-digital
AFG	arbitrary function generator
AO	acousto-optic
AOSLM	acousto-optic spatial light modulator
AOTDL	acousto-optic tapped delay line
BAW	bulk acoustic wave
BW	bandwidth
CCD	charged coupled device
CCPD	charged coupled photo detector
CW	continuous wave
dc	direct current
DSB-SC	double-sideband suppressed-carrier
ESE	Expert in Science and Engineering
FFT	fast Fourier transform
FIR	finite impulse response
IF	intermediate frequency
IFFT	inverse fast Fourier transform
I&Q	In-phase and Quadrature
IIR	infinite impulse response
LMS	least mean squared
MADOP	multichannel adaptive optical processor
MSE	mean-squared-error
PC	personal computer
RF	radio frequency
RL	Rome Laboratory
S/J	signal-to-jammer
S/N	signal-to-noise
SNR	signal-to-noise ratio
T/R	transmit/receive
USAF	United States Air Force
VCSEL	vertical cavity surface emitting laser
VSWR	voltage standing wave ratio

## Units of Measure

dB	decibels
dB <sub>i</sub>	decibels above an isotropic radiator
dB <sub>m</sub>	decibels above, or referred to, one milliwatt
°, deg	degrees
ft	feet
Hz	hertz
kHz	kilohertz
km	kilometers
kW	kilowatts
MHz	megahertz
mm	millimeters
ms	milliseconds
mW	milliwatts
μs	microseconds
nm	nanometers
ns	nanoseconds
W	ohms
%	percent
s	seconds
V	volts

## **1. INTRODUCTION**

This final report documents the continued design, hardware implementation, and testing of an acousto-optic (AO) multichannel adaptive optical processor (MADOP) for application to the cancellation of multipath jamming interference in advanced surveillance applications. This Expert in Science and Engineering (ESE) effort is a continuation of an ongoing program within the Rome Laboratory (RL) Photonics Center (References 1 through 7). Approximately half of the Dynetics effort was performed onsite at RL, Griffiss AFB, NY. This work was accomplished in conjunction with Photonics Center personnel: Capt. H. Andrews, Lt. M. Turbyfill, Lt. J. Lutsko, and E. Walge under the in-house Project 4600P107. All the work described in this report was performed under ESE Contract F30602-94-C-0020 during the period of 29 December 1993 to 28 December 1994.

The U.S. Air Force (USAF) has a requirement to effectively operate surveillance radars in the presence of hostile jammers and other interference sources, including multipath. The signal environment of the future is becoming increasingly dense, including the appearance of greater numbers of wideband emitters that add to the complexity of the problem. Meeting this requirement demands a capability to cancel this interference in order to improve target detectability and track performance. Optical signal processing technology offers a possible solution to this demanding signal cancellation problem. This advanced technology has been pursued within the RL Photonics Center to address such USAF problems. The MADOP system has been part of this technology development over the past 5 years and appears to offer an attractive solution to future USAF surveillance missions in the presence of complex interference environments.

The key program objective of this effort was the integration and testing of the MADOP hardware with the C-band radar testbed at the RL Surveillance and Photonics Directorate. To meet this objective, three activities were pursued: 1) the optimization of the closed-loop MADOP performance, 2) the evaluation and improvement of electronic interfaces, and 3) the testing of the MADOP in the C-band radar testbed. The optimization of the closed-loop MADOP performance included:

1. Further mechanical stabilization of the optical subsystems through reduction of the size of the systems and design and integration of more rugged mounts;
2. Further optimization and testing of a single-loop electronic canceller that follows the AO tapped delay line (AOTDL) filter in the architecture;
3. The integration of a slow-shear TeO<sub>2</sub> AO device as the AO spatial light modulator (AOSLM) to reduce the size of the system and increase the cancellation delay window; and

4. Further packaging and organization of the radio frequency (RF) electronic subsystem and associated signal generators.

The evaluation and improvement of the electronic interfaces included further development of the algorithms used to adaptively estimate the required tap weights, simulation of these algorithms, and testing of the algorithms during the laboratory and C-band radar testbed experiments. The testing of the MADOP in the C-band radar testbed included:

1. Test plan development;
2. Integration of the systems at the 80-MHz intermediate frequency (IF) of the C-band radar testbed; and
3. Performing narrowband testing and wideband testing using a variety of signal and jammer configurations.

Test plan development was preliminary due to the unknowns involved with the C-band radar testbed. This preliminary plan was revised a number of times during the testing; hence, it was not an effective tool. It is anticipated that the next testing activity will greatly benefit from a detailed test plan that is created using the knowledge gained in this initial phase of C-band testing.

The key program objective was met during this program by successfully integrating the MADOP with the C-band radar testbed at the 80-MHz system IF (over the 8-MHz testbed bandwidth), and testing the cancellation performance in several configurations using narrowband tone and wideband noise jammers. Performance results included 30-dB cancellation of narrowband tone jammers and 15- to 20-dB cancellation of wideband (8-MHz) noise jammers. This integration and testing represents a significant milestone in the long-term development of the MADOP system. This success has motivated the continuation of the project to address further C-band radar testbed experimentation as well as possible integration with the RL S-band radar system with potential cueing from the L-band search radar.

This technical report is organized as follows. After this introduction, the adaptive cancellation algorithm implemented by the MADOP hardware is described in Section 2, with particular emphasis on some of the challenges to be faced with testing in more complex signal environments. Section 3 provides an overview of the MADOP hardware configuration and details the improvements made to both the optical and electronic subsystems. Laboratory testing of the MADOP system and integrated testing with the C-band radar testbed are then addressed in Section 4, followed by conclusions and recommendations in Section 5. Two MATLAB simulations are provided in Appendixes A and B.

## 2. MADOP ALGORITHM OVERVIEW

The MADOP has been designed to achieve time-domain cancellation of multiple wideband interferers. As designed, the system will be able to cancel four independent interference sources, with each source having up to a 10-MHz bandwidth. The initial implementation emphasizes two channels. The key advantage of our optical approach over the current state-of-the-art in digital and analog electronic implementations is the ability to cancel wideband interference by using multiple tap weights per channel. The fact that the canceller employs time-domain cancellation also allows considerable latitude in the separation between the main antenna and the auxiliary channel antennas. Furthermore, the ability to implement multiple tap weights in the time domain canceller provides the potential for jammer cancellation in the presence of multipath in the main and auxiliary channels. The discussion below contains an overview of the MADOP and its implementation within a radar. The issue of cancellation in the presence of multipath is also addressed.

### 2.1 PROBLEM DEFINITION

*Figure 2-1* presents an illustrative summary of the scenario being addressed. In this figure, two independent interference sources,  $n_1(t)$  and  $n_2(t)$ , having spectral content in the radar system passband, contaminate the directional main antenna target return,  $s(t)$ , through the sidelobes. The multipath versions of the two interference sources also contribute a significant noise term to the main channel signal resulting in the reception of :

$$d(t) = s(t) + \sum_{n=1}^N a_{1n} n_1(t - \tau_{1n}) + \sum_{m=1}^M a_{2m} n_2(t - \tau_{2m}) \quad (2-1)$$

where  $a_{1n}$  and  $a_{2m}$  represent relative attenuations due to multipath losses together with antenna sidelobe gain relative to mainlobe gain, and  $\tau_{1n}$  and  $\tau_{2m}$  represent the signal delays. The direct-path interference is given for  $n = 1$  and  $m = 1$ . It is assumed that the interference is on the order of, or much larger than, the target return,  $s(t)$ , resulting in a low signal-to-jammer (S/J) ratio in the main antenna. The two auxiliary antennas receive the interference, but the target return entering these antennas is negligible because of the low main-channel S/J assumption. Thus, the two auxiliary antennas receive the signals:

$$\begin{aligned}
N_1(t) &= \sum_{n=N+1}^{2N} a_{1n} n_1(t - \tau_{1n}) + \sum_{m=M+1}^{2M} a_{2m} n_2(t - \tau_{2m}), \\
N_2(t) &= \sum_{n=2N+1}^{3N} a_{1n} n_1(t - \tau_{1n}) + \sum_{m=2M+1}^{3M} a_{2m} n_2(t - \tau_{2m}).
\end{aligned} \tag{2-2}$$

In addition to these correlated noises, uncorrelated receiver noise is present at each antenna.

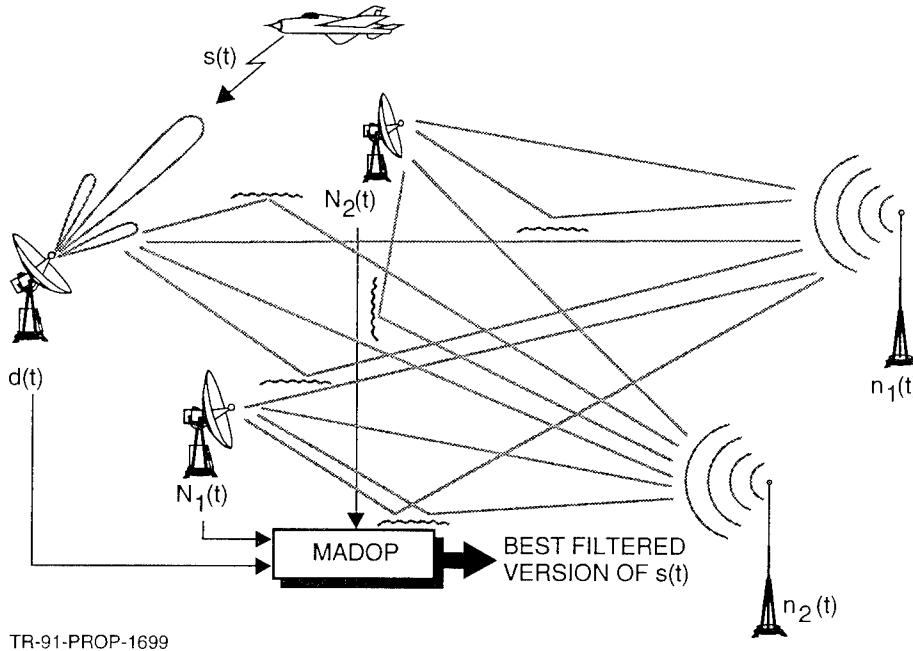


**Figure 2-1. Two-Dimensional Operational Scenario for MADOP**

**Figure 2-2** shows a simplified block diagram of a typical surveillance radar that may benefit from the MADOP. This diagram is not intended to represent a specific radar system. The MADOP is shown in the radar IF after downconversion from the RF carrier (3 or 10 GHz for example). The waveform generator provides the signal to be transmitted and also provides the matched filter to the signal processor to allow for pulse compression and pulse integration/Doppler filtering. The antenna system, whether phases-array or dish, forms a beam (or multiple independent beams, as possible with a phased-array antenna) that illuminates the target in the presence of interference. The target reflection, contaminated by interference, is received in the main channel, while the interference is also received in auxiliary antenna channels (which can be portions of a single phases array). All signals are downconverted to the IF and input into the MADOP. The output of the MADOP is the desired signal with the interference suppressed. This signal then enters the coherent pulse compression and Doppler filtering system, which is often implemented

digitally following analog-to-digital (A/D) conversion of in-phase and quadrature (I&Q) channels. After this signal processing, target detection takes place using some form of constant false alarm rate processing. The data processor performs such operations as target tracking, beam scheduling, system control, and interface to the display.

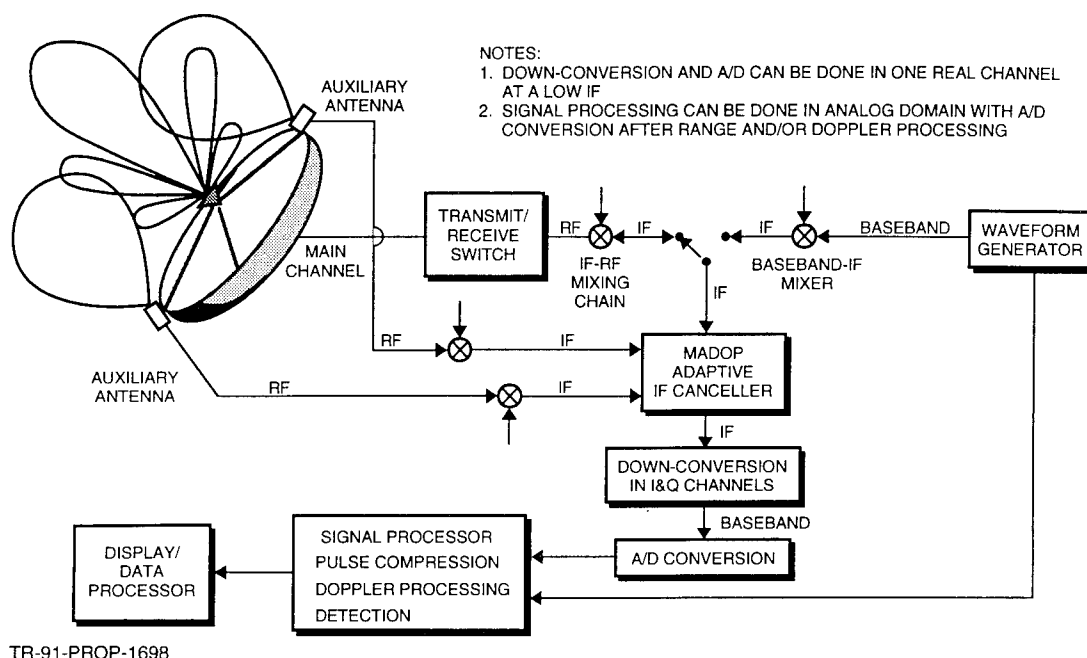


**Figure 2-2. Surveillance Radar Simplified Schematic With Adaptive IF Processing**

As stated above, the goal of the adaptive processor is to react to the interference environment in such a way that the main antenna interference is cancelled, resulting in a satisfactory S/J for further processing. The algorithm for achieving this objective is described below. The goals for this feasibility demonstration program, as coordinated with personnel in the Surveillance Technology Division of the Surveillance and Photonics Directorate (OCTS), are shown in **Table 2-1**. It is recognized that although the loop lock time (time to reach steady state) is critical in system applications (500  $\mu$ s is desirable), the personal computer (PC) interface in the digital subsystem used in the current implementation makes practical loop lock times unachievable. The development of real-time, special-purpose digital interfaces will greatly increase system speed.

**Table 2-1. Feasibility Demonstration Goals**

System Bandwidth (MHz)	10
Number of Interference Sources	4 (initial demo will accommodate 2)
Maximum Multipath Delay ( $\mu$ s)	5 (corresponds to 1.5-km differential path)
Interference Cancellation Ratio (dB)	30
Number of Multipath Delays	>4
Loop Lock Time (ms)	5
Processor IF (MHz)	80

## 2.2 ADAPTIVE CANCELLATION ALGORITHM

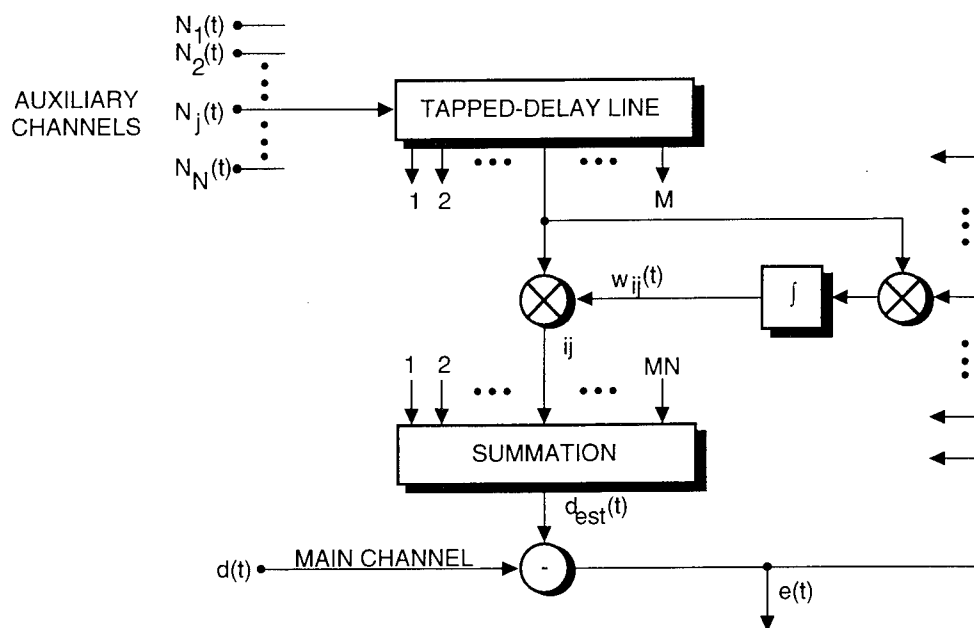
The standard multidimensional tapped delay line implementation of the least mean squared (LMS) algorithm is shown in **Figure 2-3**. Note that the LMS algorithm is based on steepest descent techniques, where the weight function is updated in the direction opposite the gradient at the current weight value. This will cause the weights to move in such a way as to reduce the mean-squared-error (MSE) along the steepest gradient. The input signals from the auxiliary antennas,  $N_i(t)$ , are convolved with the weight functions  $w_i(t; \tau)$ , which are functions of time,  $t$ , and delay,  $\tau$ , to yield an estimate,  $d_{est}(t)$ , of the main channel signal:

$$d_{est}(t) = \sum_{j=1}^P \int_{-\frac{T_a}{2}}^{\frac{T_a}{2}} w_i(t; \tau) N_i(t - \tau) d\tau \quad (2-3)$$

where  $P$  is the number of auxiliary antennas and  $T_a$  is the length of each tapped delay line. This estimate is subtracted from the main channel signal,  $d(t)$ , to form an error signal,  $e(t)$ . The weights are then updated according to the degree of correlation between this error and the auxiliary channel inputs. The  $i^{th}$  weight function is represented mathematically as:

$$w_i(t; \tau) = w_i(0; \tau) + \int_0^t \alpha(t) e(t) N_i^*(t - \tau) dt \quad (2-4)$$

where  $\alpha(t)$  is a time-varying (in general) acceleration parameter. As this process continues in time, the adaptively changing weights converge to a steady-state solution (if the signal environment is stationary). This cancels the interference in the main channel, which equivalently yields the minimum MSE and maximum output S/J ratio.



TR-91-PROP-1700

**Figure 2-3. Classical Multichannel LMS Adaptive Filter**

The classical LMS algorithm performs a weight update at each point in time. If a discrete algorithm is employed, the weight update is achieved at each time step, which must be at a frequency greater than twice the widest bandwidth to be processed. Thus, for 10-MHz bandwidth signals, the time step and weight update occur every 50 ns. **Figure 2-3** implies that taps must be positioned every 50 ns if discrete taps are employed. The integration shown in Equation 2-4 occurs over the entire observation period, resulting in a continuous weight update. In addition, as the weights are updated, the error continues to be reduced, which then feeds back into the weight calculation integration.

In the current implementation of the MADOP, the weight computations are performed by a digital computer, which means that the weights cannot be updated at the rate indicated above. Because of this, an alternate to the classical LMS algorithm is currently implemented in the MADOP. For our system, the correlation is performed, in the AO time-integrating correlator, over a longer window of time,  $T$ , during which the weight functions do not change. This time window has typically been greater than 2 ms. After the correlation has been obtained, the results are used to update the weight functions, a process that is performed in the digital computer and takes an additional increment of time,  $t_u$ . In the current implementation of the MADOP,  $t_u$  is approximately 1 s.

Because of the longer correlation time the weights computed in a single step are very close to the final weights that would result after several iterations of the classical LMS algorithm. As a result, it is no longer necessary to use the error signal ( $e(t)$  in **Figure 2-3**) to update the weights. Instead, the weights can be computed by directly correlating the main and auxiliary channel signals. This difference is similar to the two adaptive beamforming approaches: 1) iterative schemes that converge to the desired result, and 2) direct matrix inversion of the correlation/covariance matrix that is formed through integration of the received signals over some relatively long time window. This longer integration is the basis for what has been implemented in the current MADOP system.

The windowed algorithm described above is similar to the block adaptive filtering approach that has been increasingly researched in the digital adaptive filtering community (References 8 through 10). The primary motivation for this interest is the compatibility of block routines with fast convolution algorithms that employ fast Fourier transforms (FFTs). In these adaptive filters, the weights are updated based on a window of data, rather than at each time step. An interesting result related to these block routines is that the convergence generally proceeds much faster than for the classical LMS routine due to the reduction in the gradient estimate noise. Also, highly correlated input data, resulting in a high correlation matrix condition number and generally slow convergence, are better processed through block techniques.

### 2.3 MULTIPATH CONSIDERATIONS

The cancellation of interference containing multipath returns has been very difficult for conventional sidelobe cancellers because the cancellation is based on adjusting the amplitude and phase of the auxiliary channel signal and subtracting it from the main channel signal. Such an approach does not allow a means of accounting for delays caused by the multipath.

In contrast to conventional sidelobe cancellers, the MADOP effects cancellation by delaying and adjusting the amplitude of the auxiliary channel signal and subtracting it from the main channel signal. Furthermore, the MADOP can apply multiple delays and amplitude weights to cancel the multiple returns caused by multipath.

As an example, let the signal in the auxiliary channel be

$$N_1(t) = bn(t) \tag{2-5}$$

where  $n(t)$  is the interference signal and  $b$  accounts for the auxiliary channel antenna pattern and receiver characteristics. The range delay of  $n(t)$  and its delay through the receiver are set to zero without loss of generality for this analysis.

Let the main channel signal be given by

$$d(t) = s(t) + a_d n(t - \tau_d) + a_m n(t - \tau_m) \quad (2-6)$$

where  $s(t)$  is the desired signal. The two interference terms represent the direct path ( $d$  subscript) and the multipath ( $m$  subscript) components.  $a_i$  is the relative amplitude, and  $\tau_i$  is the delay relative to the auxiliary channel interference signal.

For these main and auxiliary channel signals the AOTDL of the MADOP would ideally be configured (by the weight computation algorithm) to have two delays with weights of  $a_d/b$  and  $a_m/b$ . The result would be a cancellation signal of

$$\begin{aligned} d_{\text{est}}(t) &= a_d/b N_1(t - \tau_d) + a_m/b N_1(t - \tau_m) \\ &= a_d n(t - \tau_d) + a_m n(t - \tau_m). \end{aligned} \quad (2-7)$$

The resultant output of the MADOP would be

$$e(t) = d(t) - d_{\text{est}}(t) = s(t). \quad (2-8)$$

The key point above is the ability of the AOTDL to implement multiple time delays with multiple weights.

The above discussion was based on the premise that the main channel receives multipath returns while the auxiliary channel receives only direct path returns. A more realistic scenario involves the case where both the main and auxiliary channels receive multipath signals. In this case, the ability to cancel the interference signal becomes more questionable. However, given the ability of the AOTDL of the MADOP to implement multiple delays and weights, it still may be possible to effect significant interference cancellation.

To discuss how the MADOP might be configured to handle multipath signals in the main and auxiliary channels, we cast the above discussion in the sampled data domain and make use of z-transforms. In this context, let the auxiliary channel signal be

$$N_1(k) = b_d n(k - l_d) + b_m n(k - l_m) \quad (2-9)$$

and the main channel signal be

$$d(k) = s(k) + a_d n(k - k_d) + a_m n(k - k_m) = s(k) + N_m(k). \quad (2-10)$$

The MADOP implements the equation

$$e(k) = d(k) - w(k) * N_1(k) \quad (2-11)$$

where  $w(k)$  represents the delay and weighting characteristics of the AOTDL and  $*$  denotes convolution.

Substituting for  $d(k)$  results in

$$e(k) = s(k) + N_m(k) - w(k) * N_1(k). \quad (2-12)$$

Ideally, we want  $e(k) = s(k)$ , which leads to the requirement that

$$N_m(k) - w(k) * N_1(k) = 0. \quad (2-13)$$

The above says that we want to find  $w(k)$  such that the above equality is valid.

We can further examine the calculation of  $w(k)$  by transforming the above to the z-domain. Specifically we write Equation 2-13 in the z-domain as:

$$N_m(z) - W(z)N_1(z) = 0 \quad (2-14)$$

where  $N_m(z)$ ,  $W(z)$ , and  $N_1(z)$  are the z-transforms of  $N_m(k)$ ,  $w(k)$ , and  $N_1(k)$ , respectively.

With the above we conclude that the AOTDL delay and weighting needed to effect interference cancellation can be obtained as

$$W(z) = \frac{N_m(z)}{N_1(z)}. \quad (2-15)$$

This is an interesting result but is of little practical value since it requires knowledge of  $N_m(z)$  and  $N_1(z)$ . A more practical result can be obtained by multiplying Equation 2-14 by  $N_1^*(1/z)$  to yield

$$N_m(z)N_1^*(1/z) - W(z)N_1(z)N_1^*(1/z) = 0 \quad (2-16)$$

or

$$W(z) = \frac{N_m(z)N_1^*(1/z)}{N_1(z)N_1^*(1/z)}. \quad (2-17)$$

The act of multiplying  $N_m(z)$  and  $N_1(z)$  by  $N_1^*(1/z)$  represents a correlation of  $N_m(k)$  and  $N_1(k)$  with  $N_1(k)$ . The correlation of  $N_m(k)$  with  $N_1(k)$  is currently the operation performed by the AO time-integrating correlator of the MADOP. More specifically, the correlator performs the operation

$$\begin{aligned} d(k) \otimes N_1(k) &= [s(k) + N_m(k)] \otimes N_1(k) \\ &= s(k) \otimes N_1(k) + N_m(k) \otimes N_1(k) \\ &\approx N_m(k) \otimes N_1(k). \end{aligned} \quad (2-18)$$

The assumption that  $s(k) \otimes N_1(k) \approx 0$  is a basic assumption of the MADOP and is based on the fact that  $s(k)$  and  $N_1(k)$  are uncorrelated.

For the case where there is no multipath in the auxiliary channel and  $n(k)$  is wideband

$$N_1(k) \otimes N_1(k) \approx b^2 \delta(k) \quad (2-19)$$

and

$$N_1(z)N_1^*(1/z) = b^2. \quad (2-20)$$

With this,  $W(z)$  and  $w(k)$  become

$$W(z) = \frac{1}{b^2} N_m(z)N_1^*(1/z) \quad (2-21)$$

and

$$w(k) = \frac{1}{b^2} N_m(k) \otimes N_1(k) \approx \frac{1}{b^2} d(k) \otimes N_1(k). \quad (2-22)$$

The latter equation represents the weight calculation as a block LMS algorithm and is the form currently implemented in the MADOP.

$W(z)$  as given in Equation 2-21 is of the form

$$W(z) = \sum_m c_m z^{-l_m} \quad (2-23)$$

which means that the convolution of  $w(k)$  and  $d(k)$  can be performed in a finite impulse response (FIR) filter as is currently done in the AOTDL portion of the MADOP.

For the case where the interference in the main channel contains both direct and multipath signals, and the interference is wideband, the autocorrelation of  $N_1(k)$  yields

$$N_1(k) \otimes N_1(k) = \sum_n d_n \delta(k - k_n) \quad (2-24)$$

and, thus,

$$N_1(z)N_1^*(1/z) = \sum_n d_n z^{-k_n}. \quad (2-25)$$

This means that  $W(z)$  will not be of the simple form of Equation 2-23. Instead,  $W(z)$  will be the ratio of polynomials in  $z$ . That is,

$$W(z) = \frac{\sum_m c_m z^{-l_m}}{\sum_n d_n z^{-k_n}}. \quad (2-26)$$

The above form of  $W(z)$  implies that the convolution of  $d(k)$  and  $w(k)$  must be carried out by an infinite impulse response (IIR) filter. A method of implementing such a filter using AOTDLs was presented in the final report for the previous ESE effort (Reference 1).

A block diagram of a modified MADOP that would implement the above algorithm is contained in **Figure 2-4**. It differs from the current configuration by the addition of another AO time-integrating correlator to form the autocorrelation of  $N_1(t)$  and another AOTDL to implement the IIR filter.

The implementation of the MADOP indicated in **Figure 2-4** is considerably more complex than the original MADOP configuration. In addition, as indicated in Reference 1, there is a potential problem with the stability of the IIR filter. Because of this, this method of implementing the MADOP should be carefully investigated before it is pursued further. Preliminary investigations conducted during the previous ESE effort indicate that the original, adaptive LMS implementation of the MADOP may be able to compensate for multipath by providing an FIR approximation to the IIR filter. This is an area that warrants further investigation.

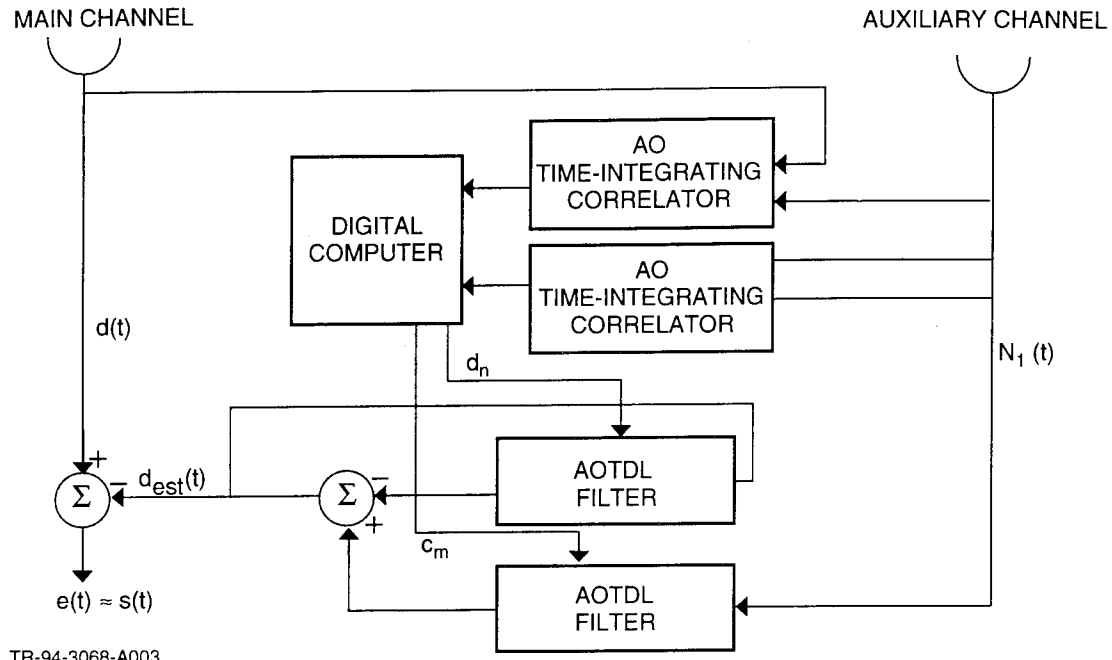


**Figure 2-4. MADOP Configuration for Implementing an IIR Filter**

### **3. MADOP HARDWARE CONFIGURATION**

During the performance of this effort, the optical and electronic subsystems of the MADOP were further developed and tested. Previous test results and detailed theoretical development are contained in References 1 and 2.

#### **3.1 OVERVIEW OF THE ARCHITECTURE**

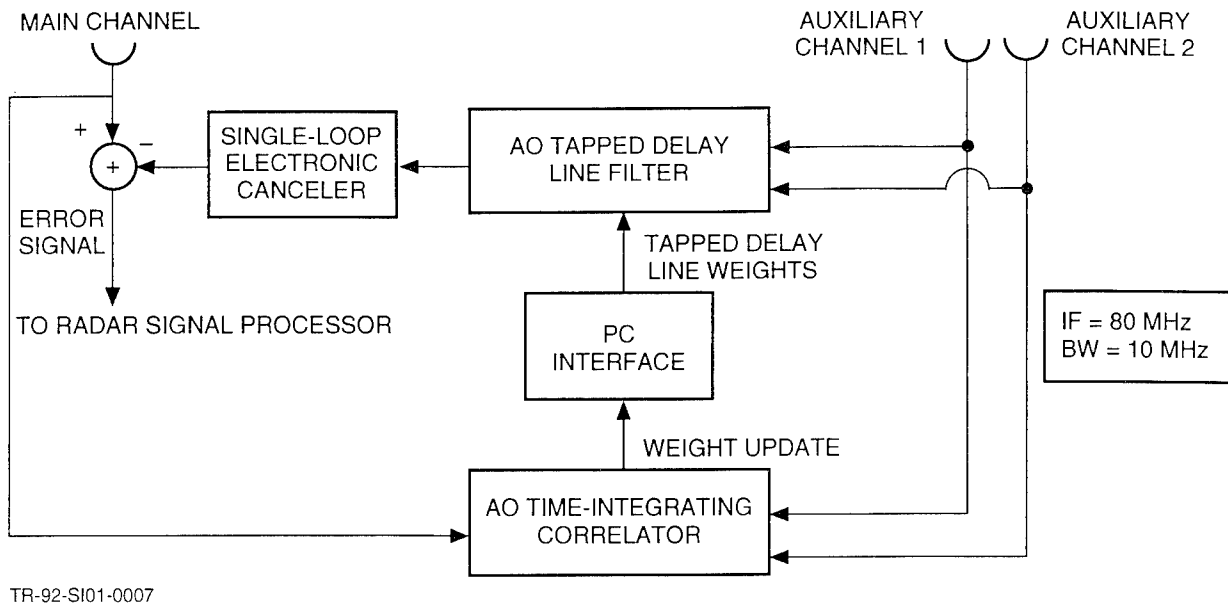
The MADOP subsystems and their relevant inputs and outputs are shown in *Figure 3-1*. Shown in this figure are two auxiliary antenna inputs together with the main channel received signal. The AO time-integrating correlator accepts the main channel signal and the auxiliary channel signals and forms the appropriate cross-correlations. This cross-correlation information contains the information needed to select, through the PC interface, the weights to be applied to the AOTDL filter. This AOTDL filter convolves the auxiliary channel inputs with the weights and sums the resultant channels to obtain an estimate for the jamming signal in the main channel. This was originally subtracted from the main channel to generate the error signal. After development of the system, it was noted that the system maintains a stable tap position relative to the envelope of the modulation, but relative to the 80-MHz IF there is phase drift. Therefore, the single-loop electronic canceller was fabricated and inserted into the system at the output of the AOTDL filter to, in effect, lock the carrier of the AOTDL filter output to the main channel signal to achieve effective cancellation.

Each of the following subsections will describe the further development and testing of the individual subsystems, namely the AO time-integrating correlator, the AOTDL filter, the single-loop electronic canceller circuit, and the PC interface.

#### **3.2 TIME-INTEGRATING CORRELATOR FOR WEIGHT FUNCTION CALCULATION**

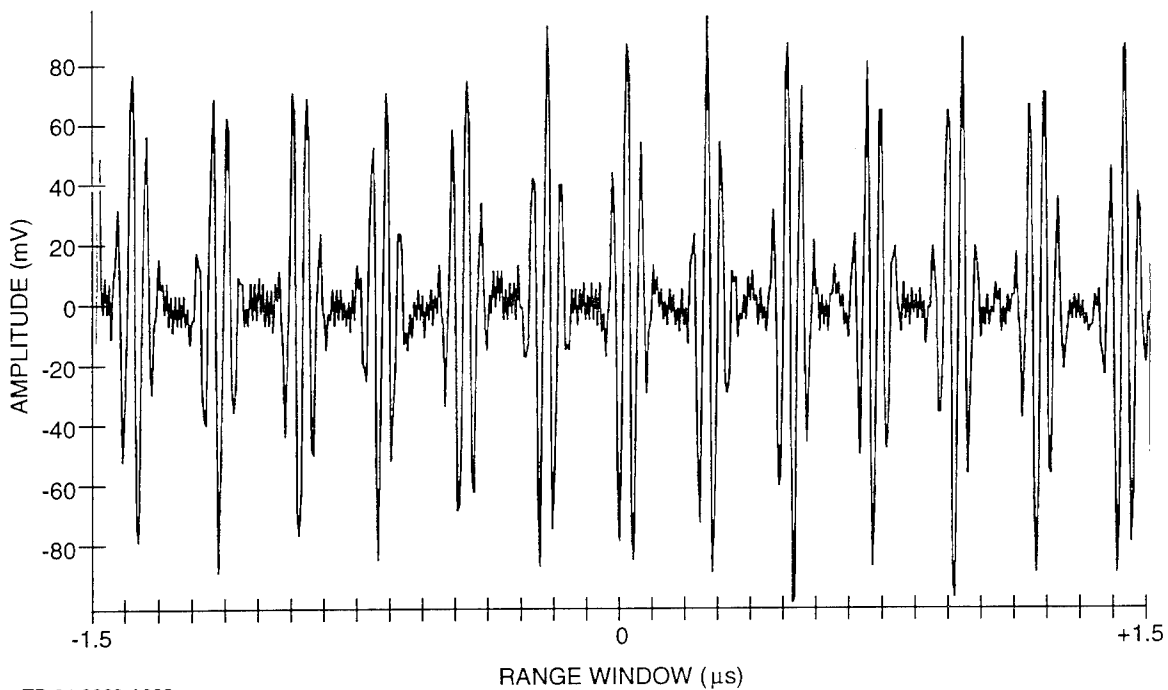
The work performed on the time-integrating correlator under this effort included optimization of correlation for laboratory testing of the MADOP system, transportation of the breadboard correlator system to the radar facility, recalibration of the correlator after transportation, and optimization of the correlator for MADOP testing with the radar.

Initial testing and optimization of the two-path time-integrating correlator was performed during the first onsite support trip. The multichannel AO cells were reinserted into the correlator and the two-path correlator was aligned. A 3- $\mu$ s correlation window was verified using a two-tone double-sideband suppressed-carrier (DSB-SC) modulation input to the AO cells, as described in References 1 and 2. A 2.16-MHz tone was DSB-SC modulated on an 80-MHz carrier. This results in 13 correlation peaks across the 3- $\mu$ s window, as shown in *Figure 3-2*.



TR-92-SI01-0007

**Figure 3-1. MADOP System Layout for Two Channels**



TR-94-3069-A003

**Figure 3-2. Range Window Verification of 3- $\mu$ s Aperture**

Adjustments in AO cell position and imaging/focusing lens positions were made to optimize the uniformity of the correlation across the range window. An 80-MHz tone was input to each AO cell, resulting in the spatial carrier correlating across the charged coupled photo detector (CCPD) array. **Figures 3-3 and 3-4** show the output from the linear CCPD array and a two-dimensional (2-D) charged coupled device (CCD) camera after range window uniformity optimization. Note that since it was decided that only a single channel is needed for the near-term radar demo, the second linear array was removed and replaced with the 2-D camera. The 2-D camera also aided initial AO cell and beam splitter alignment since spatial carrier fringe orientation is easily viewed in this format (as seen in **Figure 3-4**).

Correlation window centering was achieved through the use of a 10-MHz noise signal into the AO cells. The CCPD array was linearly translated along the AO aperture direction, until the correlation peak due to the noise was centered on the array. The alignment results are shown in **Figure 3-5** (output from the linear array).

Dynamic range test procedures have been revised to make full use of the detector dynamic range. The procedures are as follows:

1. Set bias = 0 on camera,
2. Turn on inputs to AO cells (with attenuation) so that correlation is present on detector array,
3. Increase either RF power or increase integration time (the latter is preferred) until correlation peak almost saturates the detector array. This will utilize more of the available well potential prior to saturation of the CCPD array,
4. Perform bias addition (128),
5. Perform background subtraction, and
6. Collect/save data for further analysis.

**Figure 3-6** shows the electronic signal generation layout for dynamic range testing. During the test,  $s(t + 0.5 \mu s)$  was attenuated with respect to  $s(t - 0.5 \mu s)$ . **Figure 3-7** shows the results for 0-dB, 20-dB, and 27-dB differential attenuation. From **Figure 3-7**, dynamic range appears to be 27 dB, but pixel-to-pixel non-uniformities and gain imbalances between odd and even pixels are preventing an accurate measurement of the dynamic range.

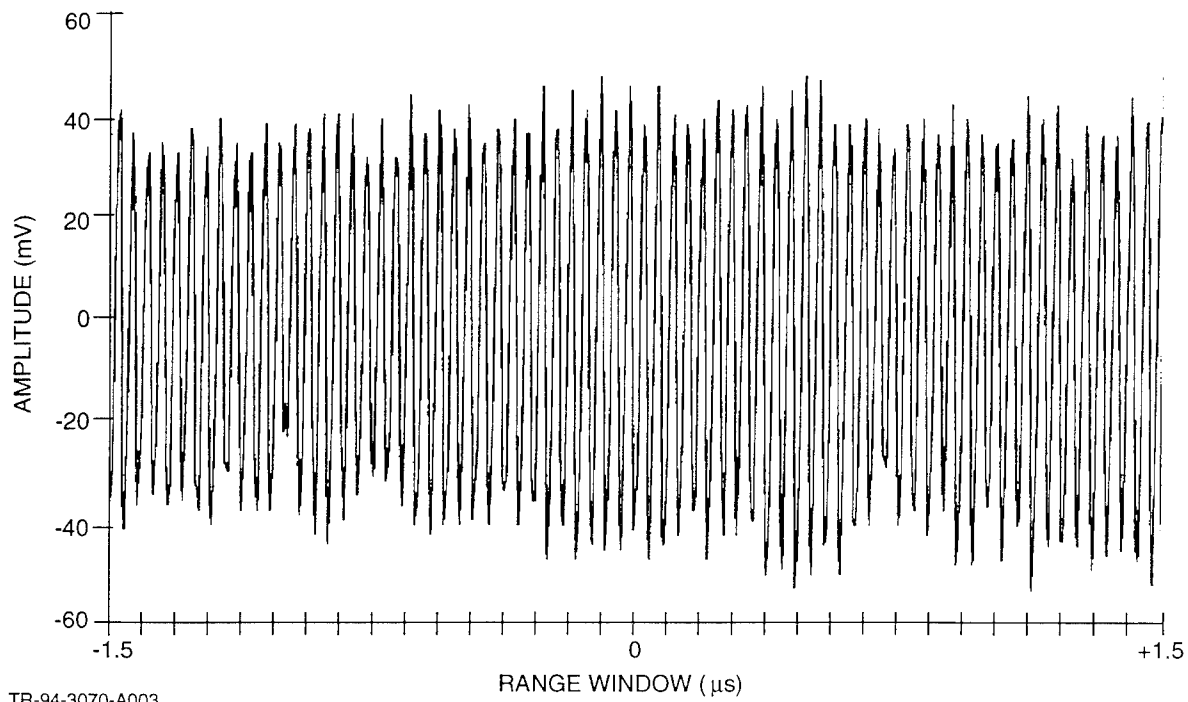
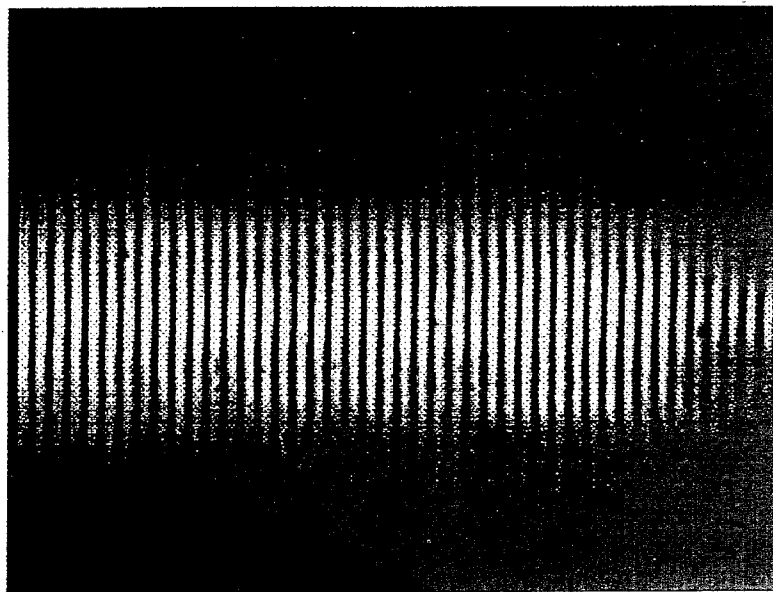
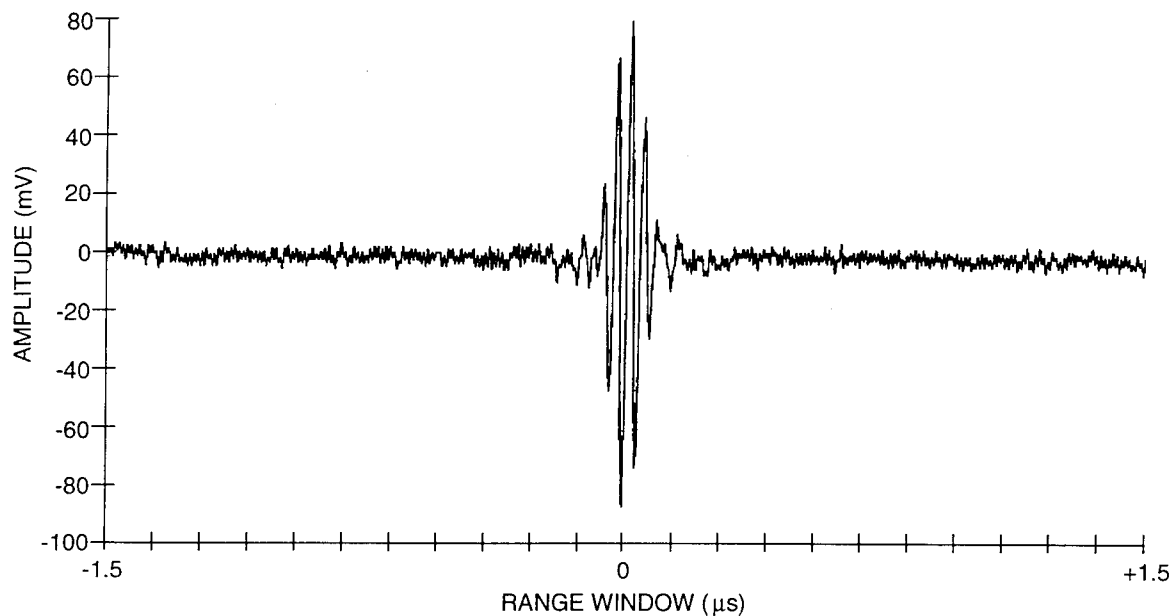


***Figure 3-3. Window Uniformity: Linear Array Output***



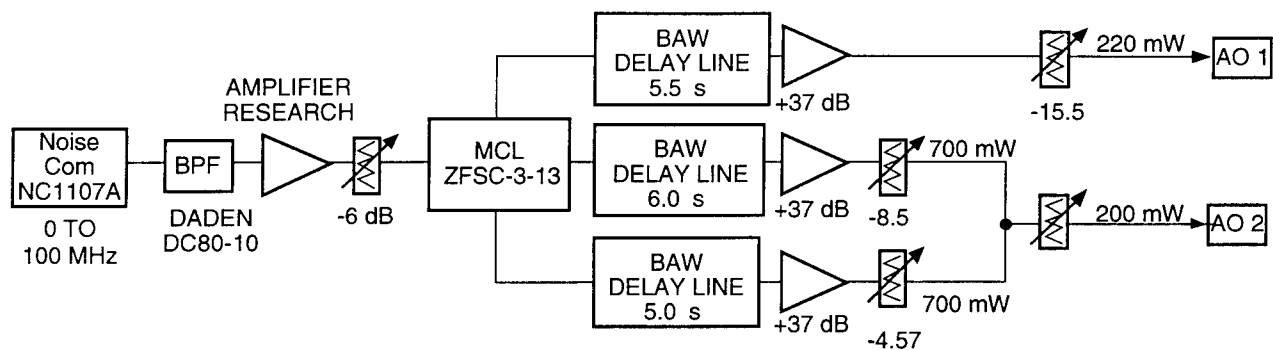
RANGE WINDOW

***Figure 3-4. Window Uniformity: 2-D Camera Output***



TR-94-3072-A003

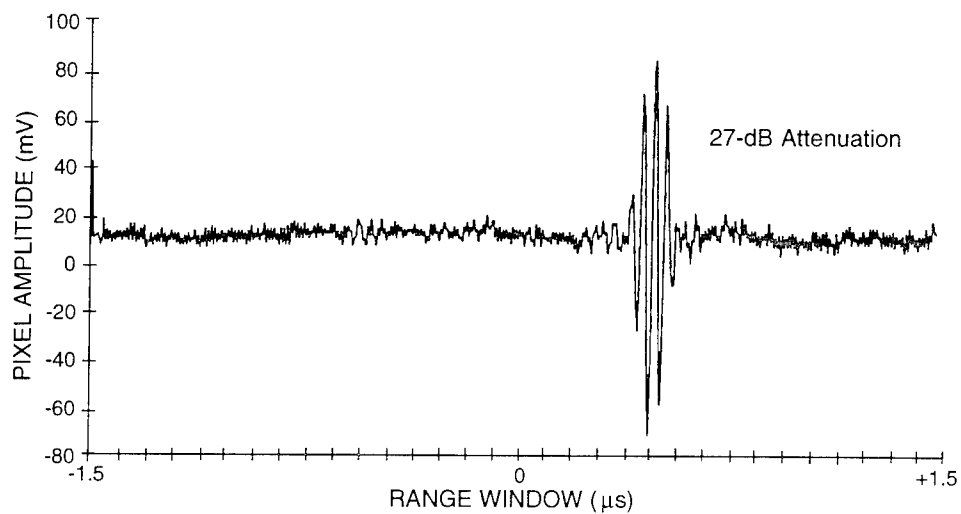
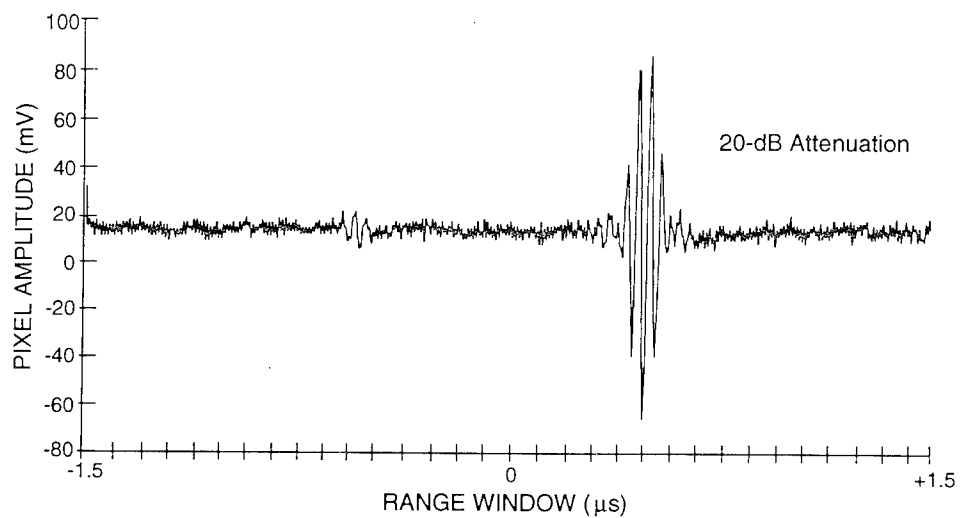
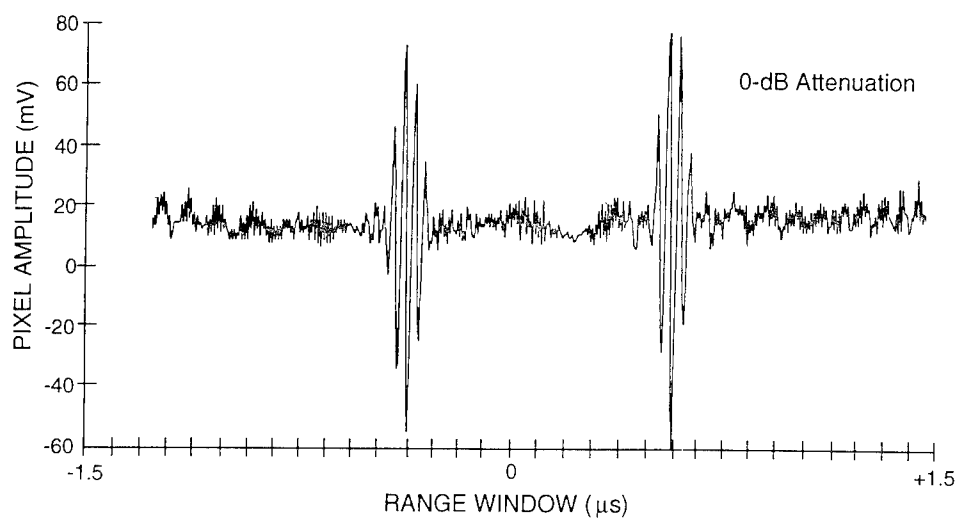
**Figure 3-5. Range Window Centering Using 10-MHz Noise Inputs**



NOTE: ALL VALUES SHOWN ARE FOR INITIAL SETUP

TR-94-3073-A003

**Figure 3-6. Dynamic Range Test Signal Generation Layout**



TR-94-3074-A003

**Figure 3-7. Dynamic Range Tests**

To better understand "true" dynamic range, the CCPD data was saved, converted to an "XL" file, and then analyzed using MATLAB. A MATLAB simulation, DATAPLOT, was written to analyze the detector output. The listing of DATAPLOT is contained in Appendix A. The expected data format is a 512-element column of data corresponding to the voltage levels from the 512 pixels on the linear array. Also read into the program are the background levels due to A01 and A02. Background subtraction is performed in the program.

An FFT of the detector output is performed and plotted as output. *Figure 3-8* shows the detector output (after background subtraction), and *Figure 3-9* shows the spectral content of the detector output after performing the FFT. The axis of *Figure 3-9* along the horizontal is spatial frequency. The plot also folds over at the midpoint (at the highest spatial frequency), a feature inherent in the standard MATLAB FFT. As seen in the figure, an appreciable term due to detector odd/even gain mismatch results at highest frequency. Correlation information (10 MHz) location depends on the spatial carrier frequency. It is desired to have the spatial carrier high enough to allow for needed sampling yet low enough to keep spectrum terms separated.

Separation of the desired and undesired terms in the frequency domain allows spectral filtering to be performed. DATAPLOT also allows for the option of a bandpass filter to be centered around the desired information while blocking out the unwanted information (as shown in *Figure 3-10*). Once frequency domain filtering has been accomplished, DATAPLOT takes an inverse FFT (IFFT) of the spectral data and converts the data to a time domain plot (original format). *Figure 3-11* shows the correlation data after filtering has been performed in the frequency domain. Comparing the unfiltered correlation (*Figure 3-8*) and the filtered correlation (*Figure 3-11*) outputs, a reduction in the spatial nonuniformity can be seen.

DATAPLOT also was used to calculate the signal-to-noise ratio (SNR) of the correlator. SNR values are calculated in MATLAB by taking the ratio of the maximum signal value (S) and the root mean square (rms) noise floor (N).  $SNR = 20 \log_{10} (S/N)$ . Different data sets were used and different functions were performed (i.e., filtering versus no filtering) to compare expected performance from the correlator under given conditions. *Table 3-1* lists the test conditions and resulting SNR values obtained from DATAPLOT. As seen in the table, background subtraction added >3 dB of SNR. The benefits of implementing a frequency filter can be seen to be >8 dB improvement in SNR. Also, the effects of proper data collection methods can also be noted. Optimizing power levels onto the detector can result in ~5 dB of improvement in SNR (based on the data sets available).

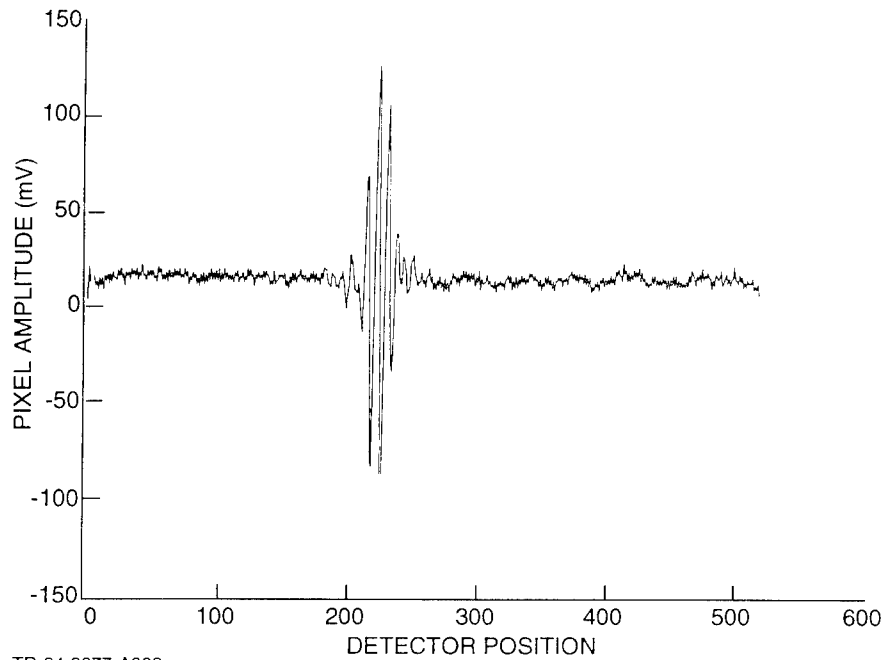


**Figure 3-8. Representative Detector Output**

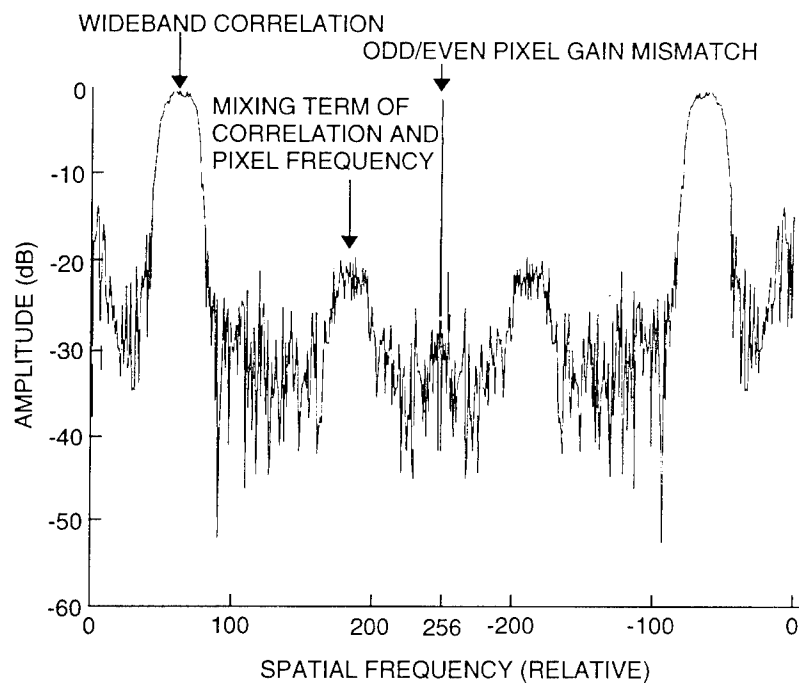
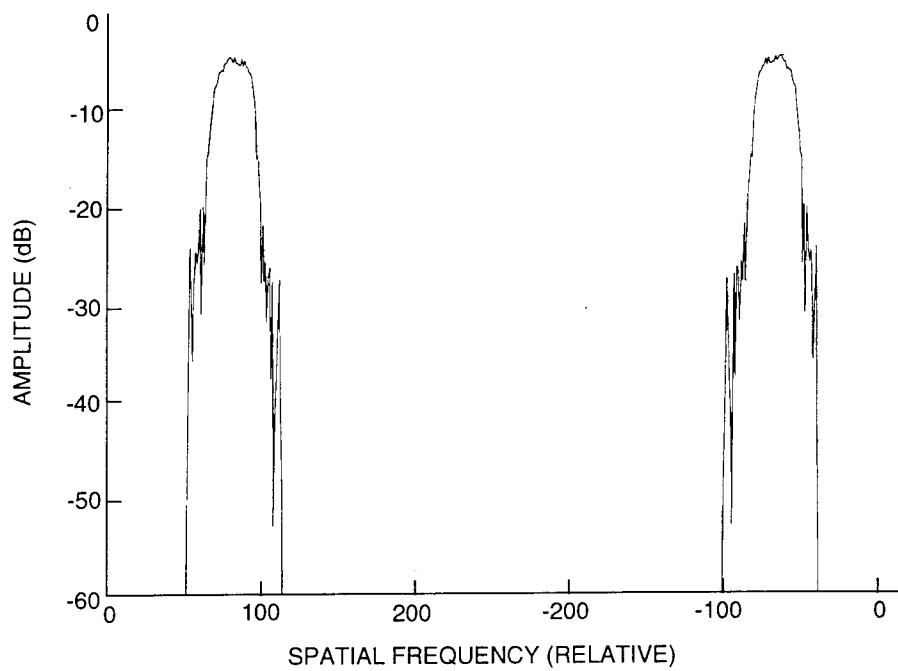
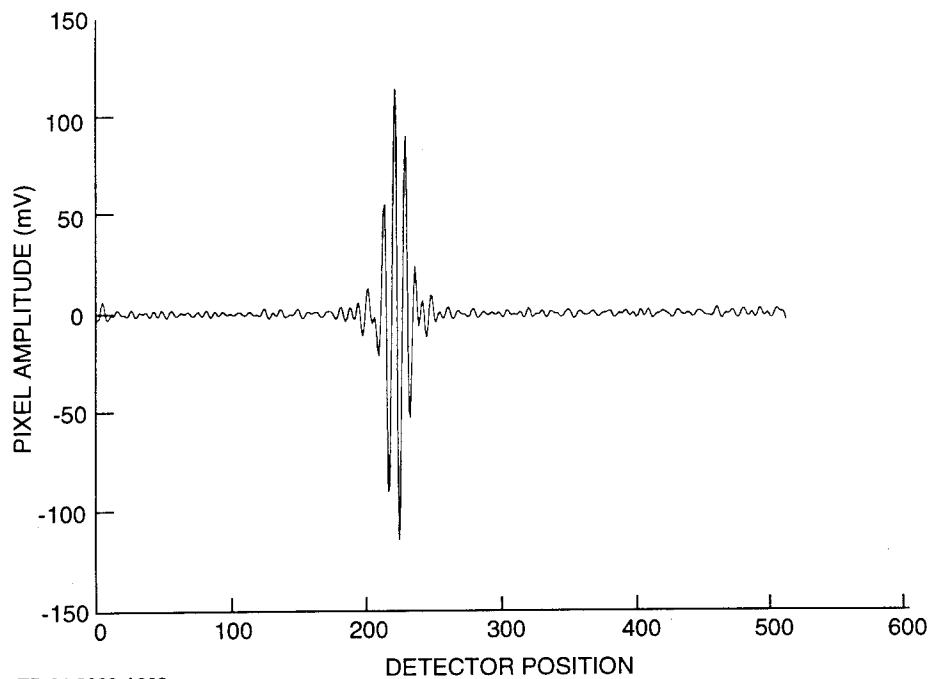


**Figure 3-9. Spectral Content of Detector Output**



TR-94-3079-A003

**Figure 3-10. Bandpass Filter Placed Around Wideband (Desired) Information**



TR-94-3080-A003

**Figure 3-11. Correlation Output After Filtering**

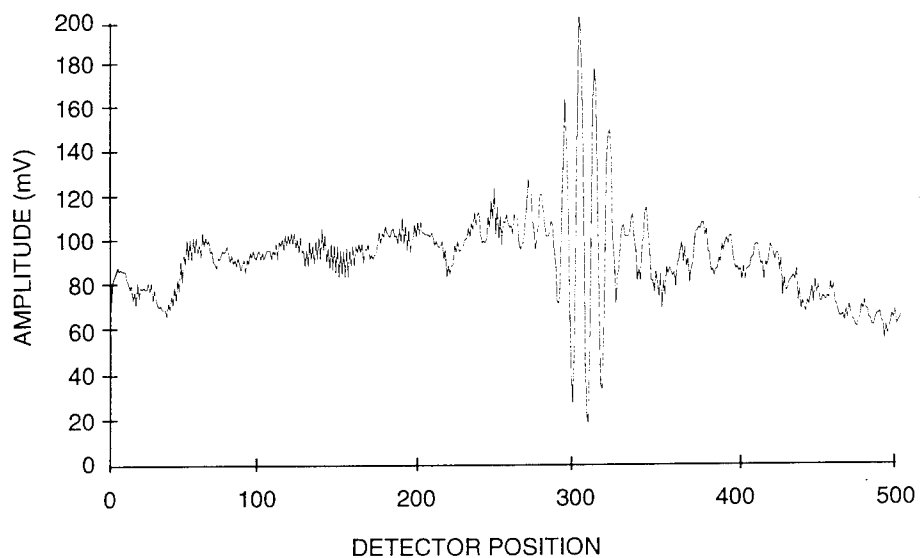
**Table 3-1. SNR Calculations as Function of Data File, Feature Implementation, and Data Collection Optimization**

Background Subtraction	Power Optimization Prior to Bias Addition	Frequency Bandpass Filtering	Calculated SNR
No	No	No	24.01 dB
No	Yes	No	29.27 dB
Yes	Yes	No	32.47 dB
Yes	Yes	Yes	40.52 dB

The in-line correlator architecture was reinvestigated due to spatial carrier fluctuations inherent in the two-path correlator architecture. This portion of the effort focused on achieving correlation through direct modulation of a Toshiba 10-mW, 670-nm laser diode. Hardware implementation was performed using some Dynetics hardware (laser diode circuit board, Picosecond Labs bias-T). Signal generation was implemented (including reference tones) for correlating a pulse (0.1  $\mu$ s) on an 80-MHz carrier. Correlation was achieved, but due to limited time, no data collection or characterization was performed. Based on the stability gained with the in-line architecture, implementation of an in-line correlator is recommended as a future MADOP activity. Implementation of the in-line correlator in the MADOP is expected to increase performance in closed-loop testing.

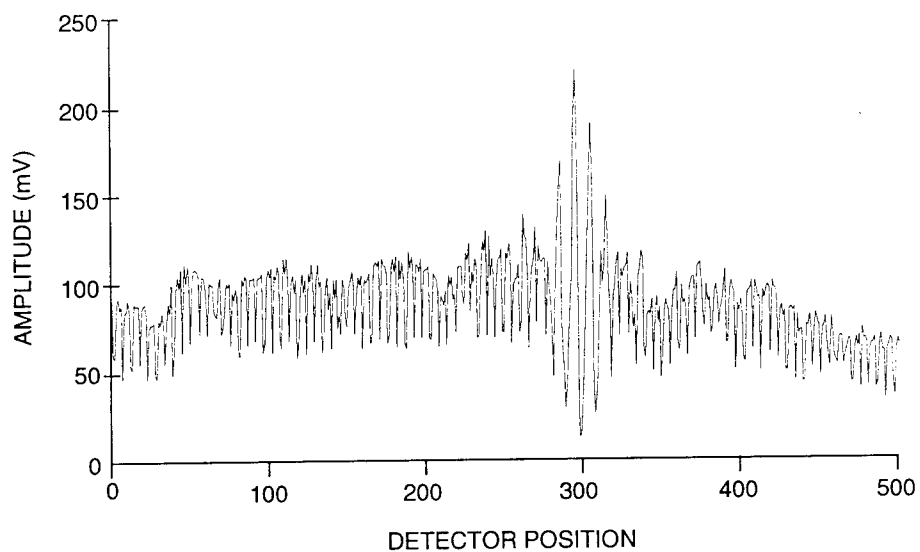
The correlator breadboard table was transported to the radar facility for integration and initial testing of the MADOP system. After transport, the correlator was tested again to verify performance. During verification testing, it was discovered that the laser had been moved during transport. Minor realignment and performance verification testing was performed on the correlator. Performance of the correlator after realignment was equal to that measured prior to breadboard transportation.

The C-band radar testbed used for the testing has the option to operate in a receive-only mode, or in a switched transmit/receive (T/R) mode. **Figure 3-12** is the output from the CCPD array and shows correlation from an 8-MHz jammer source while the radar is in the receive-only mode. However, **Figure 3-13** shows the output from the CCD array for the same signal while the radar is in the T/R mode. Note that there is additional noise due to the T/R switching. This noise autocorrelates across the time window. Note that in an application where the auxiliary channel is passive, there will be T/R noise present in the main channel, but the noise will not be correlated due to its absence in the auxiliary channel.



TR-94-3081-A003

**Figure 3-12. 8-MHz Jammer Correlation (Receive Mode Only)**



TR-94-3082-A003

**Figure 3-13. 8-MHz Jammer Correlation (T/R Switching Mode)**

DATAPLOT was used to further analyze and characterize the T/R noise and its effect on the correlation. **Figure 3-14** shows the correlation of an 8-MHz jammer with T/R noise present and **Figure 3-15** shows its spectrum. As mentioned earlier, the horizontal axis of **Figure 3-15** is spatial frequency. The spectrum plots presented in this section also fold over at the midpoint (at the highest spatial frequency), a feature inherent in the standard MATLAB FFT. Noted in the figure are the location of the wideband correlation on its spatial carrier (set by the beam combiner in the two-path architecture), and the odd/even pixel mismatch. To analyze contributions due to the T/R switching, one of the AO cells was blocked and the other was imaged onto the CCD array. **Figure 3-16** shows the resulting image. The signal into the AO cell was not changed (i.e., 8-MHz jammer and T/R noise). Note that the gradual amplitude falloff along the detector position axis is due to illumination and AO cell aperture effects. **Figure 3-17** shows the detector spectrum. Noted in the figure are the main spatial frequency contributions due to the T/R noise and also the product of the main term with the pixel gain mismatch term. A bandpass filter was positioned about the correlation spatial frequency (**Figure 3-18**), and an FFT was performed on the information to obtain the contributions of the T/R noise within the correlation spatial frequency window (**Figure 3-19**). Note the amplitude scale in the plot of the filtered T/R contributions as compared to that of **Figure 3-16**.

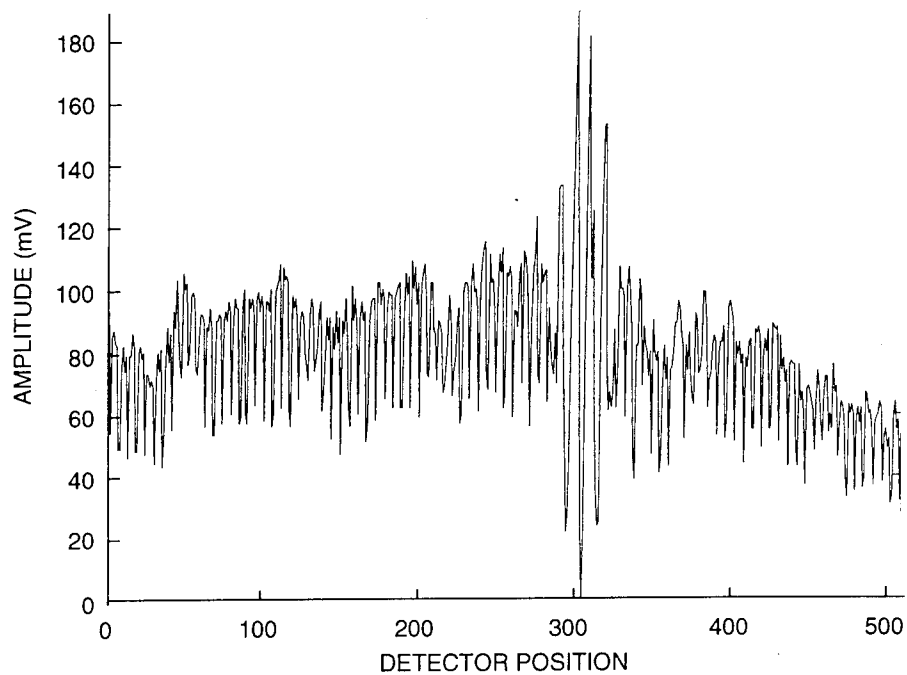
Finally, the AO cell beam block was removed and correlation information was collected and processed using MATLAB. **Figures 3-20 and 3-21** show the filtered correlation spectrum and the filtered correlation, respectively, for the 8-MHz jammer with T/R switching noise. As seen in **Figure 3-21**, the contribution of the T/R noise within the correlation bandpass degrades the dynamic range of the correlation. Investigations into the reduction of the T/R noise, possibly through appropriate selection of correlation spatial carrier frequency, need to be addressed in the follow-on effort. Implementation of spatial carrier setting for the two-path architecture is performed through mechanical rotation of optical components. In the in-line architecture, it is accomplished through electronic control/setting of the reference tone.

### 3.3 AOTDL FILTER

The AOTDL filter was successfully improved in each of the three periods of onsite support at the RL Photonics Center. The enhancements to the AOTDL filter are described in this section.

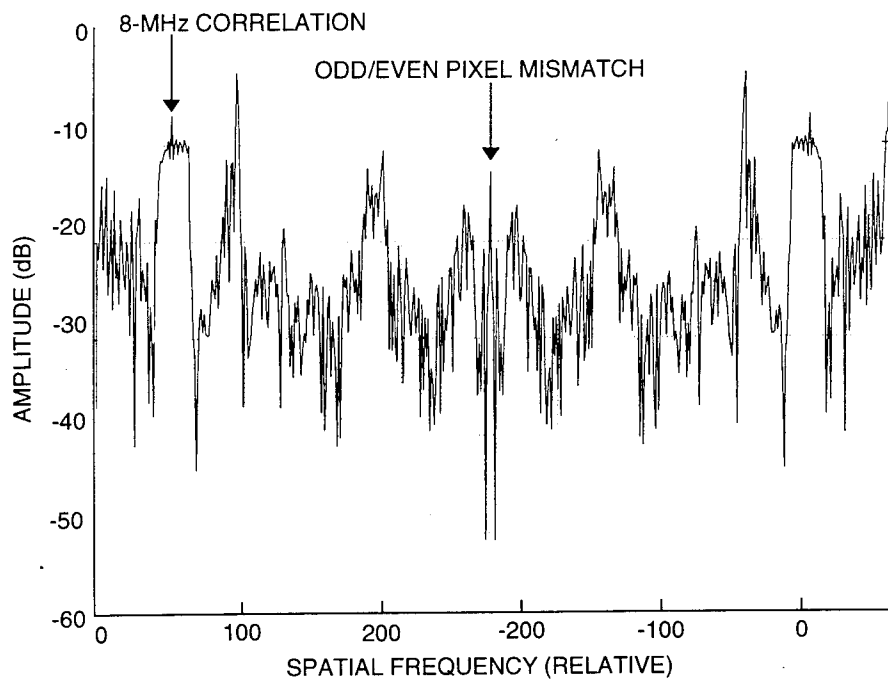
#### 3.3.1 Onsite Support Period One

During the first period of onsite support, the system was enhanced through the accomplishment of the following activities:



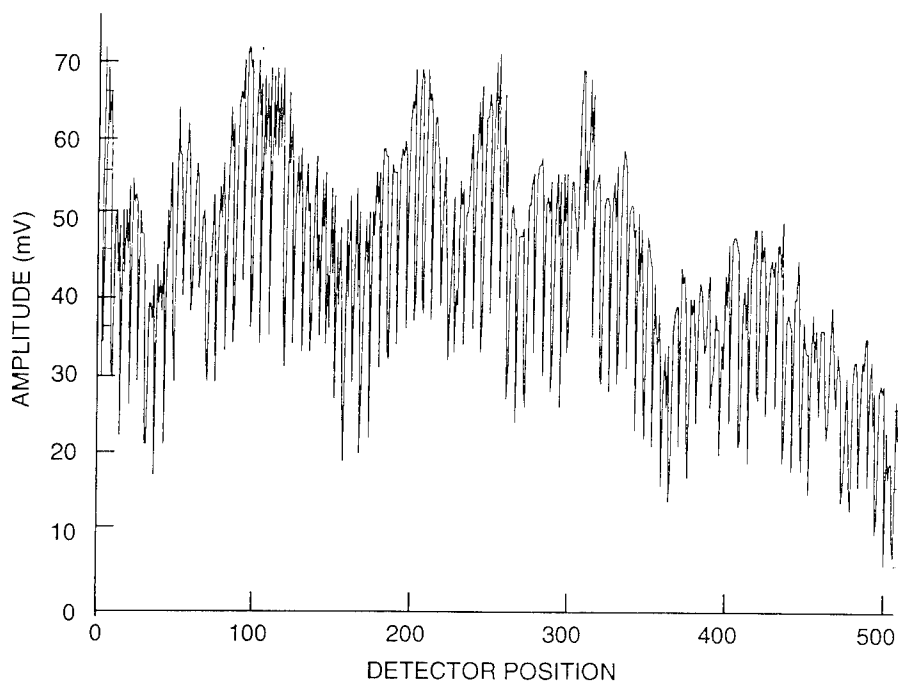
TR-94-3083-A003

**Figure 3-14. 8-MHz Correlation With T/R Noise**



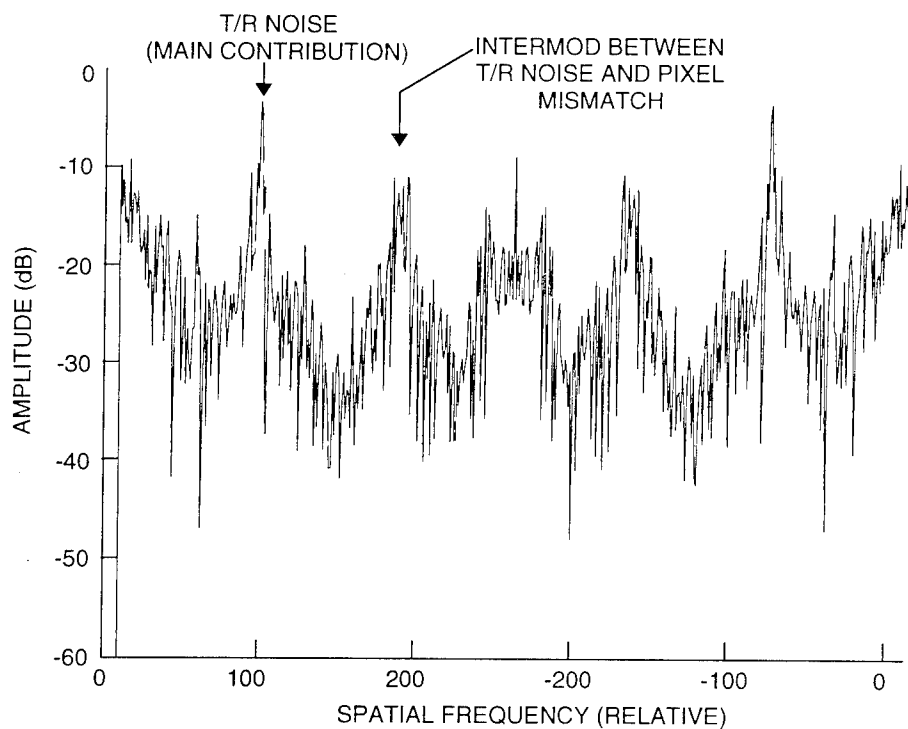
TR-94-3084-A003

**Figure 3-15. Spectrum of CCPD Output**



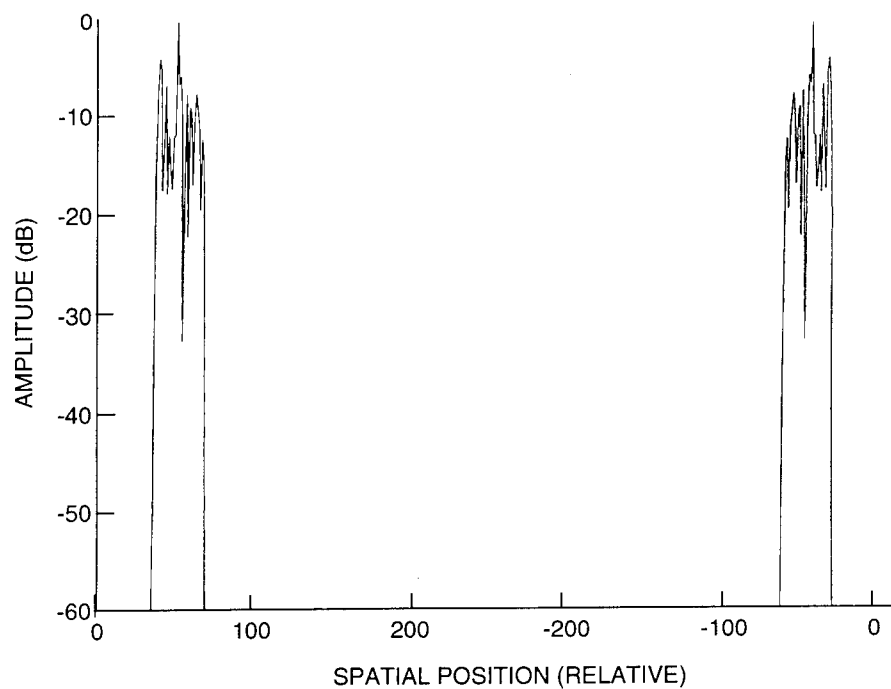
TR-94-3085-A003

**Figure 3-16. Single AO Cell T/R Noise**



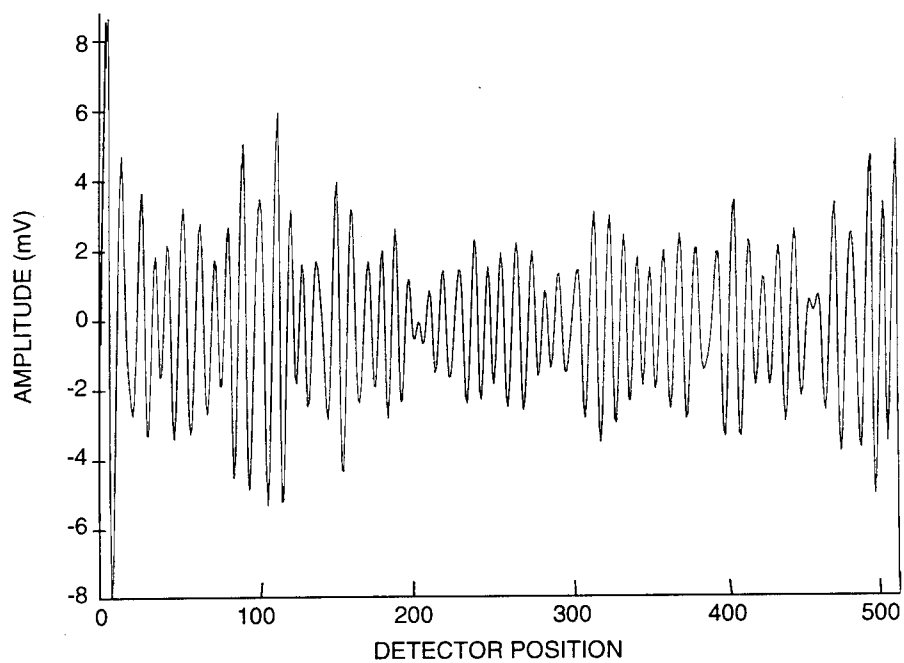
TR-94-3086-A003

**Figure 3-17. Single AO Cell T/R Noise Spectrum**



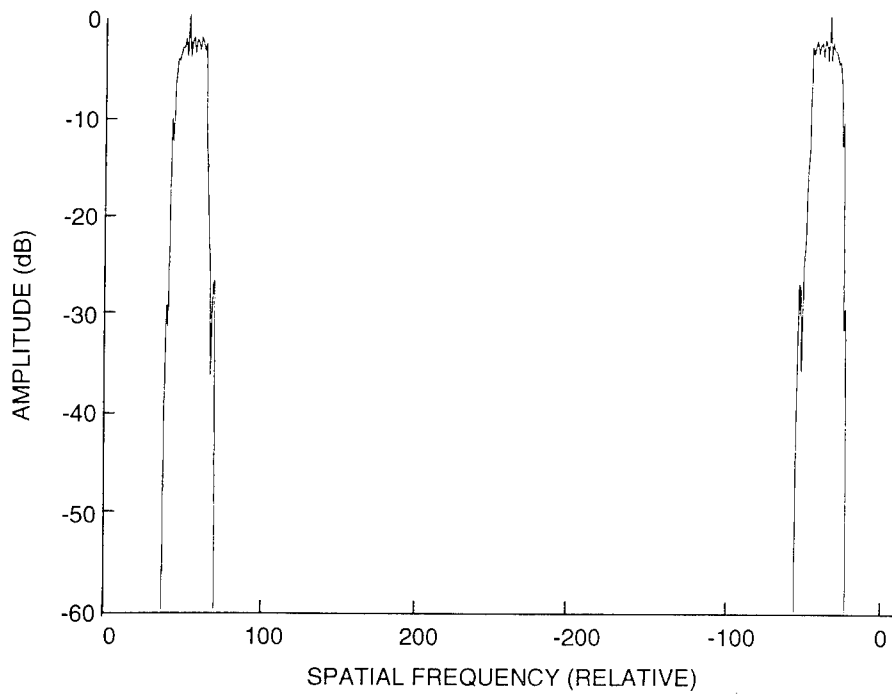
TR-94-3087-A003

**Figure 3-18. Filtered T/R Noise**



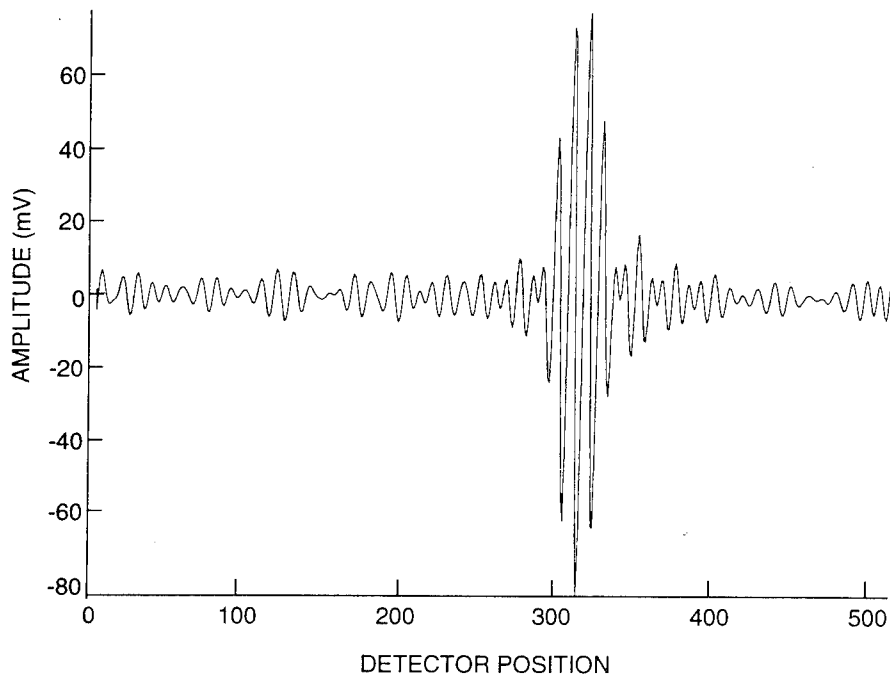
TR-94-3088-A003

**Figure 3-19. T/R Noise After Filtering**



TR-94-3089-A003

**Figure 3-20. Filtered Correlation Spectrum (With T/R Contributions)**



TR-94-3090-A003

**Figure 3-21. Filtered Correlation (With T/R Contributions)**

1. Realigned subsystem with new frequency-doubled Nd:YAG laser.
2. Designed new cylindrical/spherical lens system for insertion between the AOSLM and AOTDL and implemented this with two 300-mm cylinders and the 750-mm spherical lens. The cylindrical lens design optimization MATLAB routine and resulting design are shown in *Figure 3-22*.
3. Implemented a spatial block of the -1 order out of the AOTDL in order to decrease insertion loss and improve system stability. A 38-mm spherical lens was added before the 16.5-mm lens after the AOTDL to achieve this block through a frequency plane mask. With this enhancement, the AOTDL bandwidth was increased to 25 MHz.
4. Developed and documented alignment procedures from laser to detector for the AOTDL subsystem, including alignment without any mirror adjustments or AO cell Bragg angle adjustments.
5. Characterized the optical crosstalk from the AOSLM. This is now dominant since electronic crosstalk has been reduced below the noise floor through the insertion of the new ac-coupled New Focus photodetector/amplifier package.

During this first onsite support period, alignment procedures for the AOTDL subsystem were developed. This activity included a complete realignment including the use of a new laser. Key changes included: 1) the AOSLM was placed on a fixed mount so it does not have Bragg alignment adjustment (however, using slotted screw holes provides the necessary flexibility to rapidly align the device); 2) mirrors were taken off of their adjustable mounts to reduce this major source of instability; and 3) a new pair of cylindrical lenses was provided to perform the acoustic column imaging function (orthogonal to the acoustic propagation direction).

During setup of the AOTDL, the height should be set so that the maximum frequency (which corresponds to the minimum time delay) is within the acoustic aperture. If this is not done, the optical tap may be cut off by the mechanical window.

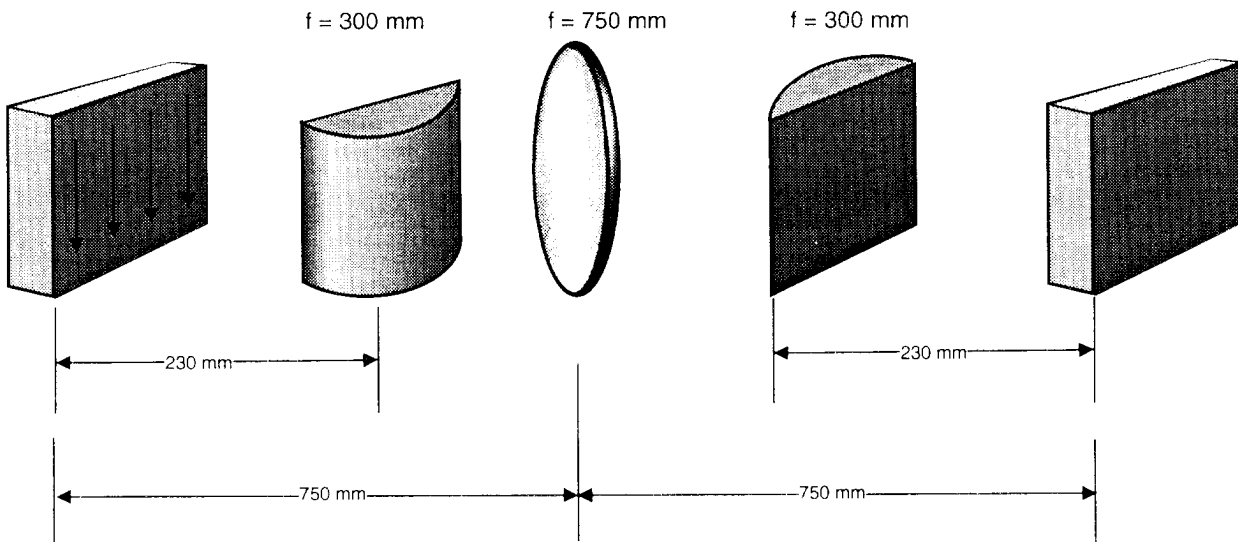
Alignment of the AOTDL for one frequency (80 MHz) is first achieved. The tap is then swept over the 60- to 100-MHz band and it is expected that significant variation in insertion loss will occur. Part of this is due to detector misalignment at this point, but the other part is due to Bragg diffraction loss in the AOSLM. To test the diffraction loss, an optical power meter is placed behind the AOTDL to measure all of the power coming through the tap. Over the 60- to 100-MHz band it was found for this alignment that the optical power varied by 5.5 dB. This means an 11-dB

```

f1=300;
f2=300;
s0=(10:10:750);
s1=750-s0;
I1=s0*f1./(s0-f1);
I2=750*(s1-I1)./(s1-I1-750);
s3plus=-0.5*(I2-750-sqrt((I2-750).^2+4*(I2*f2-750*f2)));
s3minus=-0.5*(I2-750+sqrt((I2-750).^2+4*(I2*f2-750*f2)));
Mplus=(I1./s0).*(I2./(s1-I1)).*(s3plus./(750-s3plus-I2));
Mminus=(I1./s0).*(I2./(s1-I1)).*(s3minus./(750-s3minus-I2));
plot(s3plus)
pause
plot(s3minus)

```

(a) MATLAB Routine



(b) Resulting Design

TR-94-3091-A003

**Figure 3-22. Anamorphic Lens Arrangement**

insertion loss difference due only to optical power considerations. By changing the frequency range it was found that the optimum performance was in the 56- to 96-MHz frequency band. Over this range, 3-dB optical variation was achieved, corresponding to 6-dB insertion loss change due to optical tap power only. For this reason, this band was selected for the operating tap frequencies. Note, however, that the Bragg angle on the AOSLM was not adjusted; therefore, it might be possible to re-optimize. It is recommended when coming back to the system after a period of low usage that the optical tap power, as a function of frequency, be measured in order to select the optimum frequency range.

The next step in the process is to insert the detector and make the system operate over the full range of tap positions. The 16.5-mm lens that was originally in the system was utilized, but a longer focal length arrangement was also attempted. A 38-mm focal length lens was inserted after the AOTDL, and the Fourier plane was located by sweeping the frequency into the AOSLM and then finding the plane at which the spot did not move (by much). The detector was then placed in that position. At most frequencies, the system performed well and the insertion loss varied by approximately 15 dB. At a couple of frequencies, however, the insertion loss increased and the frequency response was very unstable. A card was inserted to remove the +1 or -1 order from the detected signal, and insertion loss performance improved. Additionally, the instability went away. The card was inserted in front of the detector; but as tap positions were changed, the spot moved on the card and performance was not good. Because of this, the card should be in an intermediate Fourier plane, and this Fourier plane should then be reimaged onto the detector with a second lens.

A razor blade was placed in the Fourier plane (replacing the card described above) and then imaged onto the detector. The razor blade was placed on a y-z (height-optical axis) adjustment so that the height and focus position could be accurately positioned. Alignment of both the detector and razor blade was tricky and required a well planned procedure. The following steps were used to achieve alignment:

1. Coarse Setting of Detector Position - The detector face must be precisely in the imaged Fourier plane of the AOTDL. If not, the spot will move as a function of tap position. To set the detector, the razor blade is lowered so that it does not block any of the light. Set the tap generator to sweep over the tap driver bandwidth of 40 MHz. Set the sweep time to 500 ms. On the detector, the spot will move. Adjust the z position of the detector until the movement appears to be minimized.

2. Fine Setting of Detector Position - Set the AOSLM frequency generator to the lower portion of the band, and adjust the detector until a good output is obtained. Do not worry about fluctuations in the frequency that are caused by plus and minus order interactions since these will be removed later. Now adjust the frequency generator to produce the maximum tap frequency. This will likely cause the spot to be off the detector, resulting in poor response. Now adjust the height of the detector until good performance is again achieved. Take note of the direction of change for the detector (i.e., higher or lower). Now set the frequency generator back to the lower frequency. Move the detector z position in one direction or the other, but take note of the direction. Again go to maximum frequency and note the direction that the detector must be moved. Was it more or less than the last time? If less, keep going in the same z direction and repeat. If more, go the opposite way. Repeat this procedure until good uniformity is achieved over the entire tap bandwidth. Note that if the detector is adjusted too far, the direction of vertical adjustment will change.
3. Coarse Setting of Razor Blade - The frequency generator should then be set in the swept mode and the z position of the razor blade adjusted until the movement of the spot is minimized.
4. Fine Setting of Razor Blade - With the frequency generator set in the continuous wave (CW) mode at the lowest frequency, the blade height should be adjusted until the blade blocks the entire beam. The blade is then lowered until the insertion loss was minimized. Usually this will occur at the right blade position. By continuing to lower the blade, the frequency response will be reduced and become more unstable as more of the  $\pm 1$  diffraction orders begin to mix. The frequency generator is then set to the maximum frequency and the blade height is adjusted until the best performance is achieved. Notice the direction of height change needed. Using the z position adjustment of the blade, this procedure is iterated similarly to the detector procedure. Once this adjustment is completed, good performance should be attained over all tap positions.
5. Fine Tuning - At this point, it might be useful to fine tune the x and y adjustments of the detector to try and reoptimize. It might help to repeat the steps above and see if anything improves. Repeat until no better performance is obtained.

The performance achieved after this alignment procedure is shown in **Table 3-2**. **Figure 3-23** shows network analyzer traces of the magnitude response for the AOTDL. As noted, the span is 10 MHz (the design bandwidth) and the center frequency is 80 MHz. The magnitude scale is 3 dB/div. The five different plots are for different frequency inputs into the AOSLM. For example, the first figure corresponds to an input frequency of 56 MHz into the AOSLM. The remaining plots are incremented by 10 MHz in AOSLM input frequency. Notice that the bandwidth is very flat and that there is not a large insertion loss variation as we change tap frequencies (< 9 dB variation). **Figure 3-24** shows one magnitude response over a wider bandwidth of 25 MHz. As seen in this figure, the AOTDL has a rather large bandwidth.

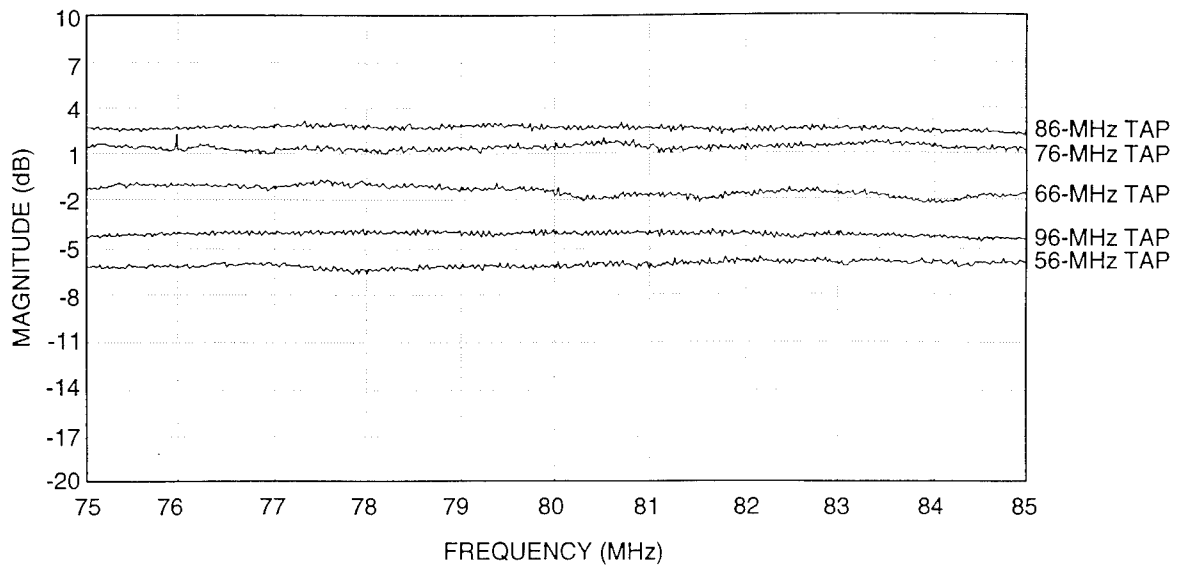
**Table 3-2. AOTDL Filter Performance Measurements: Onsite Support Period One**

Parameter	Measured Performance
Input Tap Power	50 mW
Input Tap Frequency Range	56 to 96 MHz
Insertion Loss (minimum)	-2 dB
Insertion Loss (maximum)	-13 dB
Output Noise Floor	-112 dBm/Hz
Output Noise Over 10 MHz Band	-42 dBm
Tap Frequency Coupling into the Output	-42 dB (relative to input tap drive power)
Max Spurious*	-25 dB at maximum drive power (due to intermod between tap leakage and signal)
Dynamic Range** (noise Limited at 12 dBm Drive)	Maximum 52 dB, minimum 41 dB

\*Intermods appear to be caused by detector non-linearities. Probably could reduce different detector/amplifier combination.

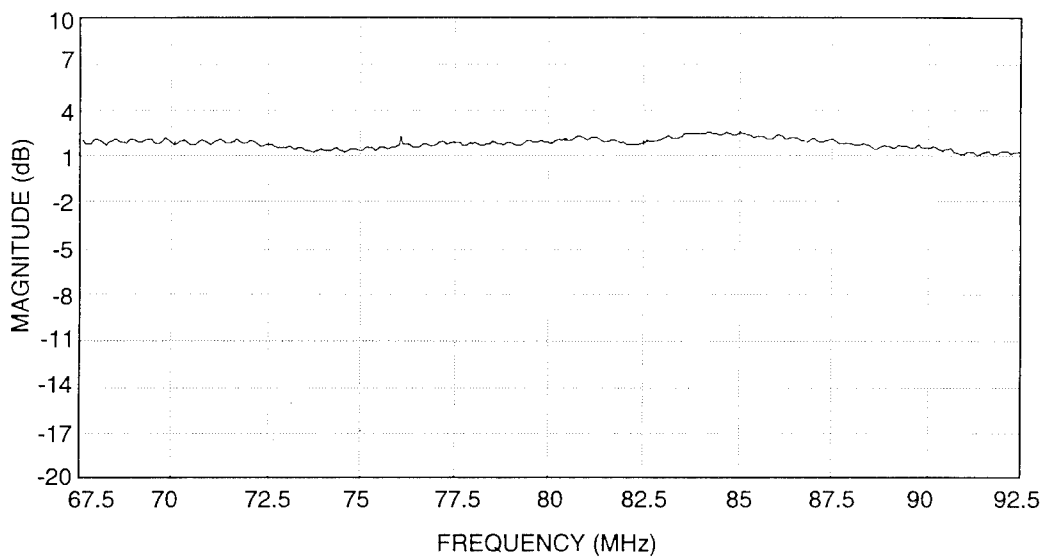
\*\*This dynamic range is misleading because of spurious signals.

**Figures 3-25 and 3-26** show the output spectrum for a CW input. The largest peak in the output is the actual delayed signal, at the input frequency; but note that there are other terms associated with both leakage of the AOSLM drive frequency and intermodulation products between this leakage signal and the desired signal. It was verified that this AOSLM drive frequency leakage was a purely optical phenomenon and not due to RF crosstalk. The only difference between these figures is that the AOSLM drive frequency was changed. It is believed that the intermodulation product terms could be reduced with a detector/amplifier combination that does not have as much nonlinearity. The leakage term is still difficult to deal with at this time.



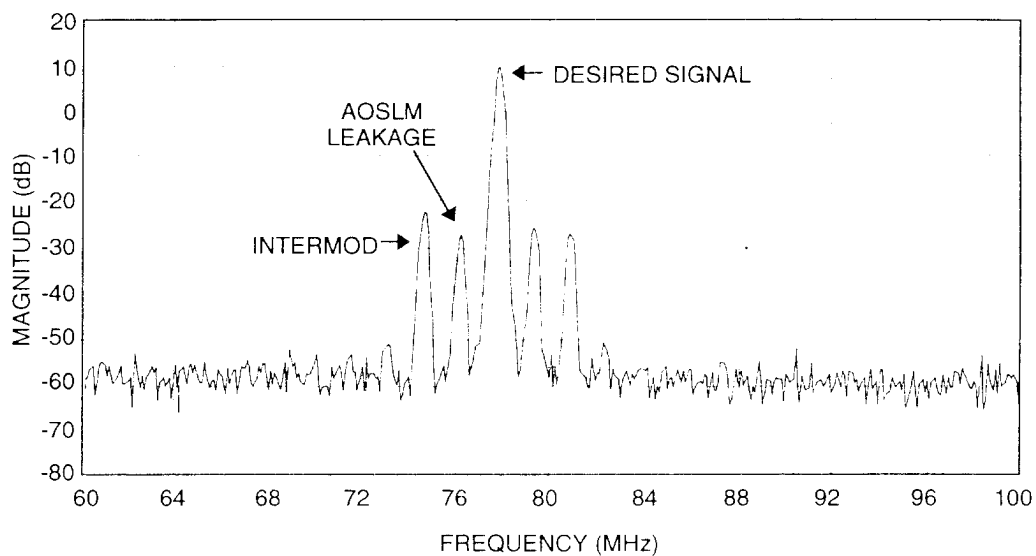
TR-94-3092-A003

**Figure 3-23. AOTDL Frequency Response: Onsite Support Period 1**



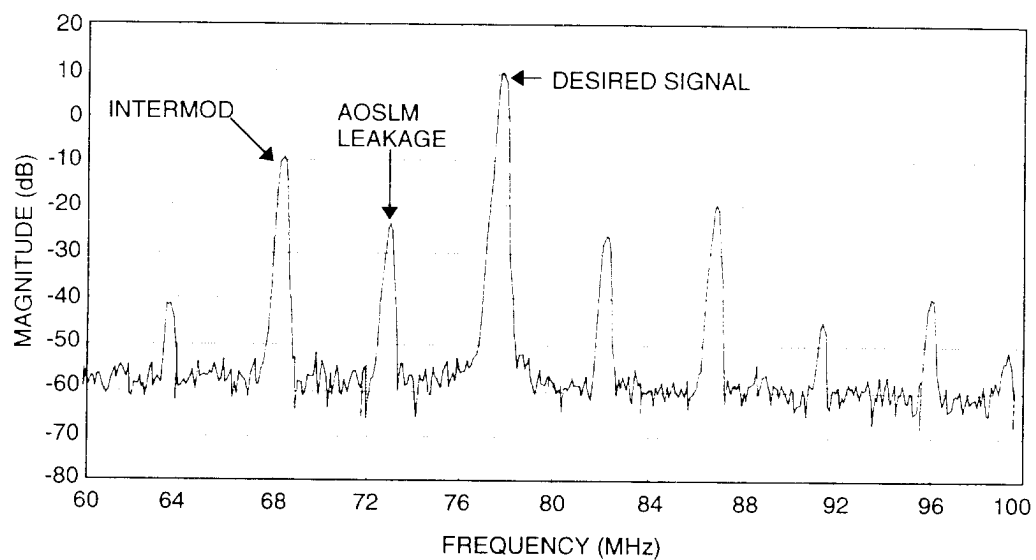
TR-94-3097-A003

**Figure 3-24. AOTDL Frequency Response for 25-MHz Span**



TR-94-3098-A003

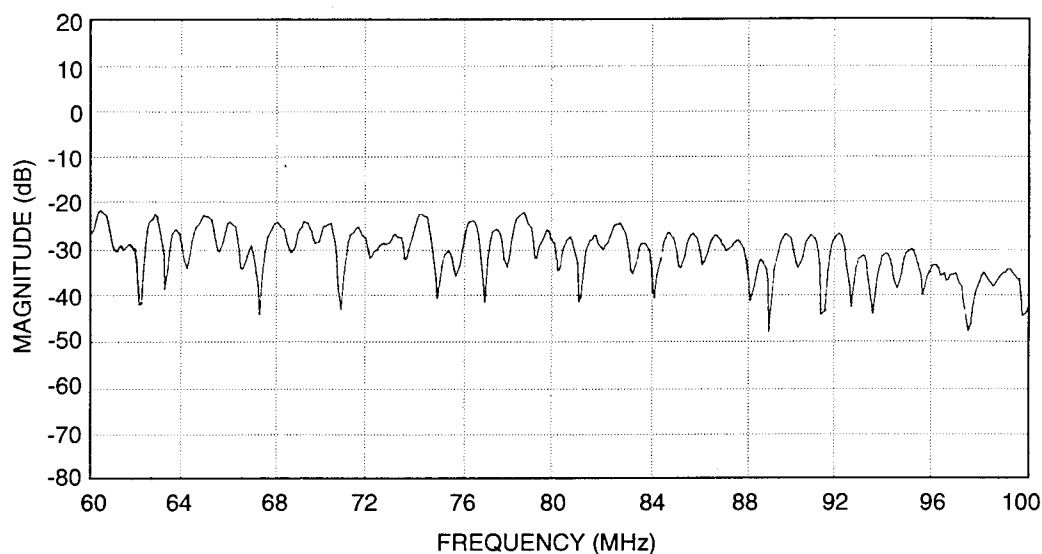
**Figure 3-25. AOTDL Output for Single Tone Input: AOSLM Frequency 1**



TR-94-3099-A003

**Figure 3-26. AOTDL Output for Single Tone Input: AOSLM Frequency 2**

To determine the severity of the AOSLM tap frequency leakage, the AOSLM was driven with the network analyzer over the 60- to 100-MHz band. The output of the AOTDL detector was then fed back into the network analyzer, but no signal was put into the AOTDL. The resulting plot (*Figure 3-27*) shows that there is considerable leakage across the AOSLM drive band. As shown in *Figures 3-25 and 3-26*, relative to the AOTDL input power, the leakage power output from the system is only down approximately -34 dB. A solution to this problem will eventually need to be found.



TR-94-3100-A003

**Figure 3-27. AOSLM Optical Interference Frequency Response**

### 3.3.2 Onsite Support Period Two

During the second onsite support period, only minor readjustments were made to the AOTDL filter architecture. The AOTDL frequency response was measured as a function of tap frequency, using a network analyzer that provides the input to the AOTDL, with output from the photodetector. The AOTDL filter frequency response during this testing activity is shown in *Figure 3-28*, where we see 3-dB flatness for each tap frequency from 50 MHz to 105 MHz, with a 16-dB insertion loss variation across this extended band of tap frequencies. Note that this is shown for a 25-MHz band, with only the central 10 MHz representing the system operating band. Across the nominal 60-MHz to 100-MHz tap frequency band, the variation of the insertion loss is approximately 7 dB. The spikes appearing in the frequency response plots are due to the feedthrough of the AOSLM tap frequency.

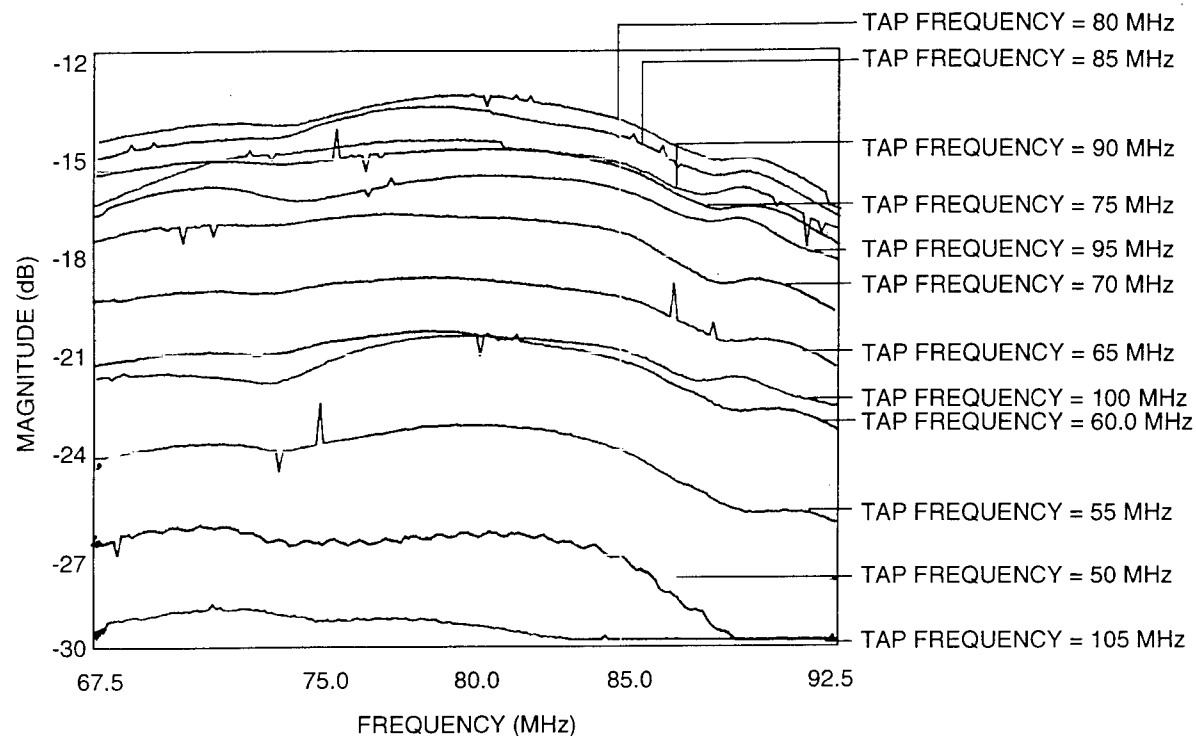


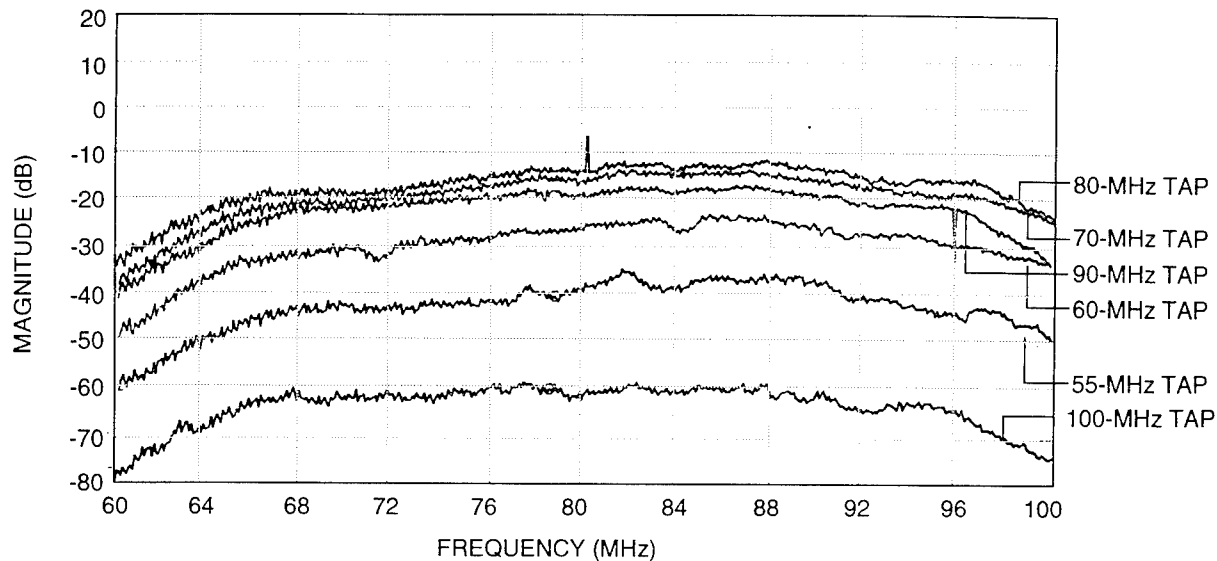
**Figure 3-28. AOTDL Frequency Response: Onsite Support Period 2**

The delay response of the AOTDL filter was also measured. The delay was measured to vary linearly from 1720 ns at a 60-MHz tap frequency to 820 ns at a 100-MHz tap frequency. This, therefore, represents a 900-ns delay window for this configuration of the AOTDL.

### 3.3.3 Onsite Support Period Three

During the third onsite support period, the testing of the MADOP took place in the C-band radar testbed facility. At this time, a slow-shear TeO<sub>2</sub> AO cell was inserted in place of the longitudinal mode TeO<sub>2</sub> device as the AOSLM. This was accommodated through the replacement of the imaging system with a simplified, shorter focal length system and the realignment of the optics. The performance of this resulting architecture improved most notably in the reduction of the tap frequency feedthrough, although this phenomenon was still apparent. The resulting frequency response is shown in **Figure 3-29**, as measured through a significant portion of the RF electronics including a 5-μs bulk acoustic wave (BAW) delay line and an amplifier. Although the frequency response for a given tap was flat to within 3 dB across the band, the variation in insertion loss was measured to be approximately 15 dB across the 60- to 100-MHz tap frequency band. This was apparently due to the poorer frequency response of the slow-shear device as compared to the

longitudinal-mode device (although the specifications were similar). This poorer frequency response should be researched in future test activities. The ripple apparent in the frequency response plots is due to the triple-transit phenomenon in the BAW delay line.



TR-94-3113-A003

**Figure 3-29. Frequency Response From ZSC-1-2 Through 5.0- $\mu$ s Delay Through AMP 20502 Through AOTDL**

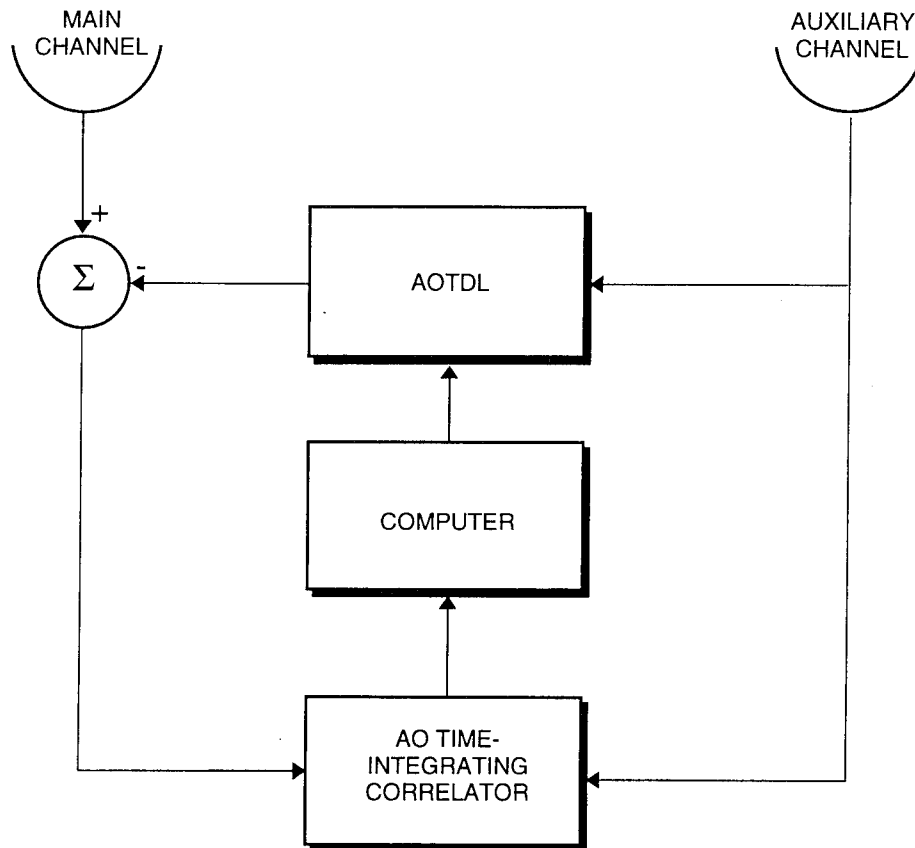
### 3.4 SINGLE-LOOP ELECTRONIC CANCELLER

A block diagram of the original concept of the MADOP is shown in **Figure 3-30**. With the original configuration, the actual cancellation of the jammer signal took place in the summer shown in the upper left portion of **Figure 3-30** and involved the subtraction of two signals on 80-MHz carriers. In order for this subtraction to take place as predicted by theory, it is necessary that the carriers be the same frequency and be phase-locked. In practice this will not occur because of drifts in the optical subsystems supplying the carriers.

To circumvent this problem we developed an electronic circuit, called the electronic canceller, that would phase lock the carrier of the AOTDL signal with the main channel signal. This circuit is configured the same as a sidelobe canceller and is shown in the diagram of **Figure 3-31**. The electronic canceller replaces the summer of **Figure 3-30** as shown in **Figure 3-32**.

The electronic canceller dynamically alters the phase of the AOTDL signal carrier so as to assure that it is properly phase-locked to the carrier of the main channel signal. An error signal,  $e(t)$ , is formed by subtracting the phase-shifted AOTDL signal from the main channel signal. The signal is then mixed with the AOTDL signal to remove the carrier and form a complex, baseband

error signal. The I&Q components of this error signal are then integrated to form new I&Q signals that define the phase, and amplitude, adjustment that must be applied to the AOTDL signal to attempt to drive the error signal to zero.



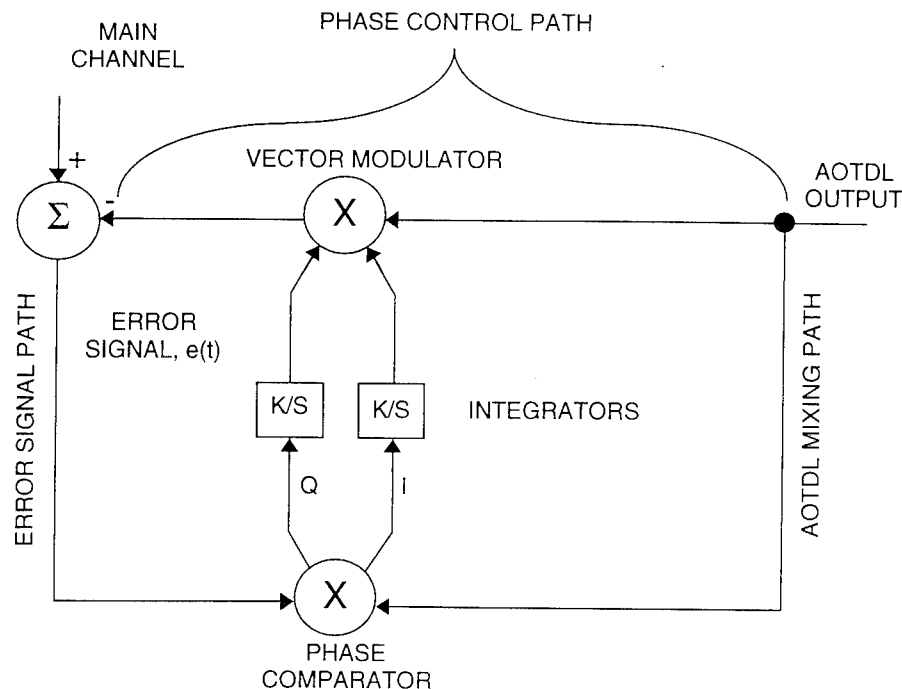
TR-94-3184-A003

**Figure 3-30. Original MADOP Configuration**

If both the main channel and AOTDL signals contained only jammer signals, the error signal would indeed be driven to zero, and the outputs of the phase comparator would also be zero. For the case where the main channel also contains a target signal, the error signal will contain the target signal. Because of this, the outputs of the phase comparator will not be zero. However, for expected signals, they will be rapidly changing signals that will be filtered by the integrators.

In its original implementation, the electronic canceller used splitters and mixers to form the phase comparator and vector modulator. This caused the circuit to have low gain and resulted in unstable operation of the canceller. In order to reduce the number of components in the vector modulator and phase comparator, Capt. Ward and Capt. Keefer of the RL Photonics Center had the

phase comparator and vector modulator specially fabricated between the last and present ESE efforts.

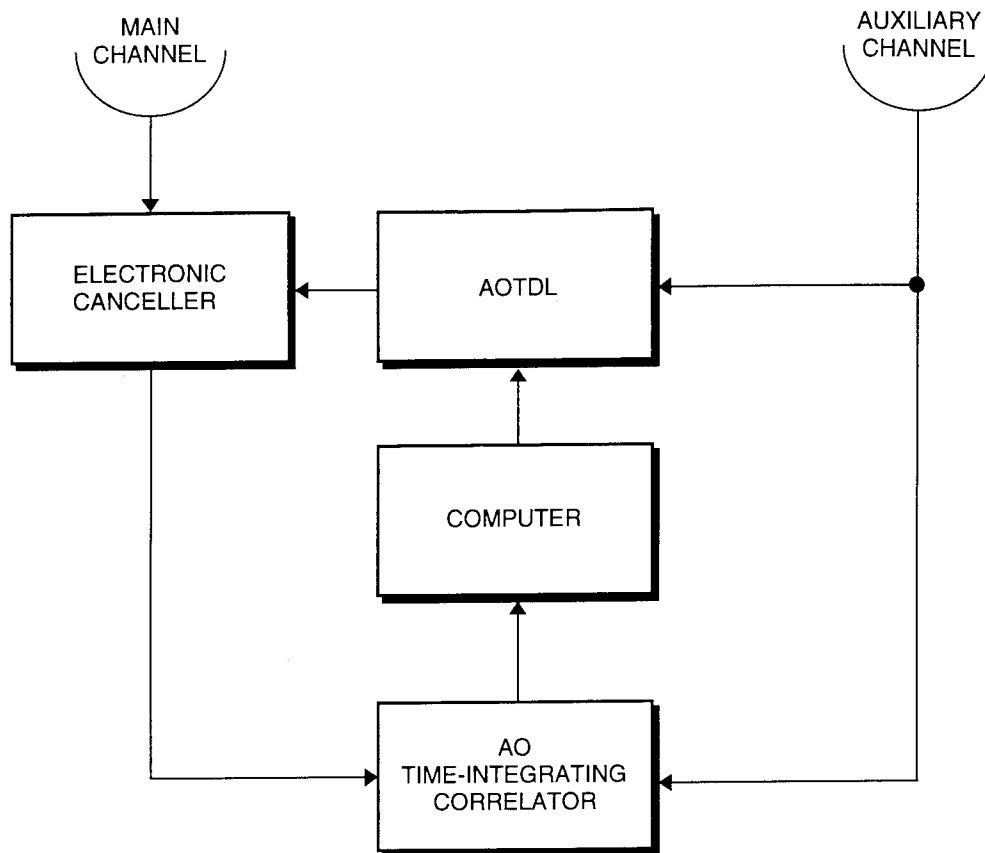


TR-94-3185-A003

**Figure 3-31. Electronic Canceller Configuration**

Part of the effort during the first onsite support trip in February was to rebuild the electronic canceller using the new phase comparator and vector modulator. It was found that while the new components improved the operation of the electronic canceller, its operation was still unstable under some conditions. In order to better understand the source of the instability, a computer model of the electronic canceller was developed that allowed the parameters to be varied to see how they would affect the operation of the loop. A listing of the MATLAB program used in the analyses is contained in Appendix B.

The model included the basic components of the electronic canceller (phase comparator, vector modulator, integrators, and summer) and models of the cables, or paths, connecting the components. The specific paths modeled were the error signal path (see **Figure 3-31**), the AOTDL mixing path, and the phase control path. These paths were represented by phase shifts. Interest was not in the actual phase shifts in the paths, but in the difference between the phase shift in the AOTDL mixing path and the sum of the phase errors in the phase control and error signal paths. Therefore, this difference was a parameter in the simulation.

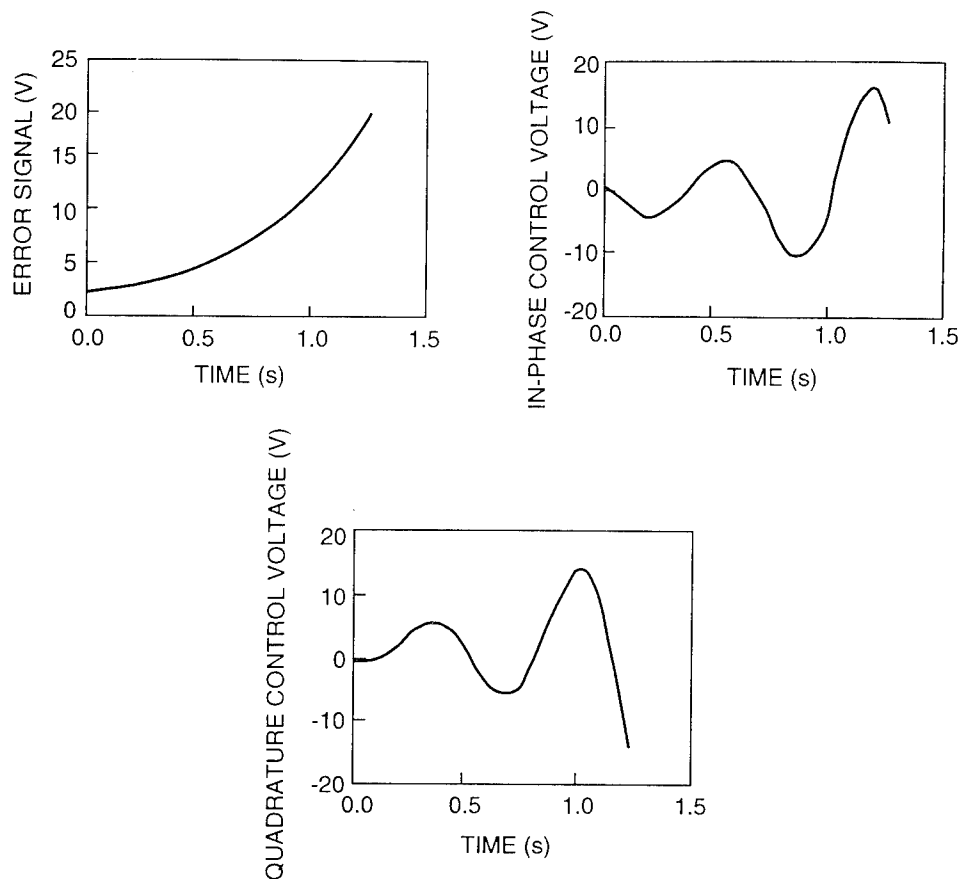


TR-94-3184A-A003

**Figure 3-32. MADOP With Electronic Cancellor**

Sample results of the simulation runs are shown in **Figures 3-33 through 3-35**. In the figures, the upper left plot is the error signal,  $e(t)$ , of **Figure 3-31**. The upper right plot is the in-phase component of the control voltage out of the integrator, and the lower left plot is the quadrature component of the control voltage out of the integrator. The AOTDL and main channel signals are sinusoids at the same frequency.

**Figure 3-33** corresponds to the case where the phase difference indicated above is greater than  $90^\circ$ . Notice that for this case the electronic canceller is unstable. When the phase error is between  $45^\circ$  and  $90^\circ$  (see **Figure 3-34**) the canceller is stable but the control voltages are very oscillatory. The operation becomes more reasonable when the phase error is below  $45^\circ$  as indicated in **Figure 3-35**.



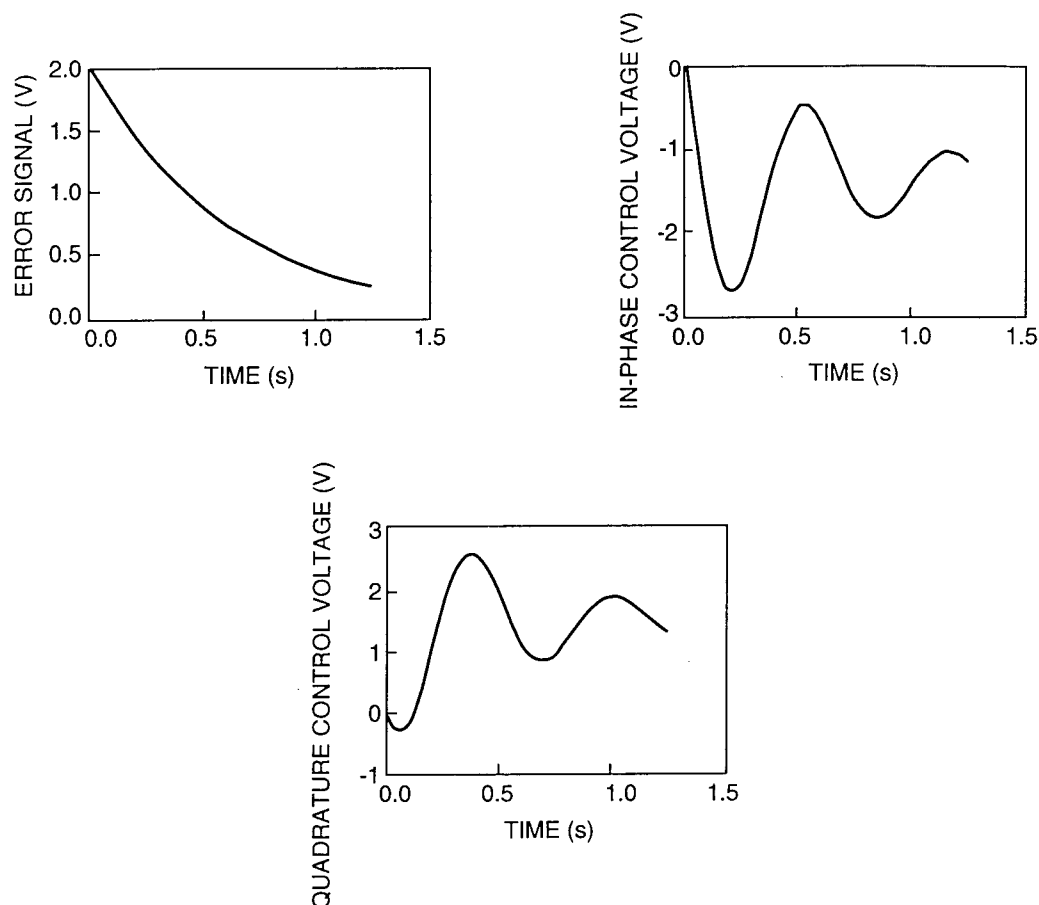
TR-94-3187-A003

**Figure 3-33. Response of Electronic Canceller for a Phase Difference of  $100^\circ$**

The model results indicate that the difference in phase shifts between the AOTDL mixing path and the combined error signal and phase control paths cannot exceed  $90^\circ$  if the loop is to be stable. Based on hardware experiments, it appears that the phase shifts depended on the lengths of the cables connecting the devices in the paths, the voltage standing wave ratios (VSWRs) of the devices, and the phase shifts in the devices. We reached these conclusions by interchanging cables and devices.

It was also determined that the dynamic range of the integrators affected the performance of the electronic canceller in that if the integrators saturate, they may not be able to recover before the error signal grows beyond a recoverable point. This is shown in **Figure 3-36**, which is a case similar to that for **Figure 3-34** except that the integrator outputs are limited to 1 V, which was the saturation limit on the actual integrators. In **Figure 3-36**, it will be noted that the in-phase control voltage has saturated at  $-1$  V. Before saturation the error signal is headed toward zero at a rapid rate. After saturation the error signal rate slows and the error signal appears to be headed toward

a value of about 1.65 V. The observation from this experiment is that the dynamic range of the integrator should be extended.



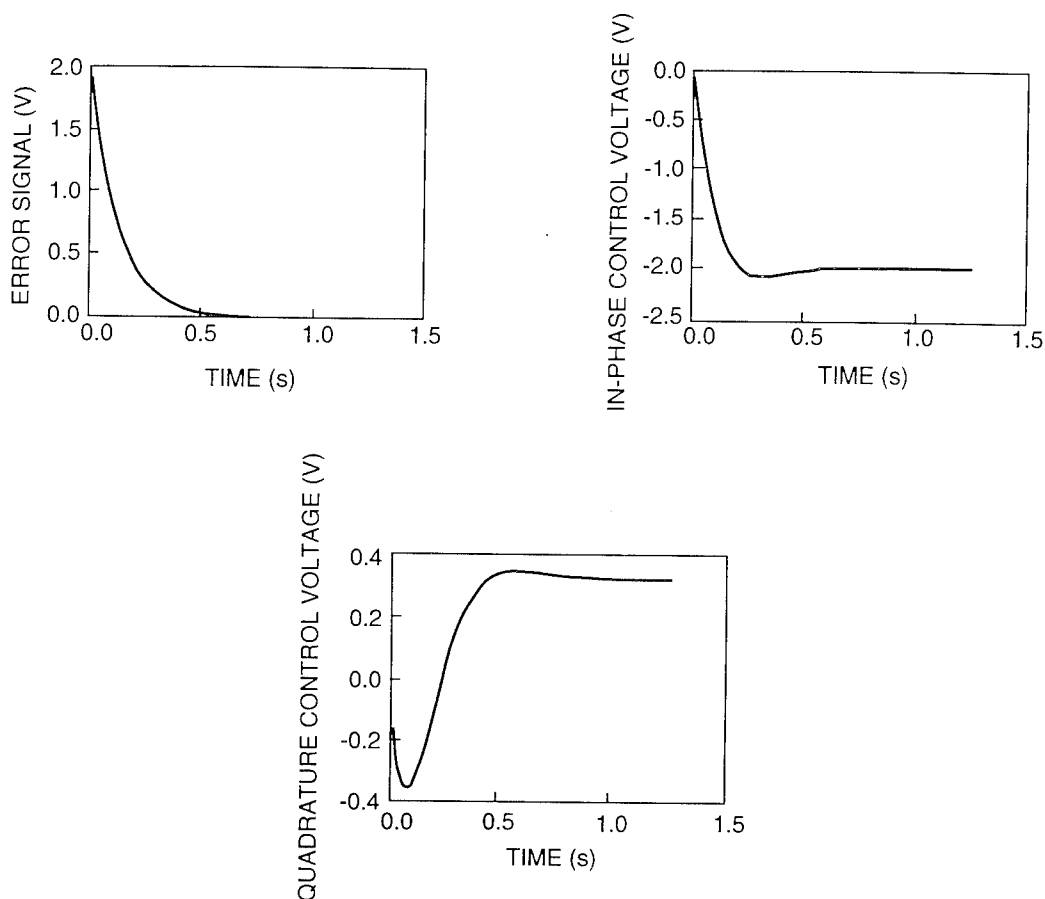
TR-94-3188-A003

**Figure 3-34. Response of Electronic Cancellor for a Phase Difference of  $80^\circ$**

Preliminary tests of the vector modulator indicated that it could introduce considerable phase error in the phase control path. The results of the preliminary tests are shown in **Figures 3-37 through 3-39**. These figures contain plots of calculated and measured phase for the vector modulator, versus voltage levels on the quadrature input to the vector modulator. Each curve corresponds to a different value of voltage on the in-phase input. The measured phase is normalized so that -1 V on the in-phase input and 0 V on the quadrature input yielded  $180^\circ$  of phase shift. This normalization was necessary because of calibration requirements.

Examination of the three sets of plots indicates that the phase shift of the vector modulator only approximates the expected phase shift. The phase errors in the measured data range between  $+5^\circ$  and  $-35^\circ$ . Also, the error is somewhat erratic. This amount of phase error can be

accommodated by the compensation loop. However, the erratic behavior of the actual vector modulator phase shift relative to the expected phase shift may cause some erratic behavior of the compensation circuit.



TR-94-3189-A003

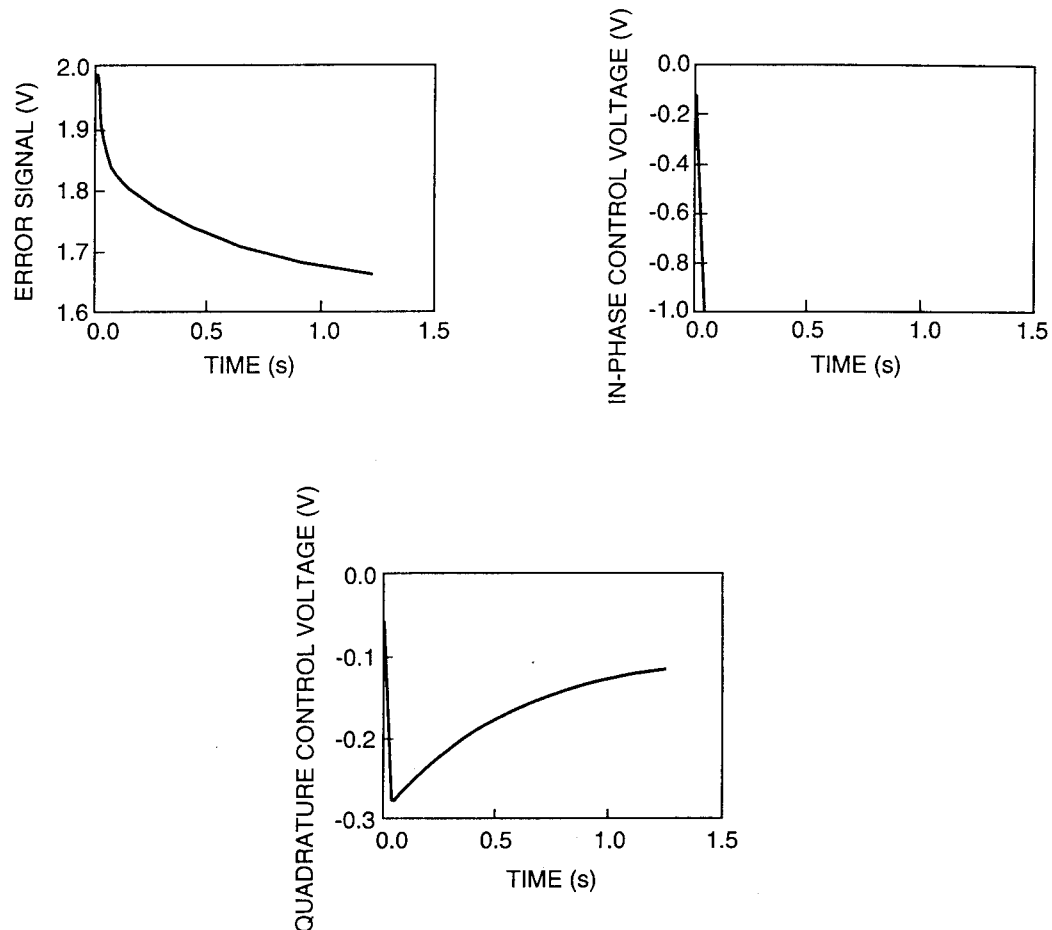
**Figure 3-35. Response of Electronic Canceller for a Phase Difference of  $40^\circ$**

The phase comparator may be another source of error in the electronic canceller. However, it was not characterized during the first onsite visit because of time constraints.

The observations of the first onsite support trip are as follows: the dynamic range of the integrators needs to be extended, and the electronic canceller circuit had to be further compacted to reduce lead lengths and to reduce the phase errors introduced by the longer leads.

During the second onsite support trip the integrator circuits were rewired and made more compact; also, the supply voltage to the integrators was increased from  $\pm 10$  V to  $\pm 15$  V. These changes increased the dynamic range of the integrators from  $\pm 1$  V to  $\pm 10$  V. In addition, the electronic canceller was assembled using barrel connectors instead of cables, wherever possible, to

attempt to compact the circuit. The result of this was that the stability problems associated with the electronic canceller on the first trip were virtually eliminated. The electronic canceller worked well for the remainder of the second onsite support trip and throughout the third onsite support trip in August.

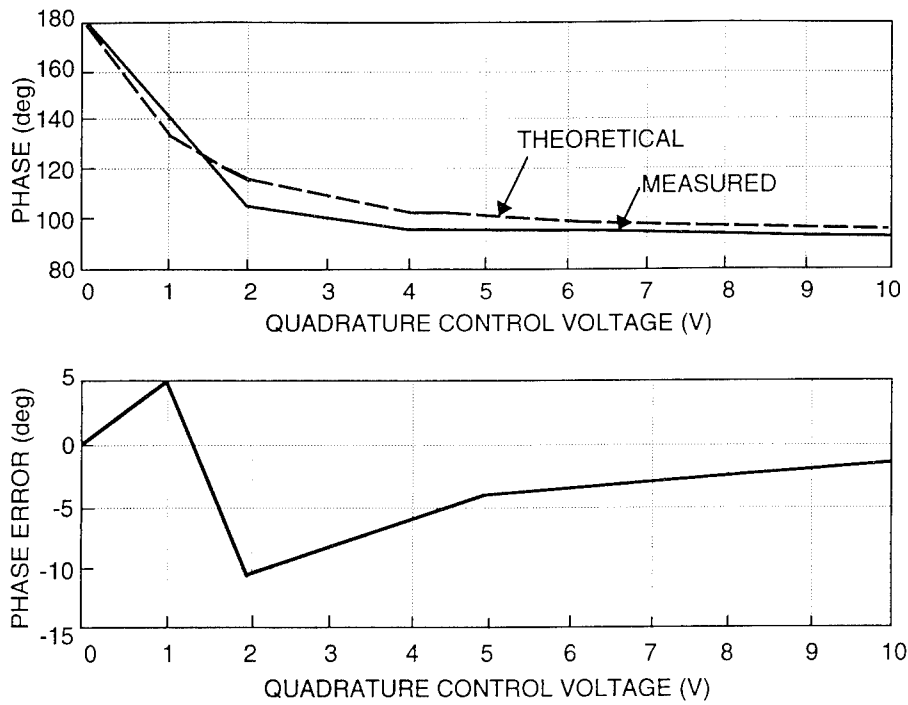


NOTE: INTEGRATORS LIMIT AT  $\pm 1$  V, PHASE DIFFERENCE =  $80^\circ$

TR-94-3190-A003

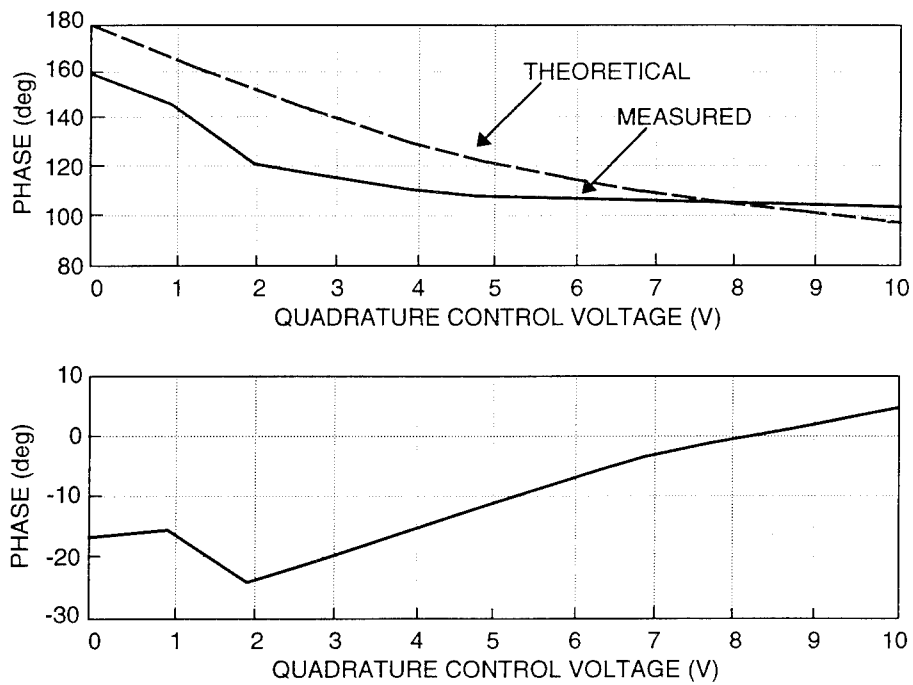
**Figure 3-36. Effects of Saturation on Electronic Canceller Performance**

During the second onsite support trip, an amplifier and the phase comparator were overloaded (see Section 4.1). To avoid this situation we reallocated some of the gains in the circuit. In particular, we effectively removed the gain before the phase comparator and included two 33-dB, direct current (dc) amplifiers directly before the integrators. A block diagram of the implementation of the 33-dB amplifiers is shown in **Figure 3-40**. This modification resolved the overloading problem and seemed to further enhance the performance of the electronic canceller. The electronic canceller was not modified during the third onsite support trip.



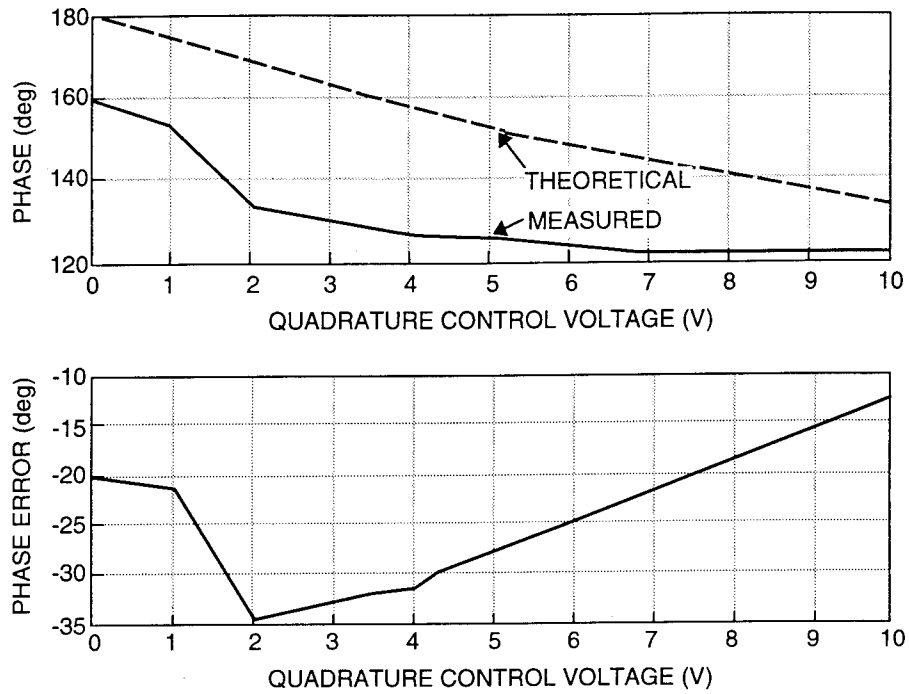
TR-94-3191-A003

**Figure 3-37. Phase Errors of Vector Modulator: In-Phase Control Voltage = -1 V**



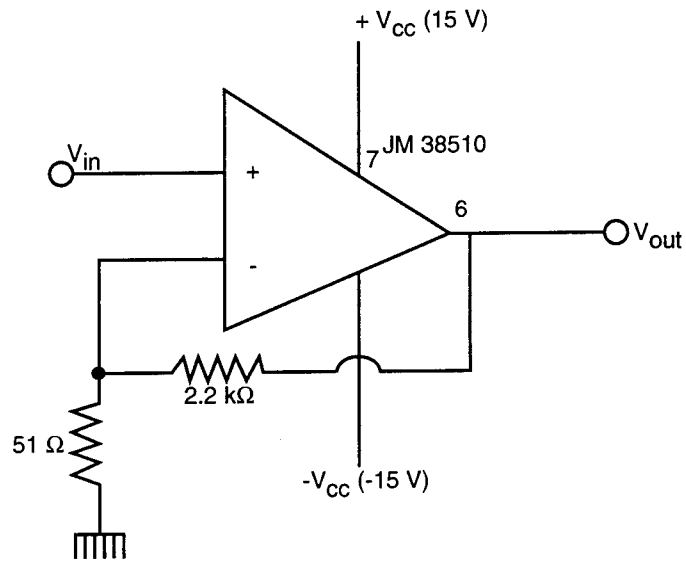
TR-94-3192-A003

**Figure 3-38. Phase Errors of Vector Modulator: In-Phase Control Voltage = -5 V**



TR-94-3193-A003

**Figure 3-39. Phase Errors of Vector Modulator: In-Phase Control Voltage = -10 V**



TR-94-3194-A003

**Figure 3-40. Schematic Diagram of dc Amplifier With 33 dB of Gain**

### **3.5 DIGITAL COMPUTER INTERFACE**

The primary work on the digital computer interface was performed by RL personnel. Accomplishments achieved during this effort related to the digital computer interface included:

1. Insertion and testing of a frequency synthesizer card that provides four independent tones across the AOSLM tap frequency band. These tones were generated using the tap frequency estimation algorithms to command the synthesizer card;
2. Improvement of the algorithms for generating the tap frequency estimates. This was primarily achieved through the implementation of detection processing (squaring and low-pass filtering) prior to peak estimation; and
3. Improvement in the speed of the processing through software enhancements and options to allow fewer graphical display options.

During future MADOP test activities, the digital computer interface will be improved through the purchase of additional high-speed computer hardware, the continued development of algorithms for tap frequency estimation, and the possible use of analog detection circuitry to reduce the demands on the digital interface.

## 4. MADOP SYSTEM TESTING

A major emphasis in this program was the testing of the MADOP under laboratory conditions and while integrated within the C-band radar testbed. These results are presented in this section.

### 4.1 LABORATORY TESTING

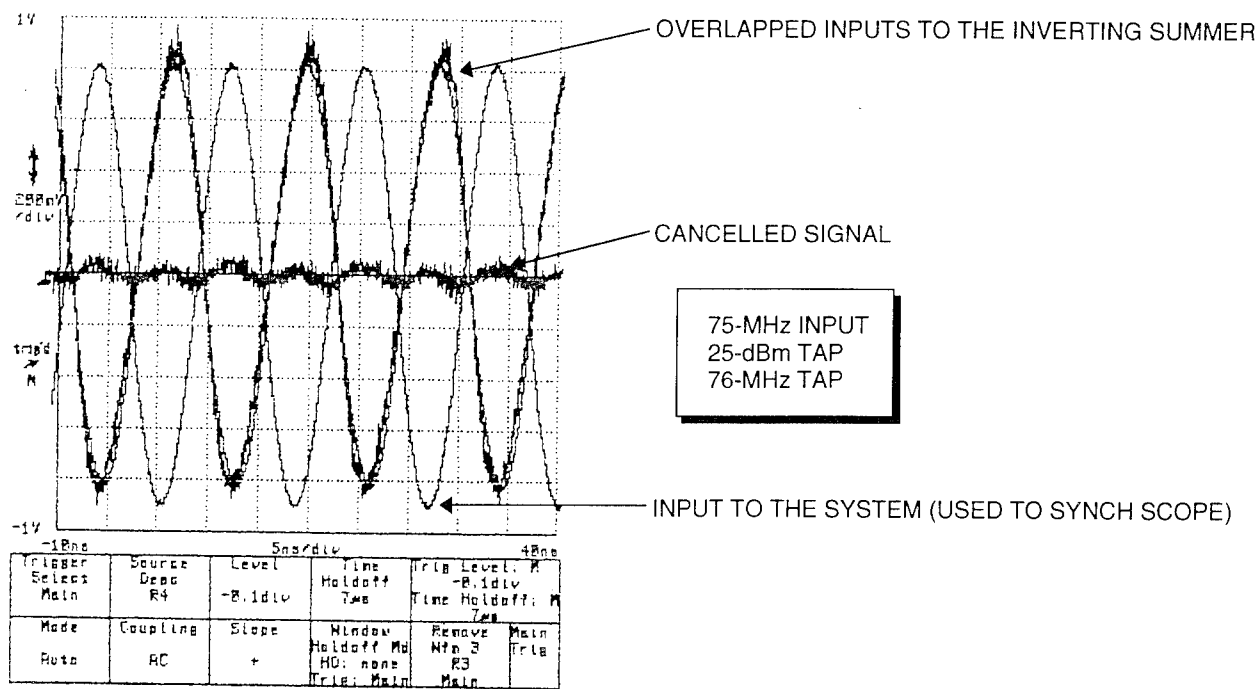
#### 4.1.1 Onsite Support Period One

During the first period of onsite support, measurements of the signal cancellation with the electronic canceller integrated into the system were performed with limited success. Most of the limitation on cancellation was attributed to the noise generated in the non-optimized electronic canceller circuit. Also, the electronic configuration, when inputting waveforms to the AO correlator and AOTDL subsystems, introduced additional noise, which can be reduced significantly with more careful RF configuration.

The test signals were first generated at the AOTDL subsystem and did not enter the AO correlator portion of the system. **Figure 4-1** shows a plot of the cancellation of a 75-MHz tone input to the AOTDL and as the reference signal into the electronic canceller circuit. The tap frequency was 76 MHz at a power of 25 dBm. **Figure 4-2** shows a similar measurement for a 77-MHz tone with the tap power reduced to 19 dBm. At this frequency, the electronic canceller configuration was on the verge of instability.

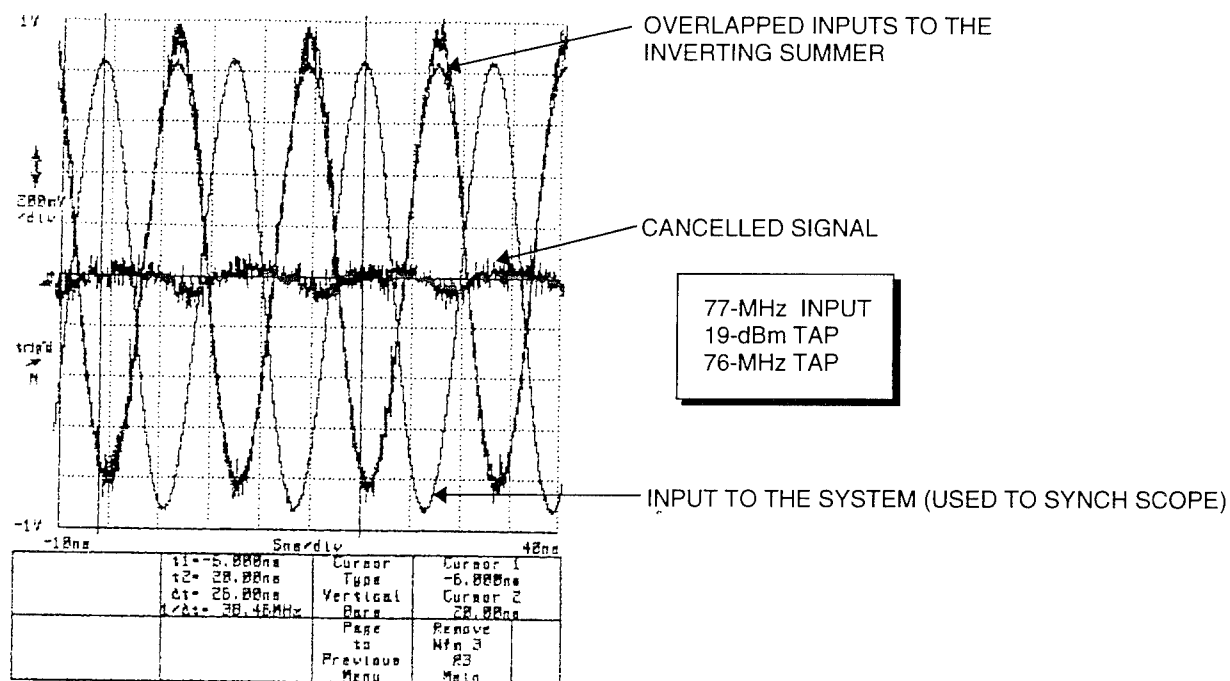
The IntraAction driver was then used with a 1.5-MHz tone input to create a DSB-SC waveform as the input to the AOTDL subsystem. **Figure 4-3** shows the spectrum of this two-tone waveform, and **Figure 4-4** shows the resultant cancellation.

Finally, the LeCroy arbitrary function generator (AFG) was used as an input to the IntraAction driver to create a 500-ns (2-MHz bandwidth) pulsed waveform. This waveform was then split to form the input to the AO correlator subsystem, which performed an autocorrelation, and as the input to a second splitter that formed the AOTDL input and the main channel signal. **Figures 4-5(a) and (b)** show the resultant cancelled pulse and the diagram of the signal configuration, respectively. The two BAW delay lines were inserted to account for the differential delay inherent in the AOTDL subsystem. **Figure 4-6** shows the reference pulse shape. **Figures 4-7 and 4-8** show the reference and cancelled pulse spectra, respectively, and reflect approximately 10-dB of cancellation.



TR-94-3122-A003

**Figure 4-1. Tone Cancellation, Signals Generated at AOTDL**



TR-94-3123-A003

**Figure 4-2. Tone Cancellation, Signals Generated at AOTDL, Reduced Tap Power**

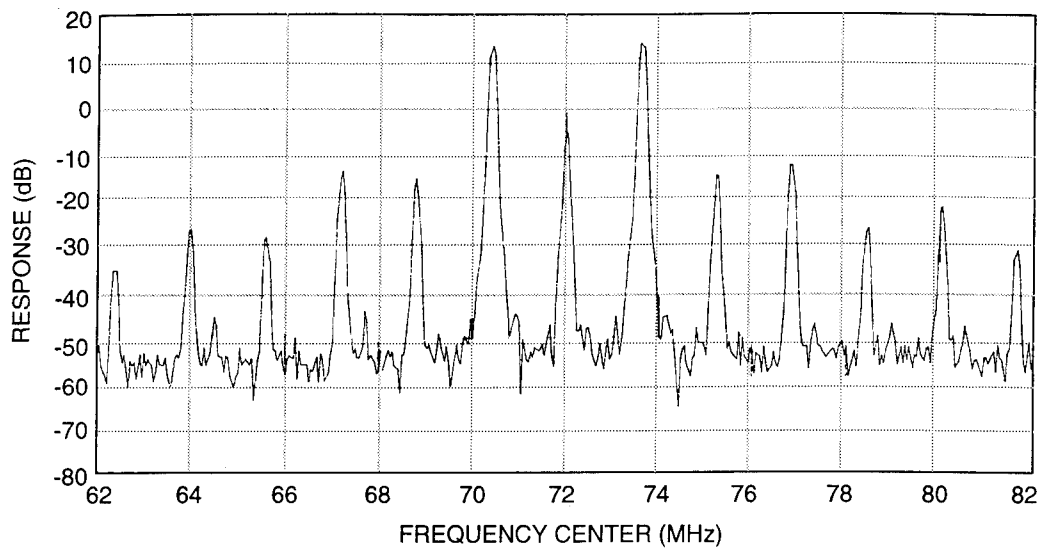


**Figure 4-3. DSB-SC Spectrum**

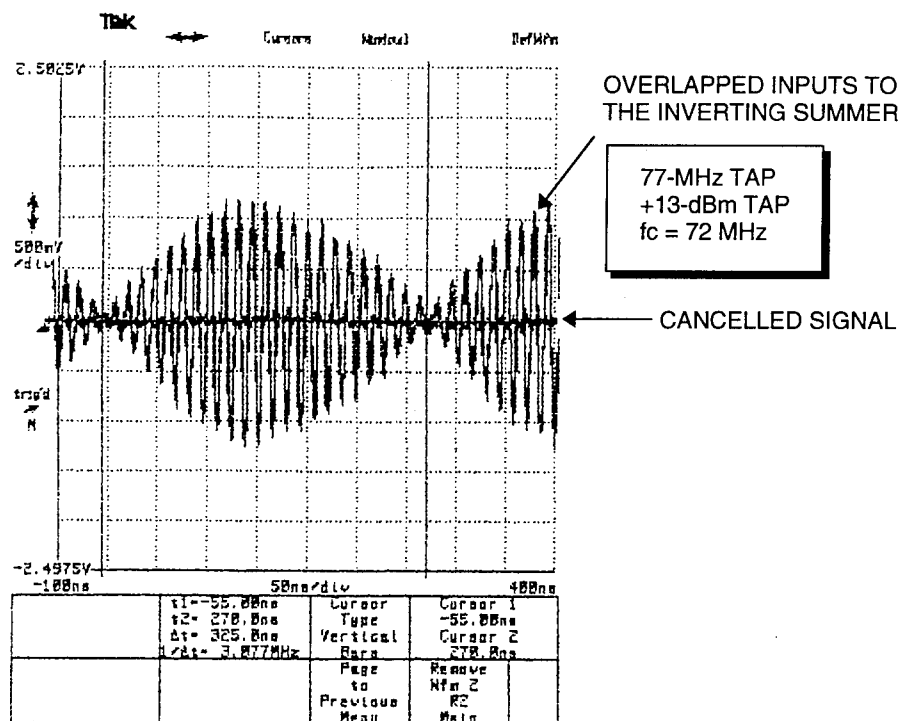
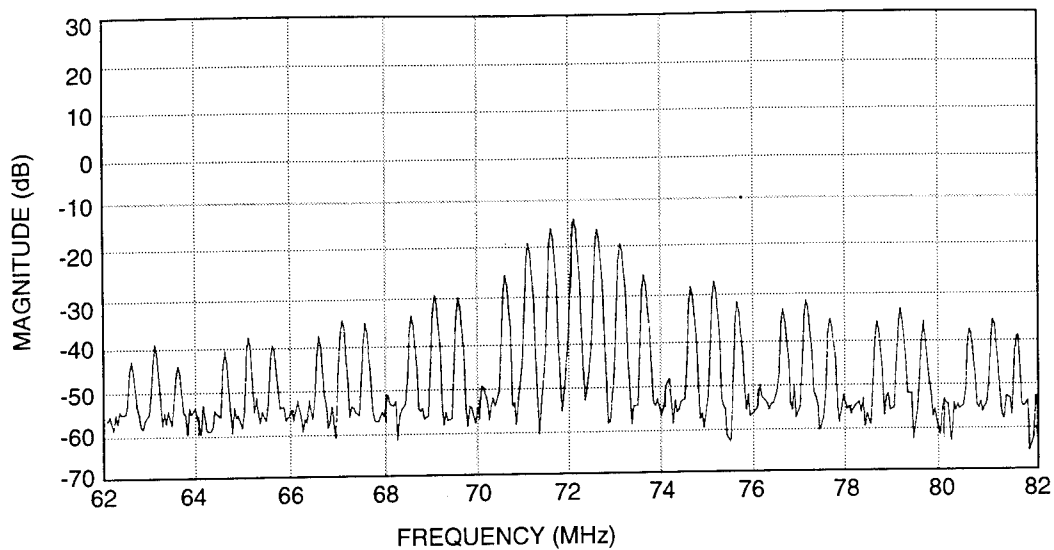


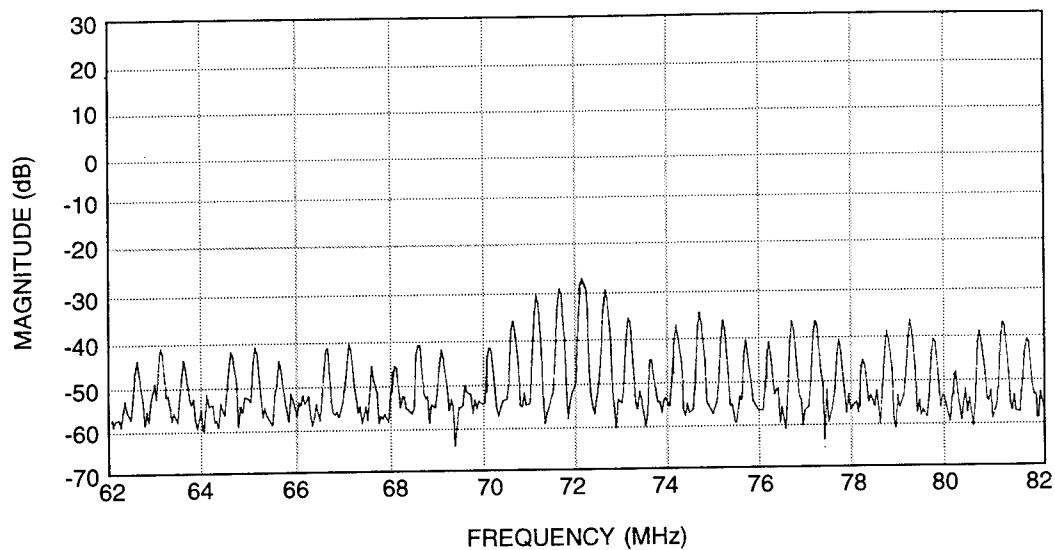
**Figure 4-4. DSB-SC Cancellation, Signals Generated at AOTDL**





TR-94-3129-A003

**Figure 4-7. Reference Pulse Spectrum**



TR-94-3128-A003

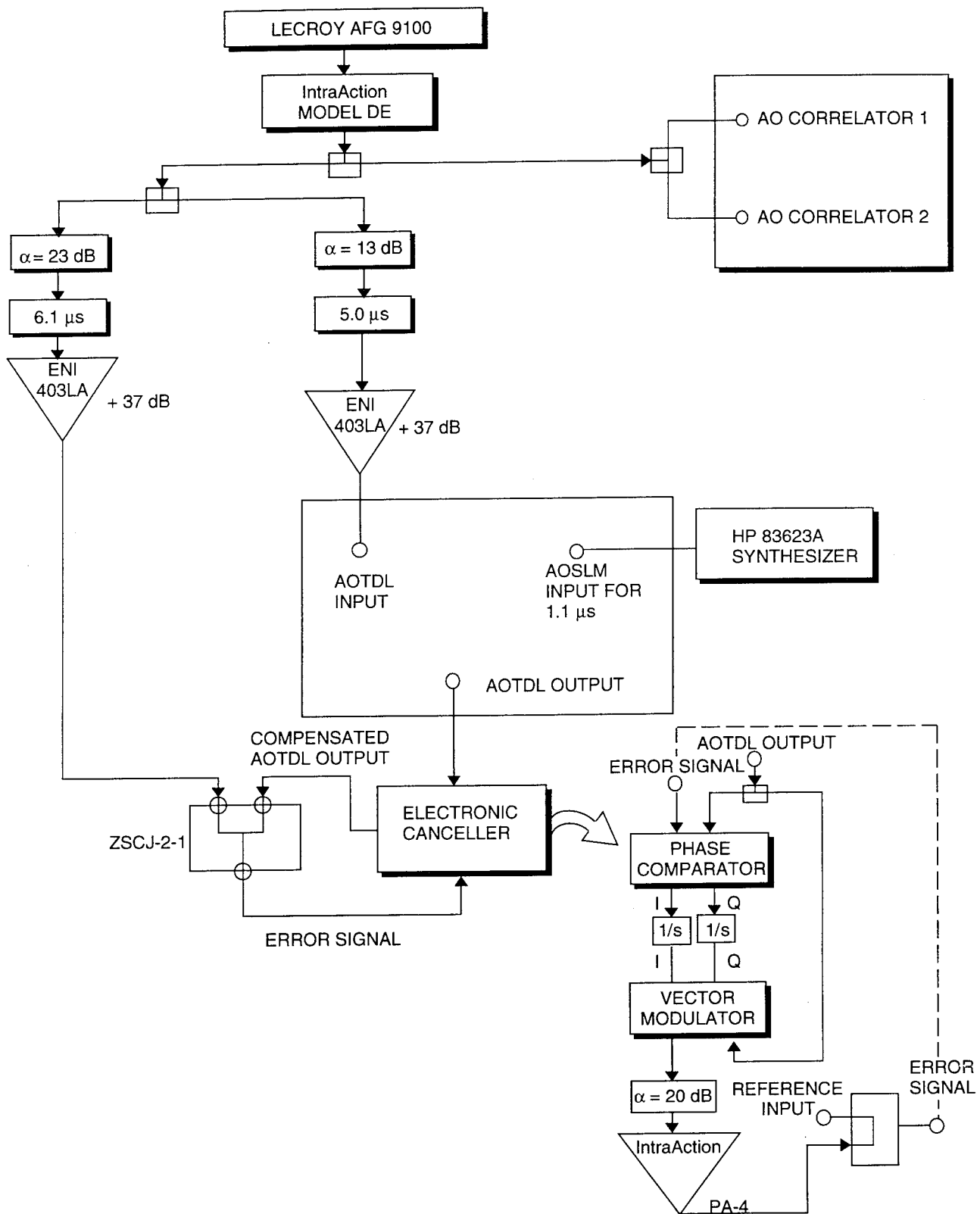
**Figure 4-8. Cancelled Pulse Spectrum**

#### 4.1.2 Onsite Support Period Two

During the second period of onsite support, the integrated MADOP system was further tested in the laboratory. The configuration for the initial testing is shown in **Figure 4-9**. Here, a waveform is created at baseband using the Lecroy AFG 9100 and mixed up to the 80-MHz IF in the IntraAction Model DE. This signal is split to simulate both the main and auxiliary channels. The AO time-integrating correlator accepts these two waveforms and performs the coherent cross correlation, feeding this result to the PC. The signal is also split to provide an input to the AOTDL filter, simulating the auxiliary channel, and to the subtractor, simulating the main channel received signal. The output of the AOTDL filter is compensated by the single-loop electronic canceller and input to the subtractor to produce the error signal.

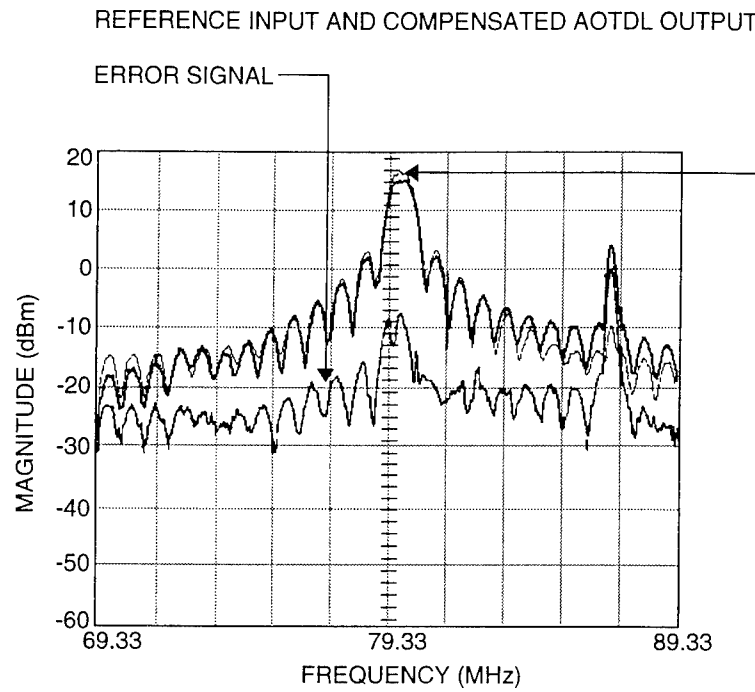
Three representative results are shown in **Figures 4-10 through 4-12**. In each case, there exists a tone at 86.9 MHz that occurs due to the AOSLM tap frequency, which feeds through the system due to optical crosstalk. This tone interference due to the AOSLM tap frequency was reduced during the third onsite support period through the employment of a slow-shear TeO<sub>2</sub> AOSLM. **Figure 4-10** shows the cancellation results for a 0.6- $\mu$ s pulse (50% duty cycle), demonstrating approximately 25 dB of cancellation. **Figure 4-11** shows similar results for a 1.2- $\mu$ s pulse, demonstrating approximately 20 dB of cancellation. **Figure 4-12** shows cancellation of approximately 30 dB for a tone at the 80-MHz IF, but we see the effect of the AOSLM feedthrough at the 86.9-MHz AOSLM tap frequency and the intermodulation product at the frequency 83.5 MHz.

After this initial testing, it was decided to add gain to the single-loop electronic canceller circuit to achieve improved performance. This increased gain was achieved through the use of an AM4001 differential amplifier inserted in place of the ZSCJ-2-1 subtractor, as shown in **Figure 4-13**. Note also in this figure that a simulated target return tone was added to the main channel signal during some tests. **Figure 4-14** shows the main channel signal composed of a jammer at 73.25 MHz and the target return at 80.5 MHz, with an S/J ratio of -10 dB (note that the target return was inadvertently put after a directional coupler so the plot actually shows a 10-dB smaller S/J ratio). **Figure 4-15** shows the resultant cancelled signal, demonstrating a S/J improvement of approximately 35 dB. This was corrupted by a rise in the noise floor of approximately 10 dB and the appearance of a number of harmonics, due primarily to the feedthrough of the AOSLM tap frequency and the increased intermodulation products [from increased (somewhat nonlinear) system gain].



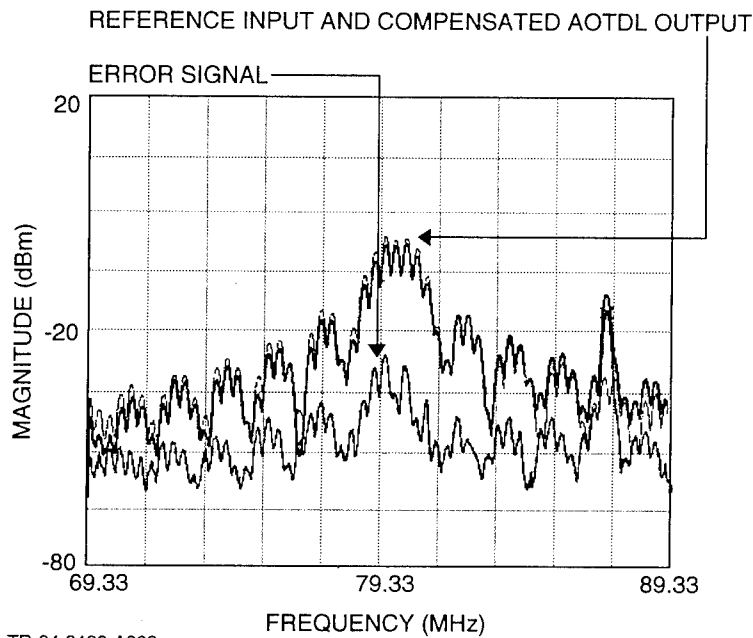
TR-94-3130-A003

**Figure 4-9. MADOP Configuration for Initial Testing During Onsite Support Period 2**



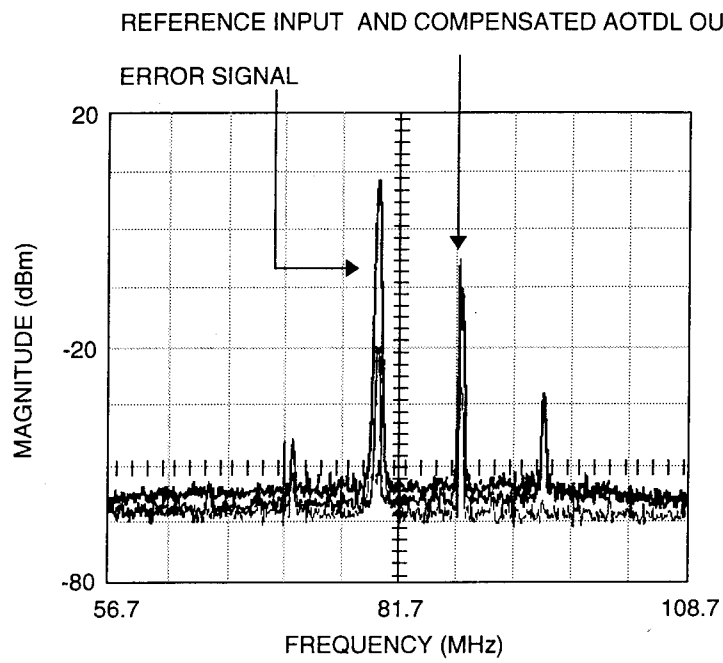
TR-94-3131-A003

**Figure 4-10. 0.6- $\mu$ s Pulse Cancellation**



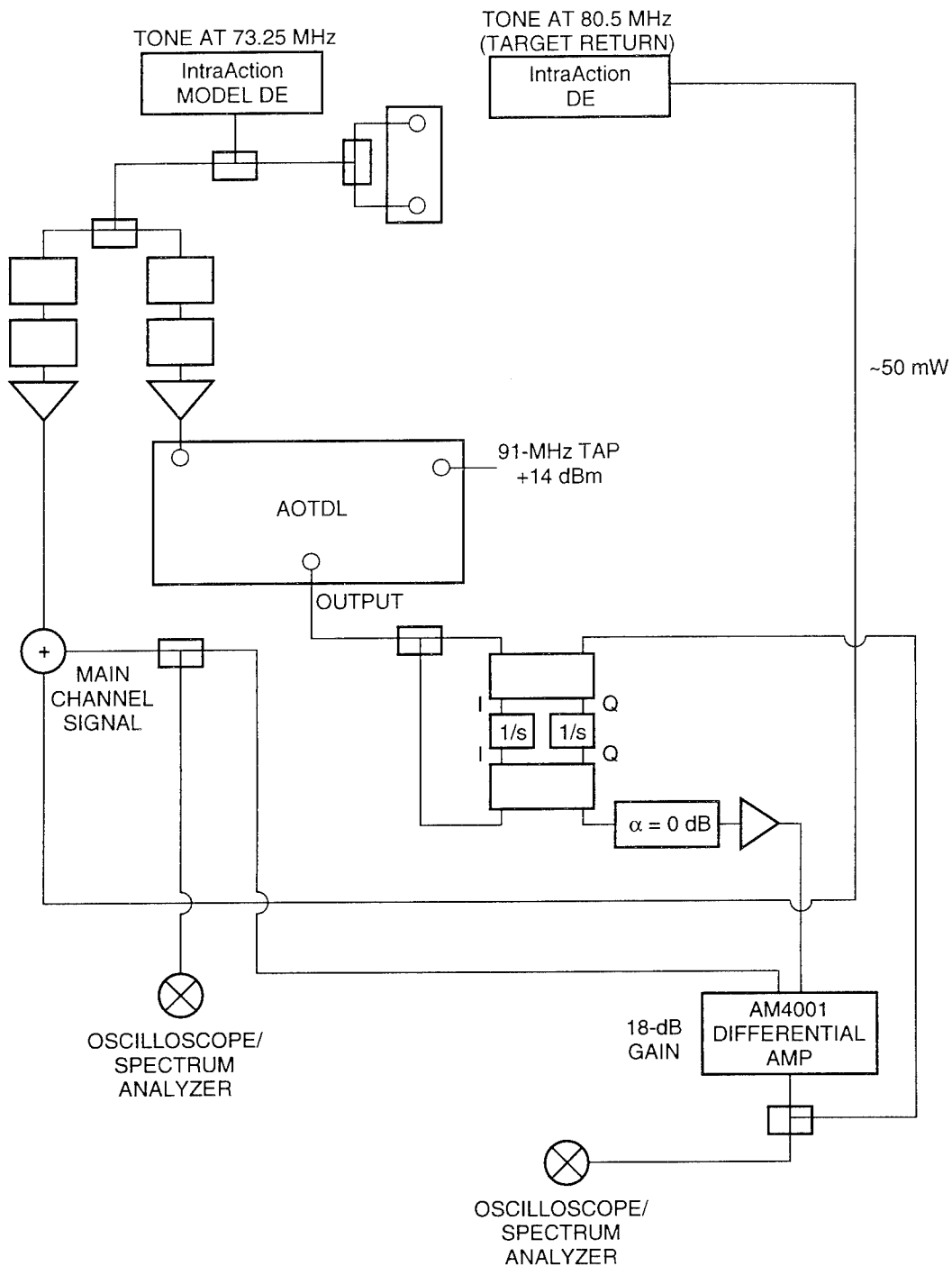
TR-94-3132-A003

**Figure 4-11. 1.2- $\mu$ s Pulse Cancellation**



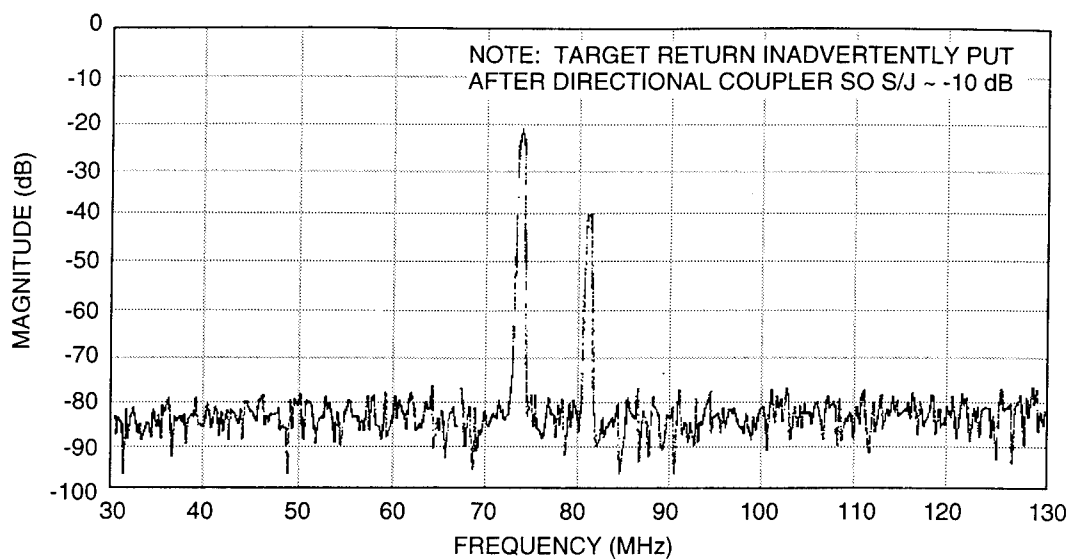
TR-94-3133-A003

***Figure 4-12. 80-MHz Tone Cancellation***



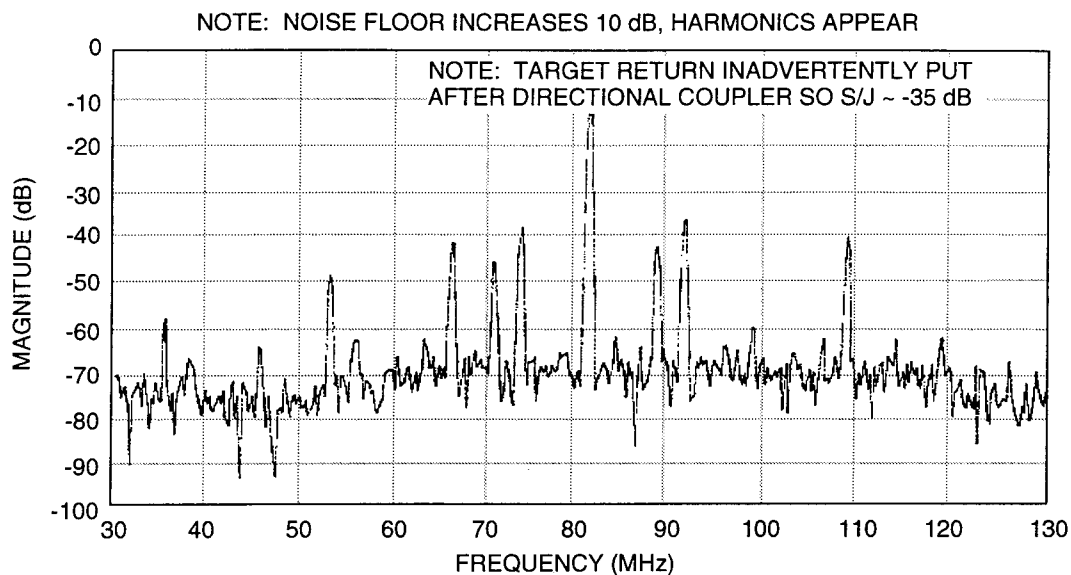
TR-94-3134-A003

**Figure 4-13. Setup With Tektronix AM4001 Differential Amp**



TR-94-3135-A003

**Figure 4-14. Main Channel Signal Containing Jammer at 73.25 MHz and Target Return at 80.5 MHz**



TR-94-3136-A003

**Figure 4-15. Error Signal Showing SJR ~25 dB**

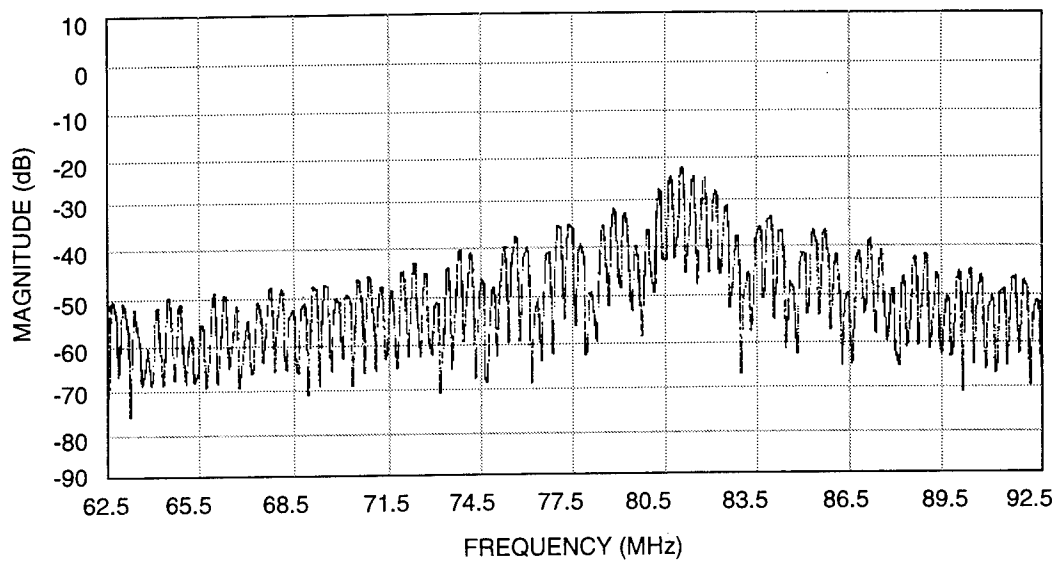
Shortly after this testing, the AM4001 differential amplifier ceased operation, which was likely due to the large power inputs when the system became unstable. This device was removed from the circuit, and further cancellation results were obtained. **Figures 4-16 and 4-17** show results for a 2-MHz pulse (approximately 20 dB of cancellation), while **Figures 4-18 and 4-19** show the cancellation for a wideband noise jammer input of approximately 17-dB (neither of these cases had an injected signal tone). Finally, a 100-ns pulsed waveform with a 20% duty cycle was input, as shown in **Figures 4-20 and 4-21**. Here the cancellation was approximately 12 to 15 dB across the band.

At this time, the system operation ceased and the problem was traced to the phase comparator. It was determined that it, too, had been overdriven during periods of system instability (note that it occurs after the PA-4 amplifier in the single-loop electronic canceller). It was decided to modify the circuit to add attenuation prior to the phase comparator and to add gain in the dc portion of the circuit prior to the integrators. This preserved the large gain after the I&Q weight integration and vector modulation to allow for effective system operation with relatively small weight voltages. This modification is described in Section 3.4 of this report. At this time, cable lengths were reduced to a minimum within the single-loop electronic canceller, which resulted in improved stability. This is likely due to the decrease in phase shift occurring in the circuit where matching (VSWR) is poor. The resulting system architecture after this modification is shown in **Figure 4-22**. With this architecture, approximately 36-dB cancellation was achieved for a single tone, as shown in **Figures 4-23 and 4-24**.

## 4.2 INTEGRATION WITH THE C-BAND RADAR TESTBED

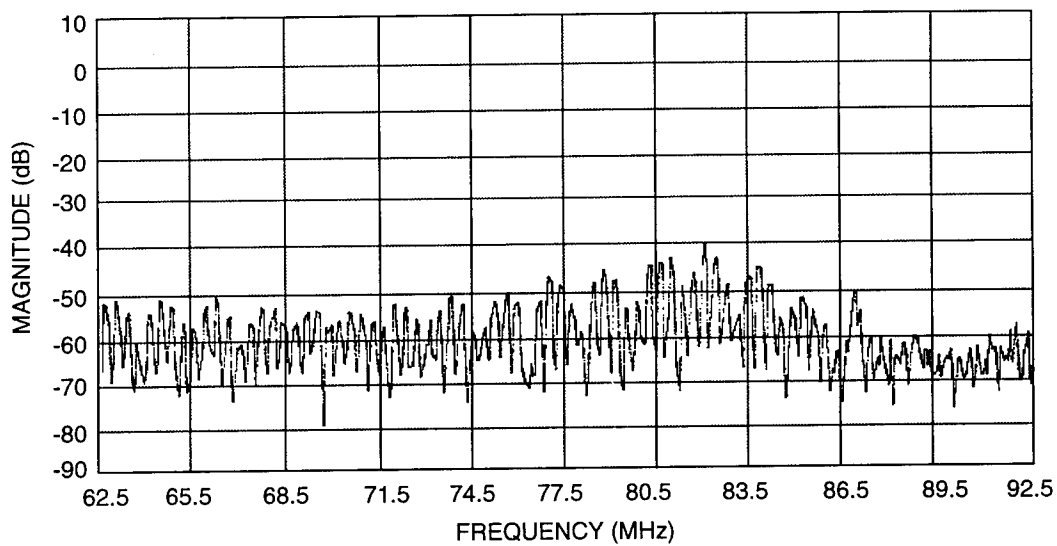
The principle thrust of activities during the August onsite support trip was to interface the MADOP to the RL C-band radar and test the performance of the MADOP using real radar signals. The C-band radar had been identified as a suitable testbed on previous onsite support trips because it possessed most of the features that were needed in the tests.

The RL C-band radar is a phased array radar that is located very close to the Photonics Laboratory. The antenna can be electronically scanned  $\pm 45^\circ$  in azimuth and from  $-1^\circ$  to  $8^\circ$  in elevation. The antenna can also employ a  $360^\circ$  mechanical scan. The antenna polarization can be vertical, horizontal, left-hand circular, or right-hand circular. The antenna gain is 36 dBi on transmit and 32 dBi on receive. The antenna beamwidth, on both transmit and receive, is approximately  $1^\circ$  in azimuth and  $2^\circ$  in elevation.



TR-94-3137-A003

**Figure 4-16. Reference Input for a 2-MHz Pulse**



TR-94-3138-A003

**Figure 4-17. Cancelled Signal for a 2-MHz Pulse**

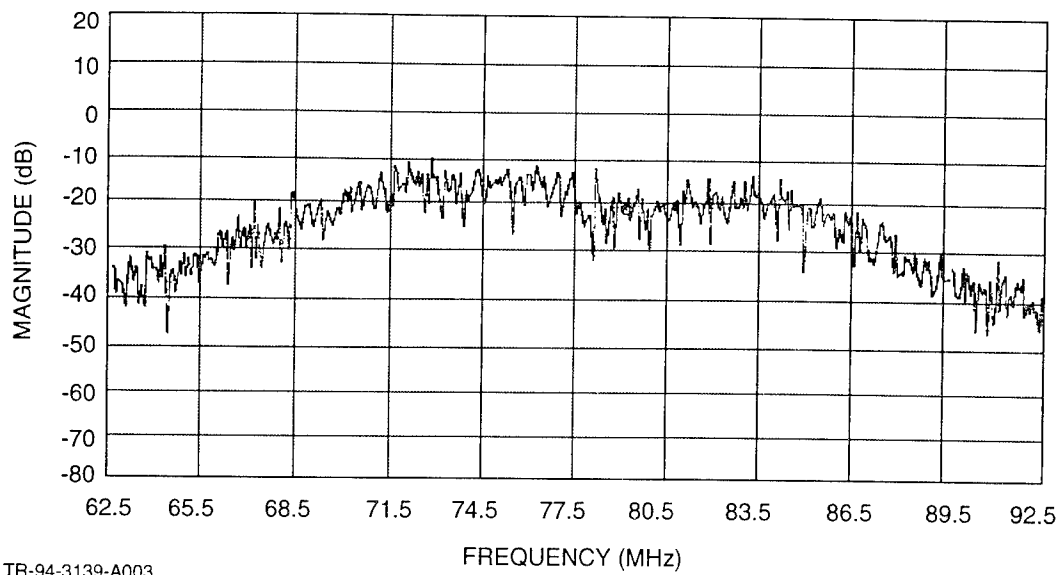


***Figure 4-18. Reference Input Wideband Noise***

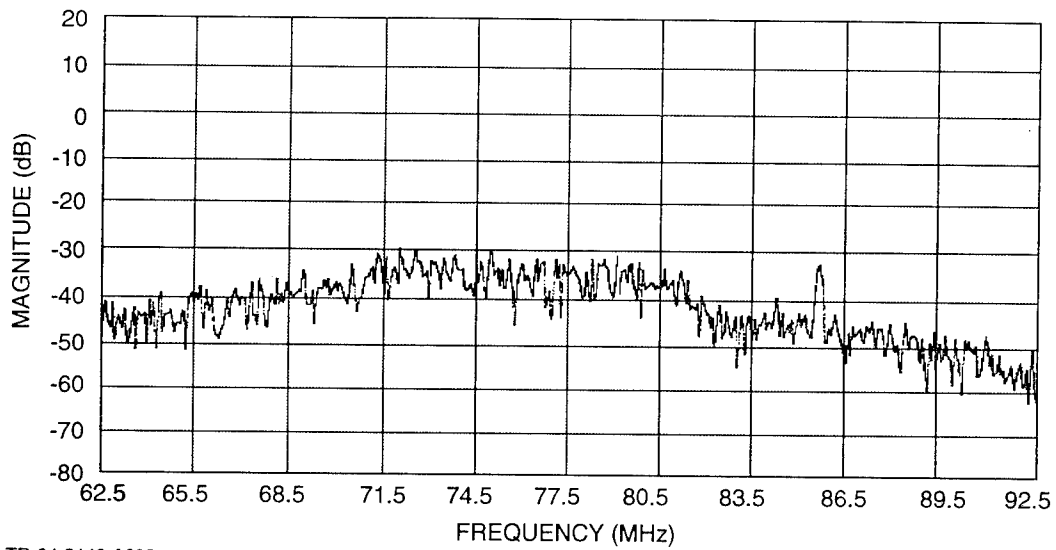


***Figure 4-19. Cancelled Signal for Input Wideband Noise***

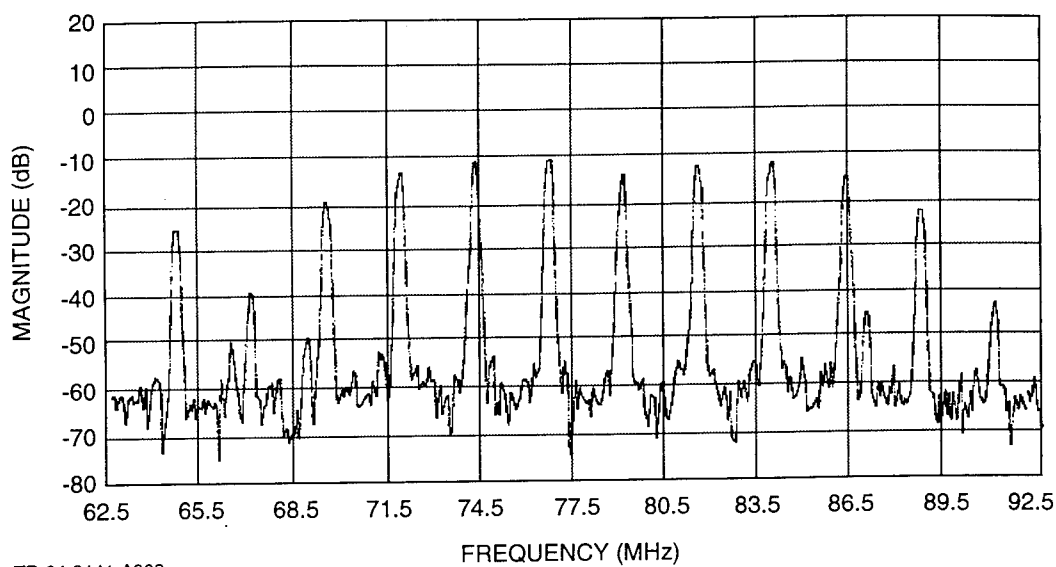


**Figure 4-20. Reference Input for a 100-ns Pulse, 500-ns PRI**

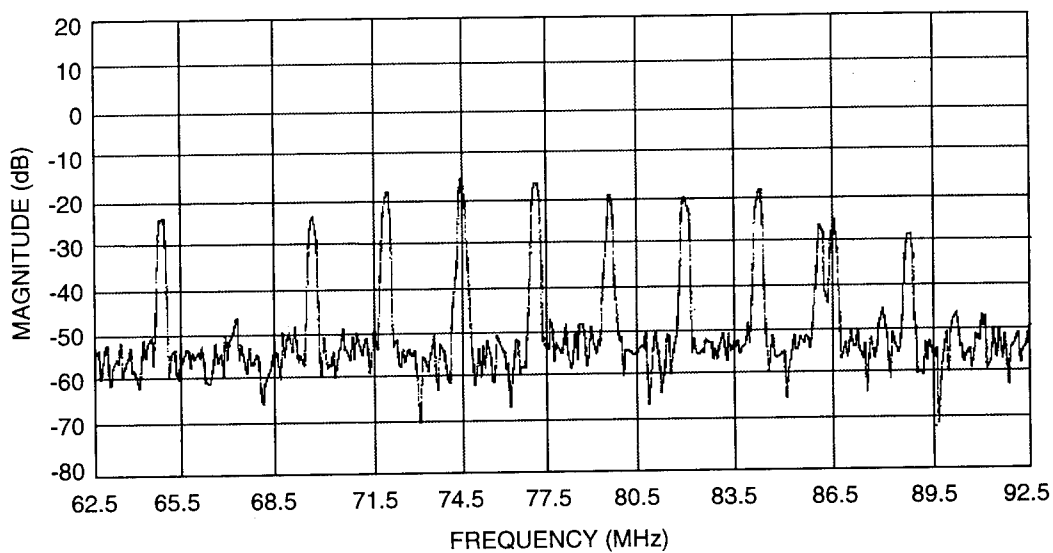


**Figure 4-21. Cancelled Signal for Input 100-ns Pulse**

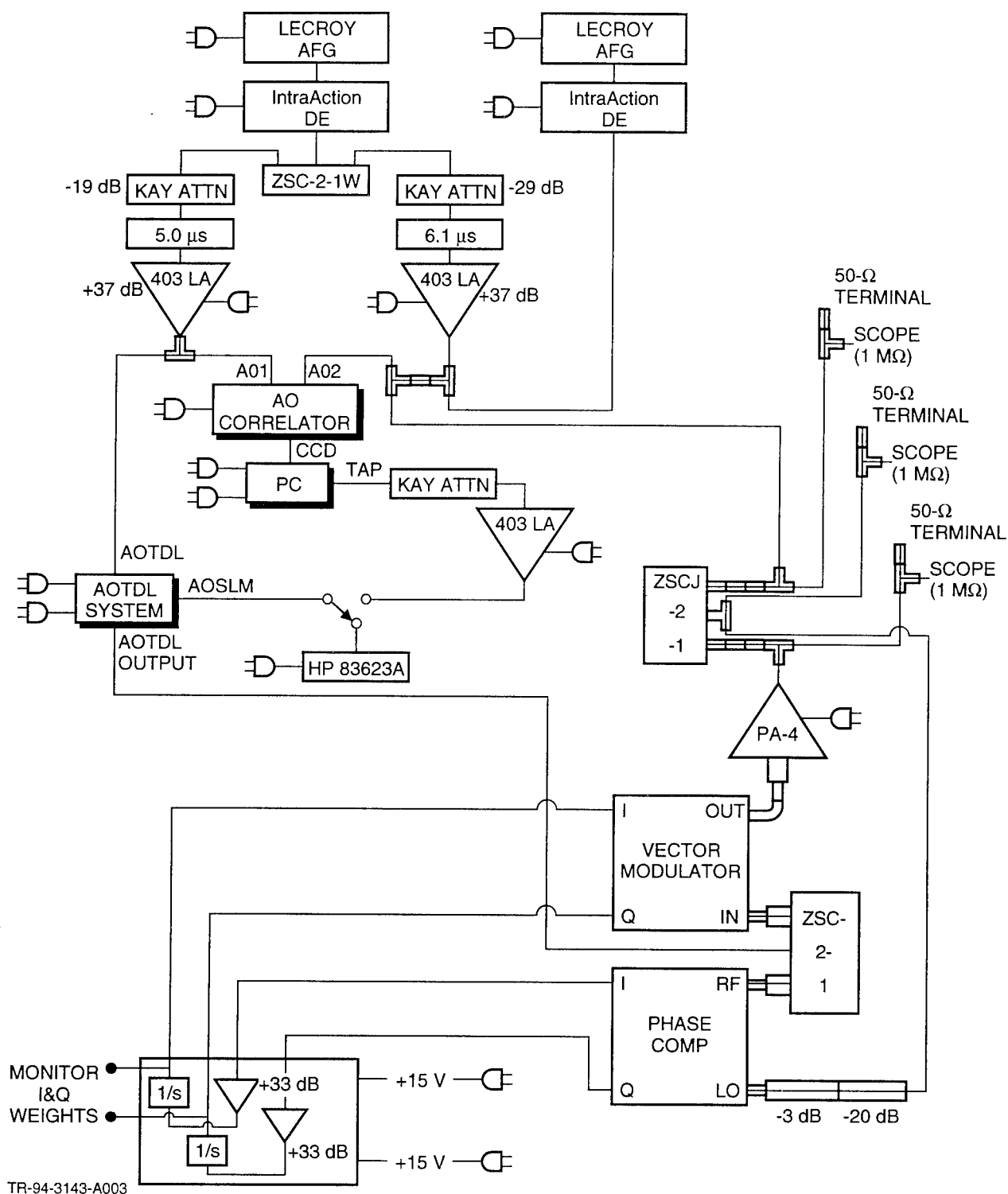
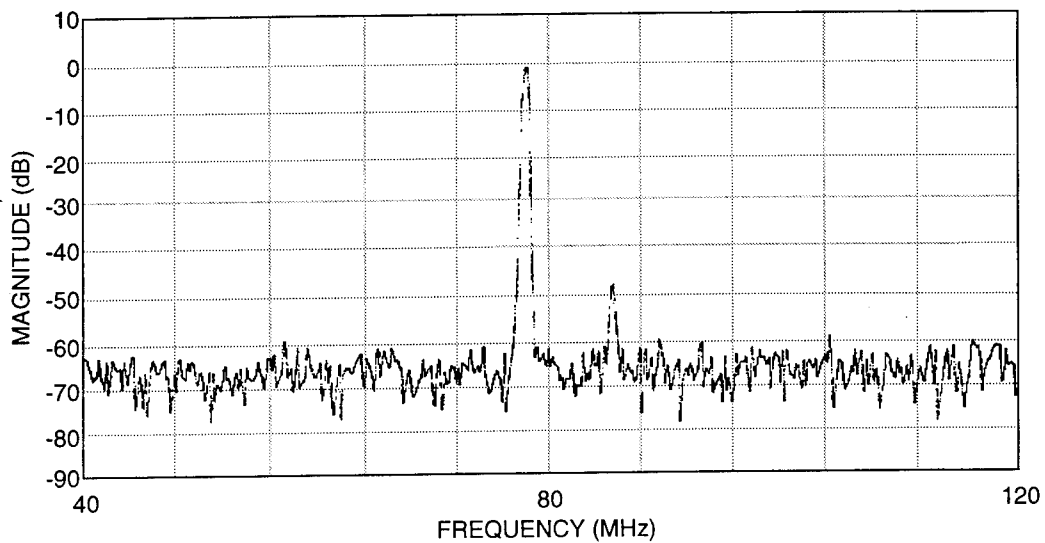
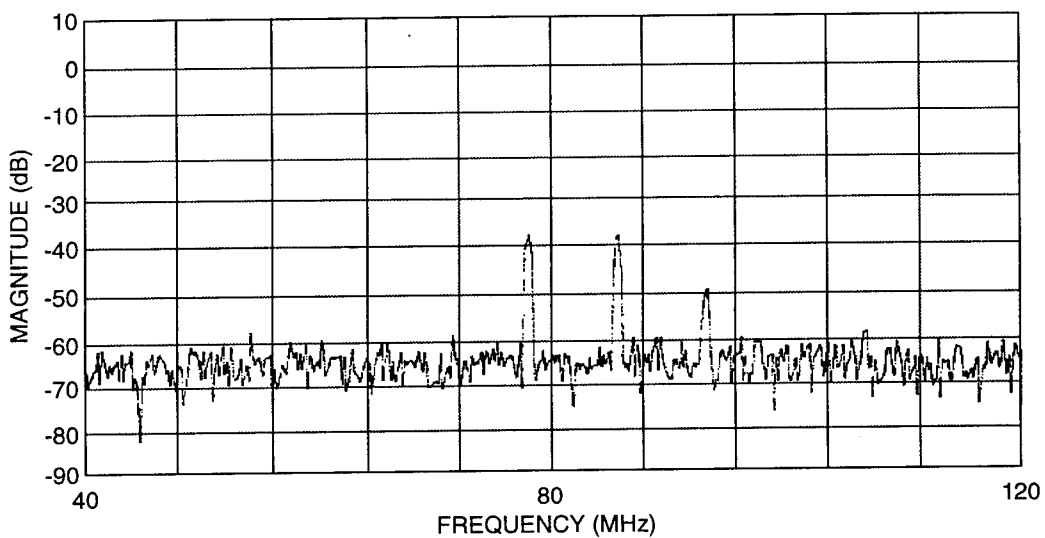


**Figure 4-22. Modified Architecture to Place Gain in dc Circuit Prior to Integrators**



TR-94-3144-A003

**Figure 4-23. Reference Single-Tone Signal**

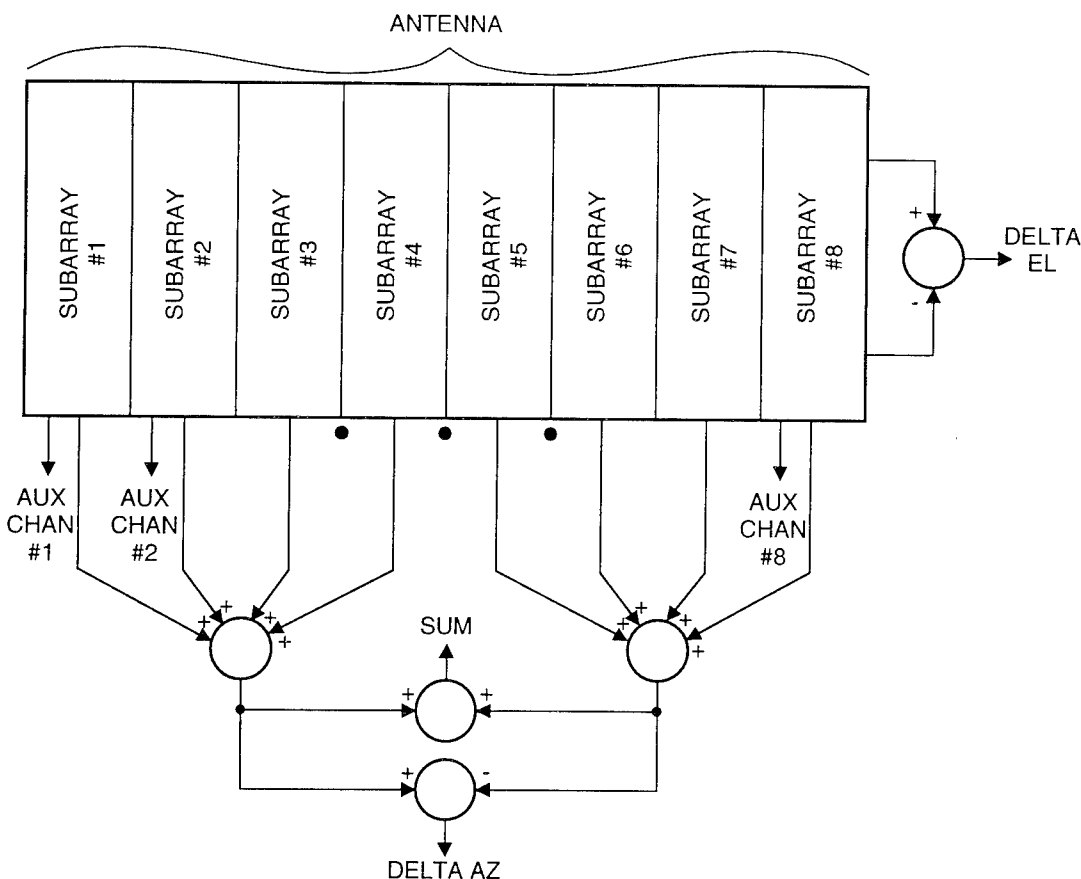


TR-94-3145-A003

**Figure 4-24. Cancelled Signal for Input Single Tone With dc Gain in System Yielding 36-dB Cancellation**

The operating frequency of the radar is 5.65 to 5.9 GHz with a nominal value of 5.775 GHz. The transmit power is approximately 200 kW peak and 8 kW average. The transmitter operates at a 1.8% maximum duty cycle and transmits waveforms with pulsewidths up to 100  $\mu$ s. The transmitter was not used during the tests of the MADOP because it was deemed inappropriate to attempt to track targets during this phase of testing.

The C-band receiver is full monopulse and also has provisions for eight auxiliary channels. The auxiliary channels are obtained from the eight subarrays of the antenna. The subarrays are formed by dividing the antenna into eight vertical sections as indicated in **Figure 4-25**. The subarrays have the same elevation beamwidth of the entire array. The azimuth beamwidth is about eight times the array beamwidth (i.e., approximately  $8^\circ$ ), and the subarray gain is about one-eighth of the entire array gain. The auxiliary channels of the radar could provide the auxiliary channel needed by the MADOP.



TR-94-3146-A003

**Figure 4-25. C-Band Array Structure**

The C-band receiver employs three down conversions and three IFs (see **Figure 4-26**). The first IF is 1265 MHz, the second IF is 592 MHz, and the third IF is 80 MHz. The final bandwidth of the 80-MHz IF is 8 MHz. The sum and difference channels and the eight auxiliary channels have separate IF amplifiers. Furthermore, the outputs of these IF amplifiers are available through 50- $\Omega$  BNC connectors. The IF amplifiers are located in the C-band radar control room and are easily accessible. The outputs from the sum channel and one of the auxiliary channels were used during MADOP testing.

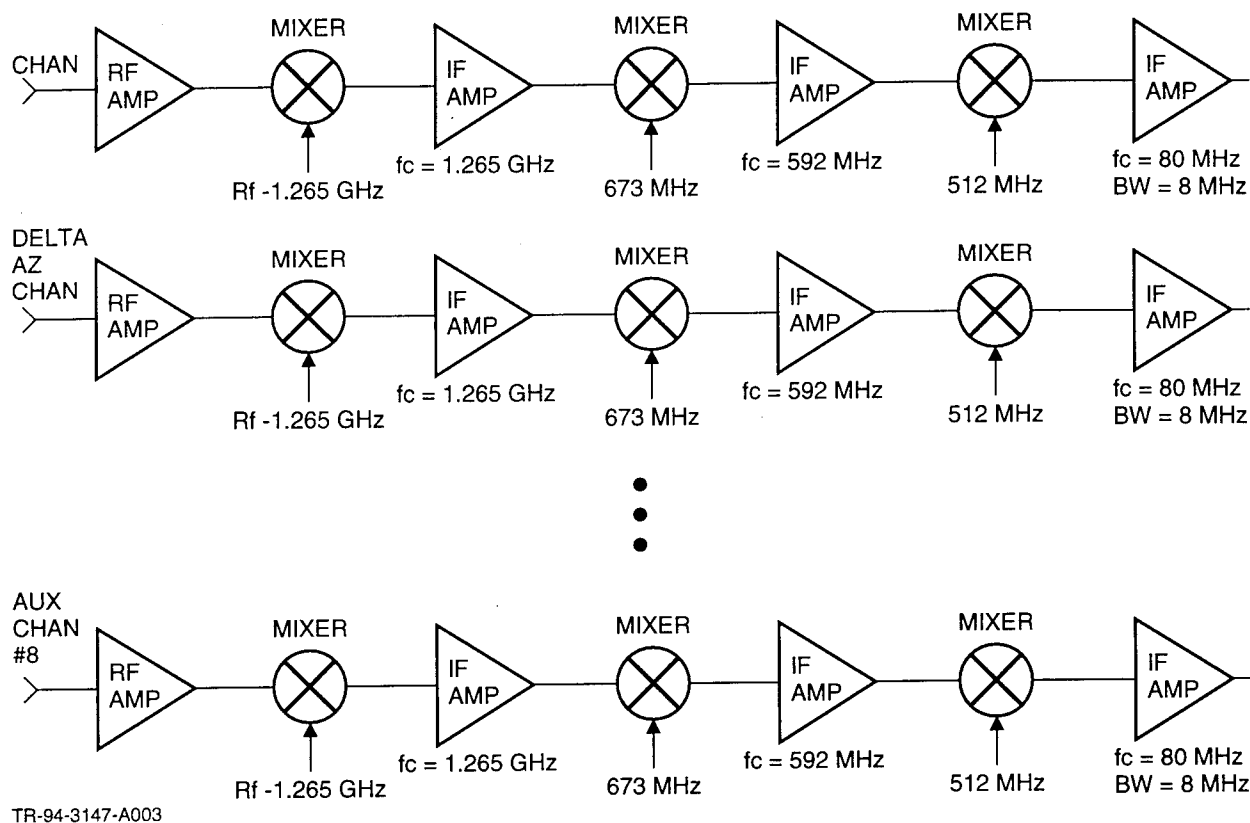


**Figure 4-26. C-Band Receiver Configuration**

The characteristics of the C-band radar were almost a perfect match for the MADOP. The radar has an IF of 80 MHz and a bandwidth of 8 MHz, both of which are approximately the design parameters of the MADOP. (In fact, the 80-MHz IF used in the MADOP was chosen with the thought of interfacing the MADOP to the C-band radar). The radar has the capability of supplying the main and auxiliary channels that would be needed by the MADOP, and these signals are easily accessible. Also, the C-band control room had space to accommodate the MADOP and the prime power needed to drive it.

There are two remote test signal sources associated with the C-band radar that can be used to generate the target and jammer signals that are needed to test the MADOP. These sources can be independently controlled and are able to generate CW, pulsed, and noise signals. The sources are located about 6500 ft from the radar and are separated by about 65 ft (see **Figure 4-27**). This provides an azimuth angular separation of about  $0.58^\circ$ . The sources are controlled from the C-band radar control room and can be synchronized with the radar timing signals.

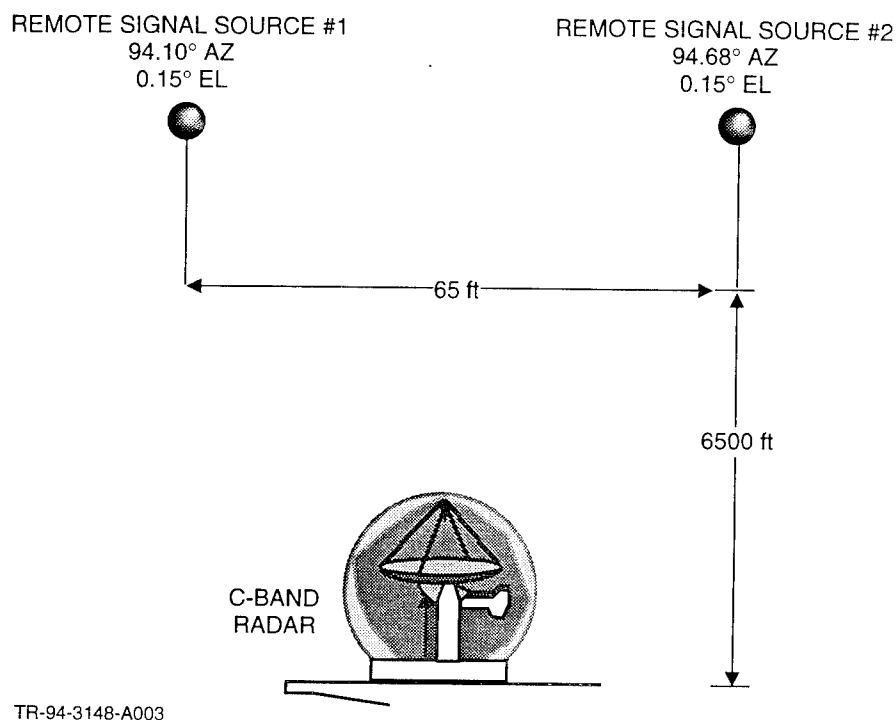
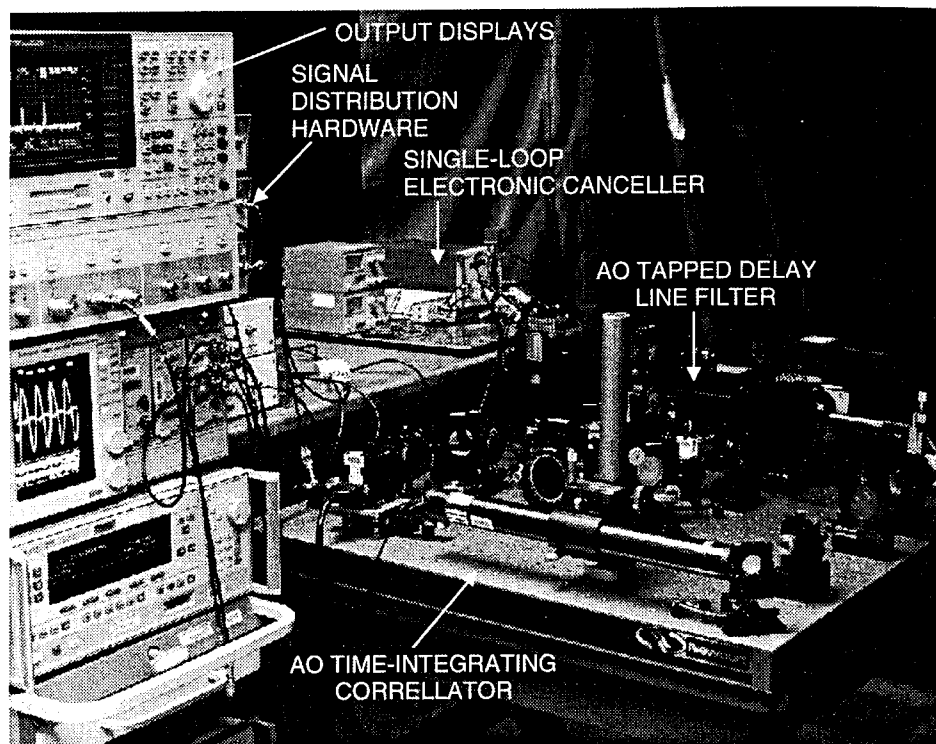


**Figure 4-27. Remote Signal Source Configuration**

### 4.3 C-BAND RADAR TESTBED MADOP TESTING

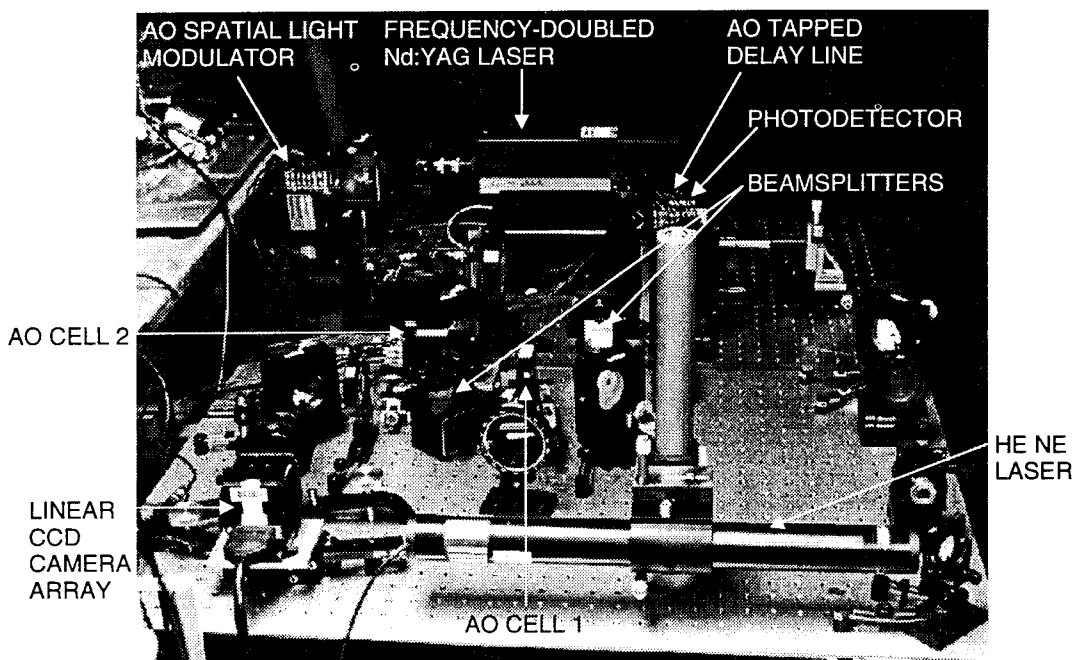
The actual testing of the MADOP with the C-band radar was conducted during the second week of the August onsite support trip (see **Figures 4-28 and 4-29**). Four sets of tests were performed. The tests were aimed at progressing from the controlled laboratory tests of previous onsite support trips to the case where the C-band radar provided the sole source of signals for the MADOP.

A block diagram of the configuration of the MADOP for the first three sets of tests is shown in **Figure 4-30**. In the first three sets of tests the C-band radar simply provided the jamming signal via the sum channel. The target signal was generated by a LeCroy AFG and the main and auxiliary channels for the MADOP were artificially derived using splitters and combiners, as with previous laboratory tests.



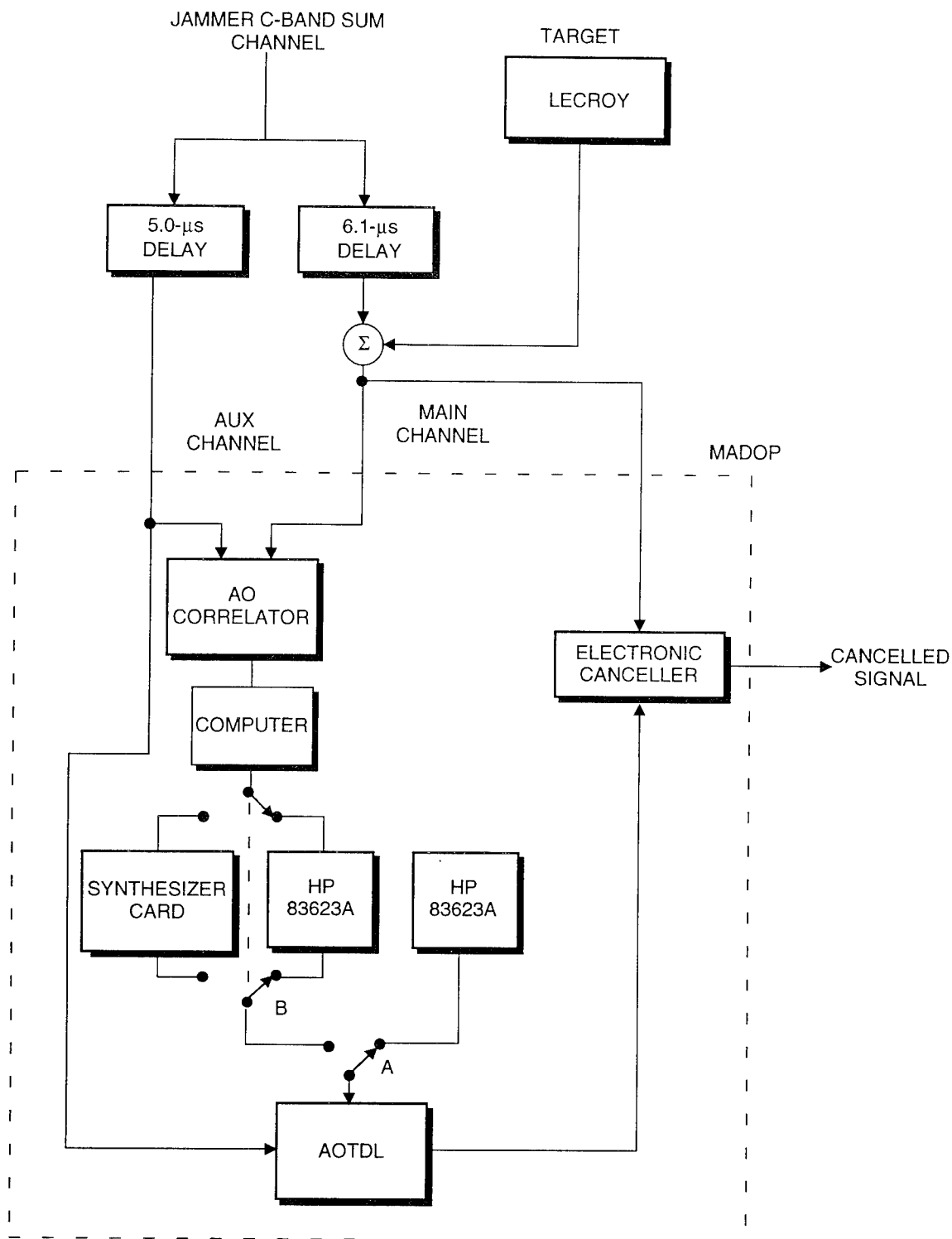
TR-95-0327-A003

*Figure 4-28. MADOP Integration With C-Band Test Radar*



TR-95-0326-A003

*Figure 4-29. MADOP AO Subsystems at the C-Band Radar Test Facility*



TR-94-3149-A003

**Figure 4-30. MADOP Configuration Used During First Three Sets of Tests**

Note that there is a switch labeled A and two switches labeled B in **Figure 4-30**. These are used to indicate the first three test configurations used. In the first configuration, switch A is to the right indicating that the HP 83623A signal generator is used to set the taps of the AOTDL. This is a manual mode of operation and was used to determine if the AOTDL and electronic canceller were cancelling the jammer when the AOTDL was properly set. This configuration essentially removed the AO time-integrating correlator and the computer from the cancellation operation.

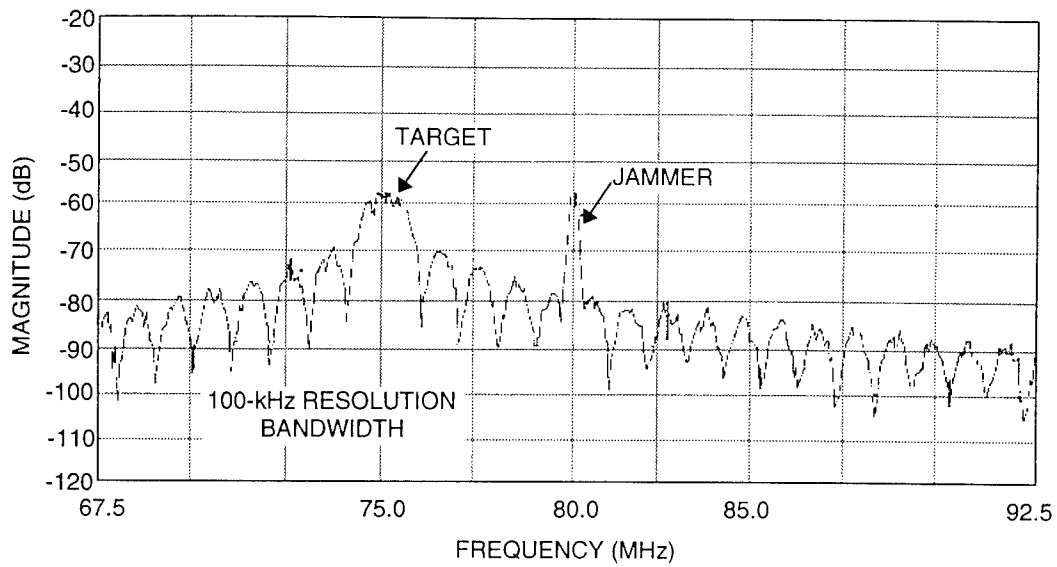
The results of the first set of tests are shown in **Figures 4-31 (a) and (b)**. In these figures, the jamming signal is a tone and the target signal is a 1- $\mu$ s pulse. The jammer is located at 80 MHz and the pulse is located at 75 MHz. This is not a realistic frequency separation but was chosen so that the target and jammer could be easily distinguished.

In the main channel signal the peak of the jamming signal spectrum is about 20 dB larger than the peak of the target signal spectrum. For discussion purposes we will say that this represents a S/J ratio of -20 dB\*. For the cancelled signal, the peak of the jamming signal spectrum is about 12 dB below the peak of the target signal spectrum. This means that the MADOP provided about 32 dB of S/J improvement for this case. This value of S/J improvement is consistent with the results obtained in the laboratory for tone types of jammers, and indicated that the AOTDL was working as it should.

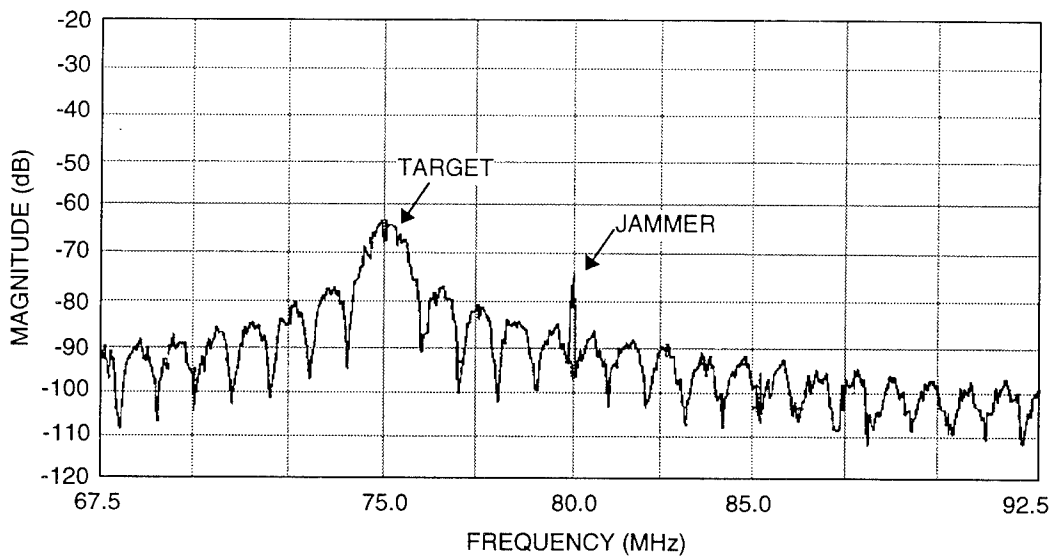
For the second set of tests, switch A of **Figure 4-30** was set to the left so that the AOTDL tap is now set by the output of the AO time-integrating correlator and the peak picking algorithm in the computer. Originally, the tests were to be run with switch B in the left position so that the frequency synthesizer in the computer was generating the frequency that was used to set the location of the AOTDL tap. However, we had problems cancelling the jammer signal. These problems were eventually traced to a bad channel on the frequency synthesizer card in the computer. In particular, the frequency synthesizer waveform was distorted, which was creating excessive harmonic energy. This, in turn, caused the AOTDL to use multiple delays when, in fact, it should have been using only one delay. The improper use of multiple taps caused the cancellation signal to differ considerably from the jamming signal and inhibited the jamming cancellation.

---

\*The difference in peaks is not a true measure of S/J since the latter is supposed to be a ratio of powers and the peaks of the spectra do not have the units of power; they have, in this case, the units of power in a 100-kHz bandwidth (the resolution bandwidth the spectrum analyzer was set to for the tests). To find true S/J, one would have to determine the total power in the pulsed and tone signals. This could be done from the spectrum analyzer data. However, such a calculation is not necessary as long as S/J is consistently defined among the various plots.



(a) Main Channel Signal Spectrum



(b) Cancelled Signal Spectrum

TR-94-3151-A003

**Figure 4-31. Results From the First Set of C-Band Radar Tests - Tone Jammer, Pulse Target, Open Loop Control Via HP 83623A**

To circumvent the problem, the synthesizer card had to be reconfigured so that the alternate channel was used. This change required that Capt. Andrews modify the computer software. While waiting for the modifications, the HP 83623A synthesizer was connected to the computer via an GPIB cable so that the computer was now controlling the frequency and amplitude of the HP 83623A synthesizer. The output of the synthesizer was, in turn, connected to the AOTDL. Referring to **Figure 4-30**, this resulted in the second set of tests being run with switch B in the right position.

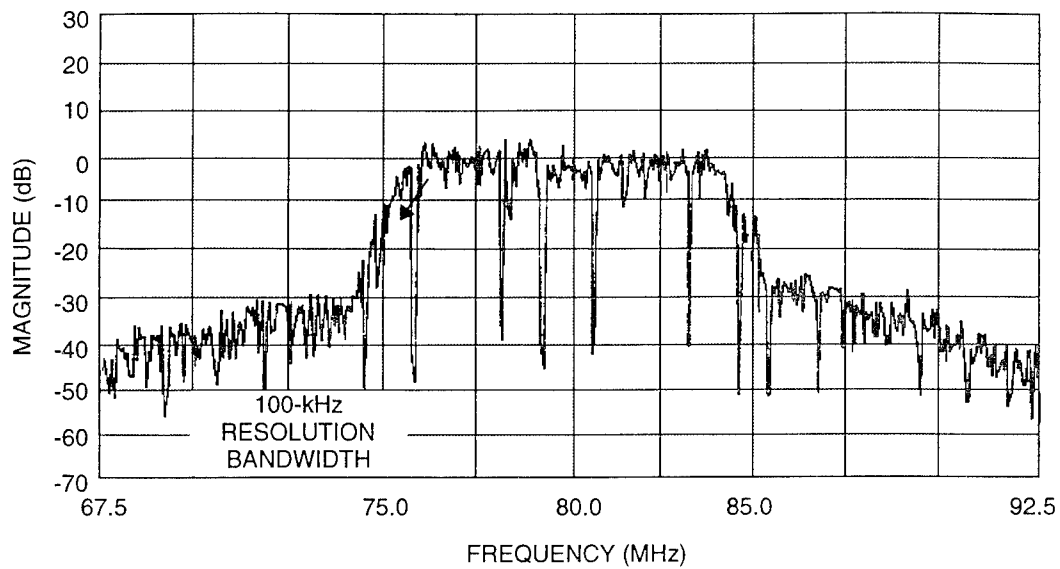
A sample of the results of the second set of tests is shown in **Figure 4-32**. The top plot on this figure is the main channel signal spectrum for the case of a noise jammer. A target signal was not used during the second set of tests. The bottom plot is the spectrum of the cancelled signal output of the MADOP. It will be noted that the level of the cancelled signal is 17 to 18 dB lower than the level of the main channel signal, indicating a jammer cancellation of about 17 dB. This, as expected, is worse than the jammer cancellation for a tone. However, it is still very good.

The shaping of the spectrum in the top plot is caused by the pass band of the C-band radar receiver and is indicative of the 8 MHz receiver bandwidth that the radar is supposed to have. The dips in both plots are due to T/R switch transients. Preliminary indications are that these may affect performance of the MADOP because of problems they cause in the correlation process. However, this needs to be further investigated. There is also a need to investigate the possibility of eliminating the effects of T/R switch transients.

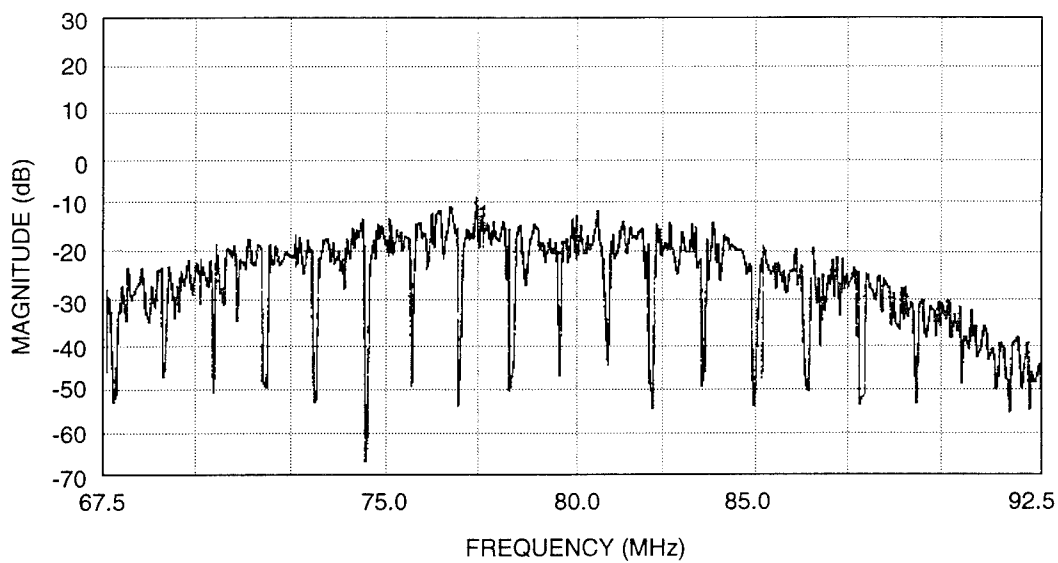
After Capt. Andrews modified the computer software to enable the alternate channel on the frequency synthesizer card, the MADOP was reconfigured to use the synthesizer in the computer. The resulting configuration is shown in **Figure 4-30** with switch B in the left position.

Sample results of the third set of tests are contained in **Figures 4-33 and 4-34**. As with the second set of results, these tests were run without a target signal.

In **Figure 4-33** the jammer is a tone at 80 MHz. The top plot is the spectrum of the main channel signal and the bottom plot is the spectrum of the cancelled signal out of the MADOP. It will be noted that, in this case, the MADOP provides about 25 dB of jammer cancellation. This is not as good as was obtained in the laboratory or with the first set of tests, however it is still reasonable.



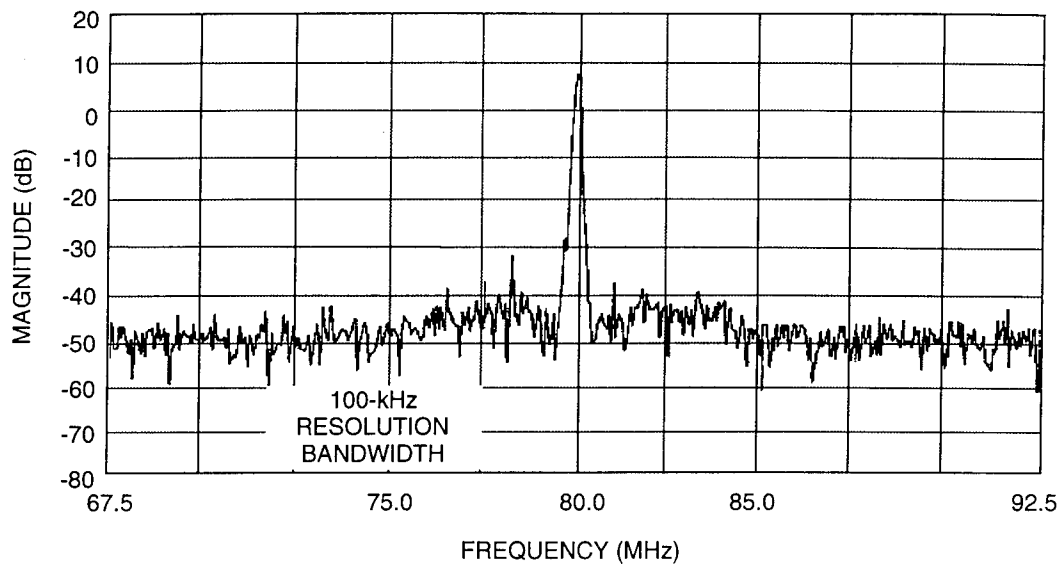
(a) Main Channel Signal Spectrum



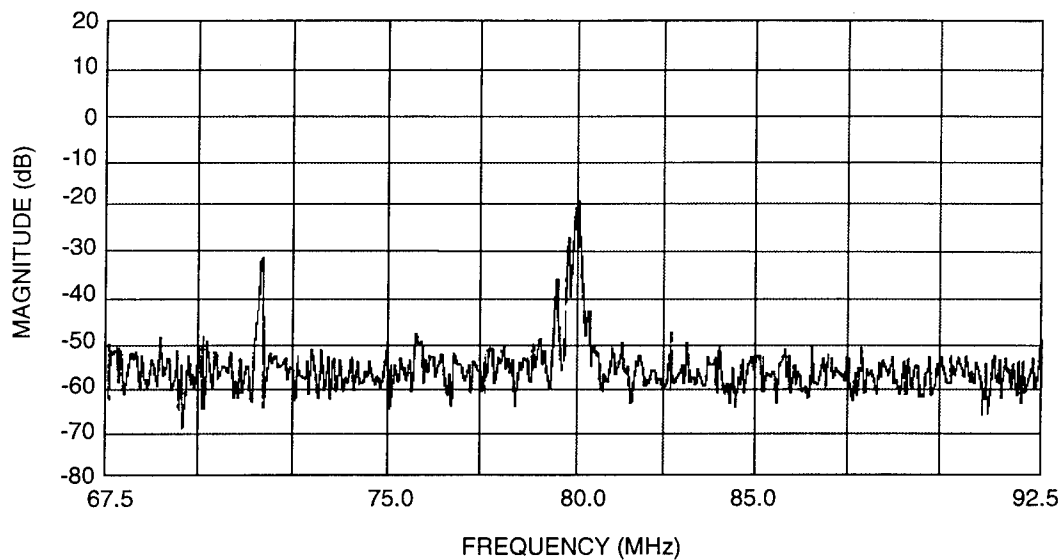
(b) Cancelled Signal Spectrum

TR-94-3152-A003

**Figure 4-32. Results From the Second Set of C-Band Radar Tests - Noise Jammer, No Target, Closed Loop Through HP 83623A**



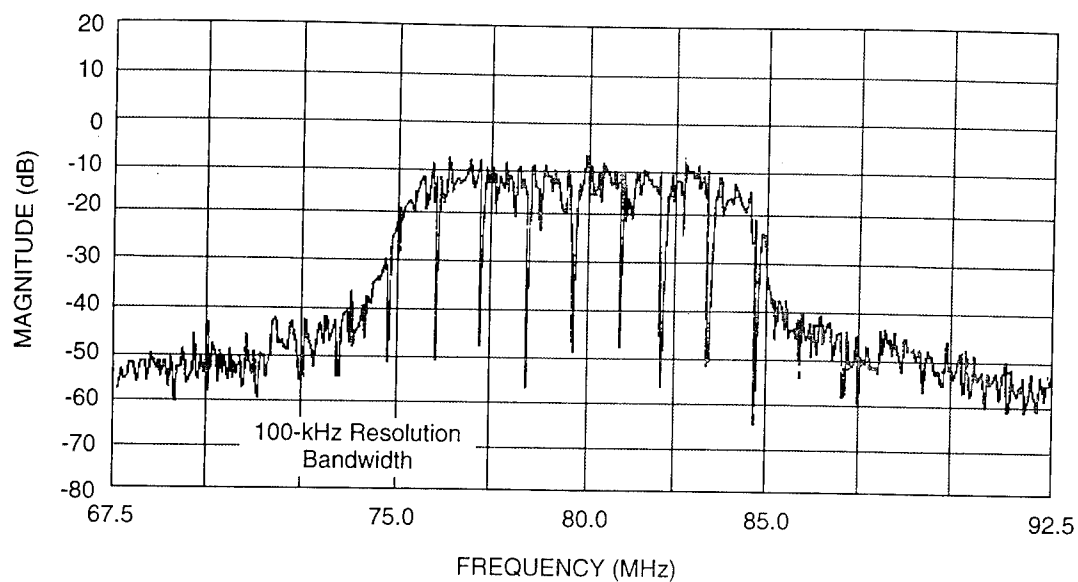
(a) Main Channel Signal Spectrum



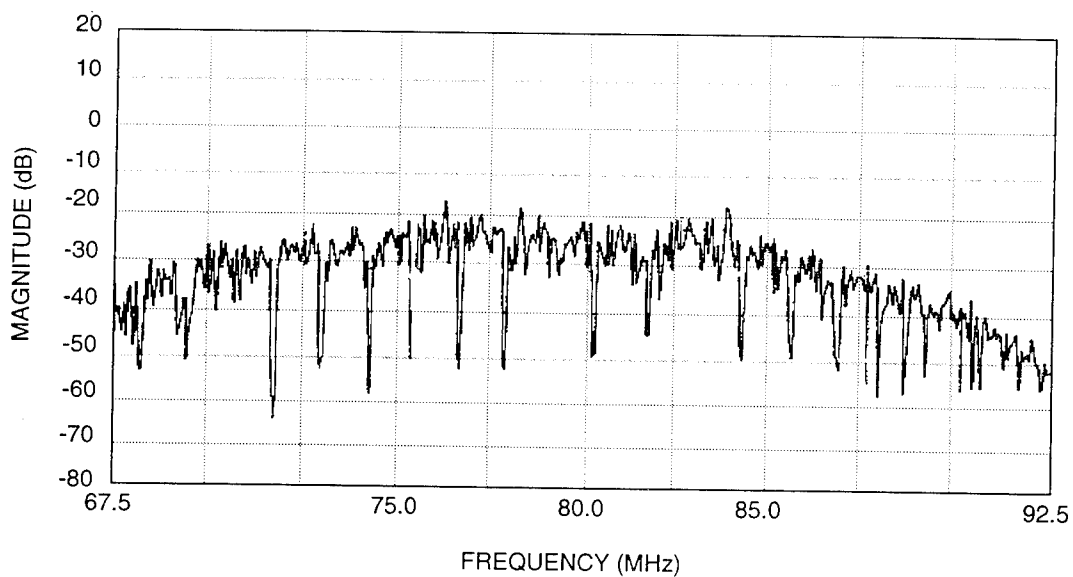
(b) Cancelled Signal Spectrum

TR-94-3154-A003

**Figure 4-33. Results From the Third Set of C-Band Radar Tests - Tone Jammer, No Target , Closed Loop Through Synthesizer in Computer**



(a) Main Channel Signal Spectrum



(b) Cancelled Signal Spectrum

TR-94-3156-A003

**Figure 4-34. Results From the Third Set of C-Band Radar Tests - Noise Jammer, No Target, Closed Loop Through Synthesizer in Computer**

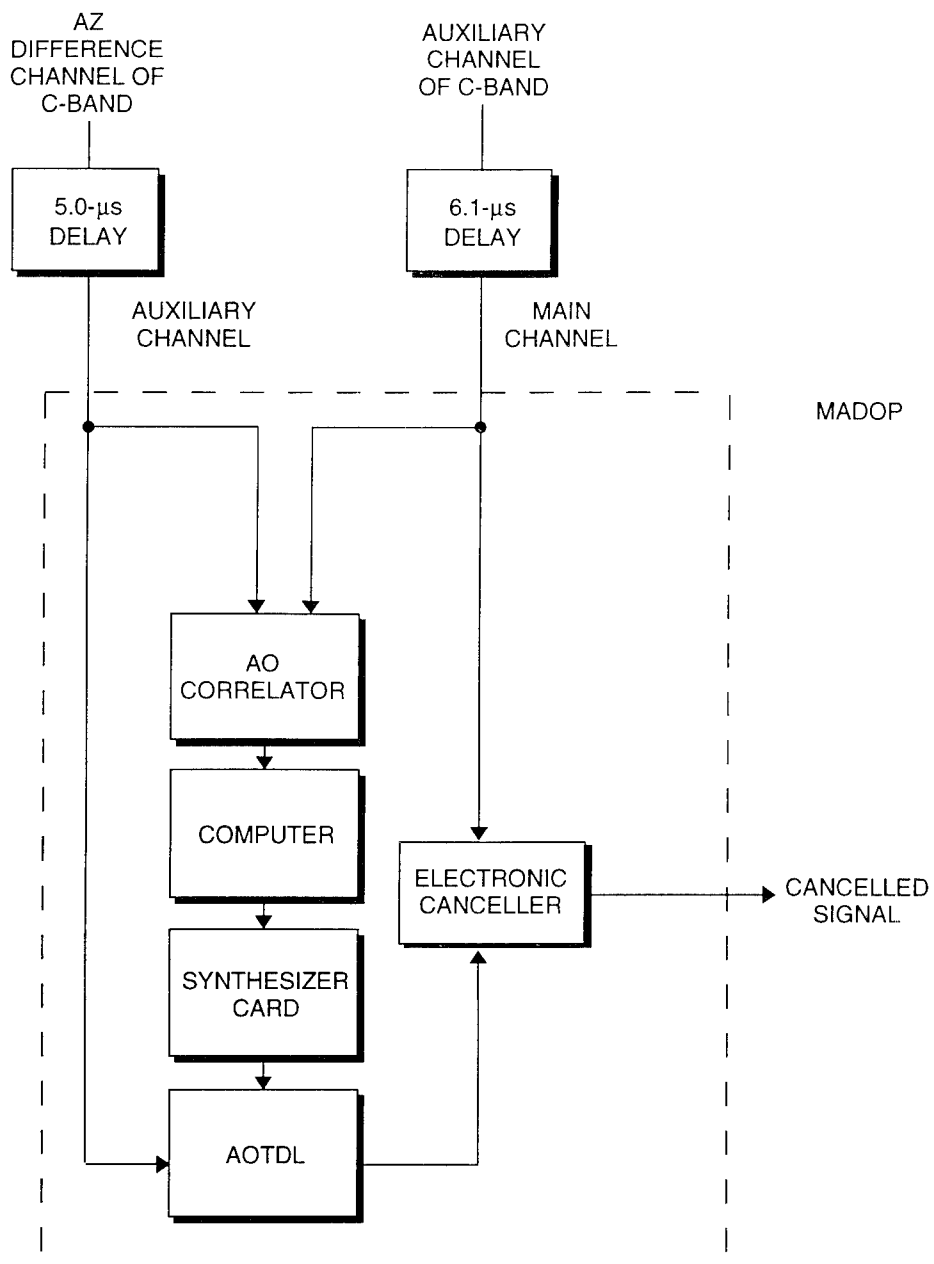
We believe that the decrease in cancellation for the third set of tests is due to the fact that the alternate channel of the computer synthesizer still produces distorted waveforms. We think that this distortion is also the cause of the distorted output spectrum shown in the bottom plot.

In *Figure 4-34* the jammer is noise. As with previous results, the top plot is the spectrum of the main channel signal and the bottom plot is the spectrum of the cancelled signal out of the MADOP. In this case the spectrum of the cancelled signal is 17 to 18 dB below the main channel signal, indicating a jammer cancellation of about 17 dB. This is consistent with the results obtained in the second set of tests. As with the second set of tests, the shape of the spectrum is a result of the C-band radar pass band characteristics, and the dips in the spectrum are believed to be due to the T/R switch.

A block diagram of the configuration that was used for the fourth set of tests is shown in *Figure 4-35*. A significant point of this configuration is that both the main and auxiliary channels of the MADOP are obtained directly from the C-band radar. They are not artificially generated as in the first three sets of tests. Another significant point is that the target signal is not artificially generated by laboratory test equipment. Rather, one of the two test sources is used to generate the target signal.

Because of the close proximity of the test sources to each other, the main and auxiliary channels of the MADOP had to be obtained from the C-band radar in an unusual manner. In normal operation, the main channel of the MADOP would be derived from the sum channel of the radar, and the auxiliary channel would be derived from the auxiliary channel of the radar. Also, in normal operation, we require that the S/J in the auxiliary channel be much less than one (less than zero, in dB), and less than the S/J in the main channel.

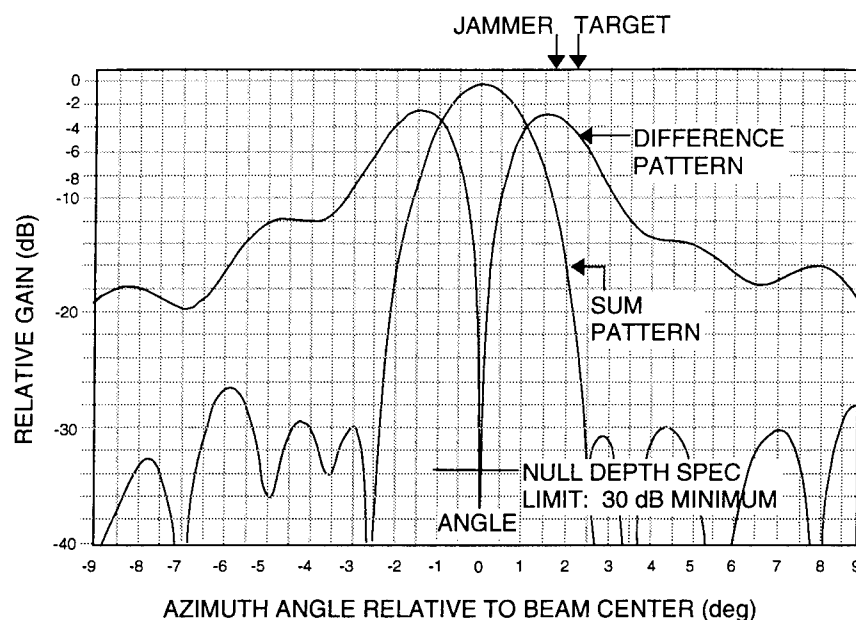
The angular spacing between the test sources is only  $0.58^\circ$  (see *Figure 4-27*), which is much less than the  $1^\circ$  azimuth beamwidth of the antenna. Because of this, both test sources will be in the main beam and experience about the same antenna gain, assuming the antenna is pointing at one of the sources. This means that the S/J will be essentially the same in the sum channel and the auxiliary channel. Although this is theoretically permissible, it is not practical for this application because it was found that measurements could not be obtained that would indicate how well jamming cancellation was being achieved with the available test equipment.



TR-94-3158-A003

**Figure 4-35. MADOP Configuration Used During Fourth Set of Tests**

To circumvent this problem we had to reverse the roles of the radar channels as related to the main and auxiliary channels of the MADOP. Specifically, we connected the output of the radar's azimuth difference channel to the auxiliary channel of the MADOP and the radar's auxiliary channel to the main channel of the MADOP. We then offset the antenna in azimuth so that both test sources were on the skirts of the sum beam, rather than in the center (see **Figure 4-36**). By offsetting the beam, about 10 dB of attenuation was achieved on the source termed the jammer and 20 dB of attenuation on the source termed the target (see **Figure 4-36**). This provided about -10 dB of S/J in the auxiliary channel of the MADOP. We further reduced this S/J by increasing the power of the jammer source so that it was about 13 dB above the power of the target source. Thus, the ultimate S/J in the auxiliary channel of the MADOP was about -23 dB. While this was less than desired, it was large enough for the MADOP to be able to cancel the jammer without seriously degrading the target signal.



TR-94-3159-A003

**Figure 4-36. C-Band Radar Azimuth Antenna Patterns**

The antenna gain of the auxiliary channel of the radar is approximately -9 dB, relative to the sum channel gain, so that the target and jammer signals in the MADOP main channel undergo approximately the same attenuation of about 9 dB, relative to the peak of the antenna sum beam. This means that the S/J in the main channel of the MADOP is about -13 dB. The power of the jammer was adjusted to be about 13 dB above that of the target.

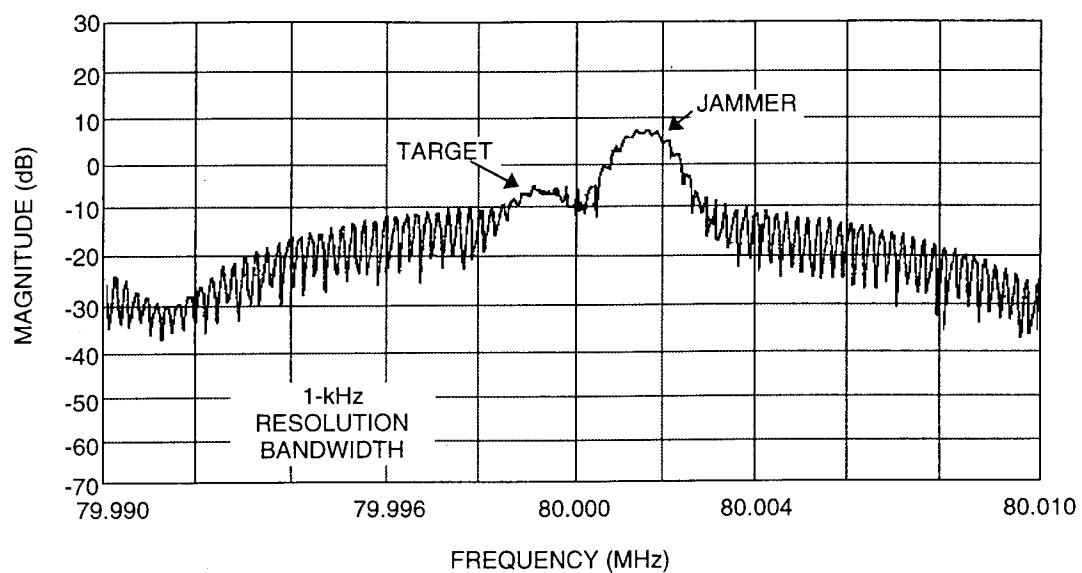
With the above, the desired conditions for the experiment were obtained. Specifically, the main channel of the MADOP contained both target and jammer signals with the jammer being about 13 dB larger than the target. This set of relative levels made it possible to discern both the target and jammer in the spectrum of the main channel of the MADOP. The S/J in the auxiliary channel of the MADOP was about -23 dB. This meant that the target signal could not be seen in the spectrum display of the auxiliary channel of the MADOP.

Two sets of data were recorded during the fourth set of tests. In the first, both the target and the jammer were tones; however, the tones were separated by 2 kHz. The spectra obtained during this test are shown in **Figure 4-37**. The top plot is the spectrum of the signal in the main channel of the MADOP, the center plot is the spectrum of the signal in the auxiliary channel of the MADOP, and the bottom plot is the spectrum of the cancelled signal out of the MADOP. The center vertical grid line of the plot is at a frequency of 79.996 MHz, and the spacing between vertical grid lines is 2 kHz. The spacing between horizontal grid lines is 2 kHz. The resolution bandwidth of the plot is 1 kHz.

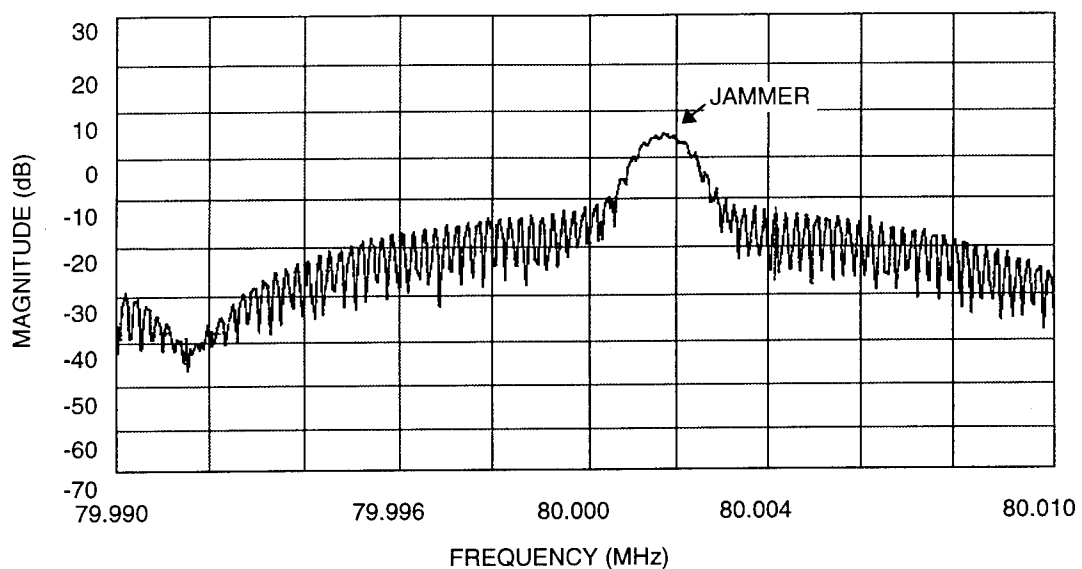
In the main channel, the jammer is about 13 dB larger than the target, whereas, in the cancelled signal the target is about 13 dB larger than the jammer. This means that the MADOP has provided a S/J improvement of about 26 dB. This S/J improvement is a little less than was obtained on previous tests with tone jammers. It is believed that the degradation is due to the fact that the S/J in the auxiliary channel of the MADOP is not as low as desired. This means that there will be some residual target signal in the signal out of the AOTDL. This, in turn, means that the MADOP is allowing some cancellation of the target signal, in addition to the jamming signal.

In the second set of test results the jammer signal is noise and the target signal is a pulse with a width of 1  $\mu$ s. The spectra for this case are shown in **Figure 4-38**. The top plot is the spectrum of main channel signal of the MADOP, and the bottom plot is the spectrum of the cancelled signal. The parameters of this plot are the same as for all of the previous plots except **Figure 4-37**.

In the top plot the target signal is barely discernible in the main channel signal. It is estimated that the peak of the target spectrum is 1 or 2 dB above the level of the jammer spectrum. In the cancelled signal, the peak of the target spectrum is about 15 dB above the level of the jammer spectrum. Thus, the S/J improvement for this case is about 13 dB. This is, again, a little less than in previous cases where the jammer was noise. As with the case of tones, it is believed that the poor S/J improvement is due to the fact that the S/J in the auxiliary channel of the MADOP is not as low as desired.



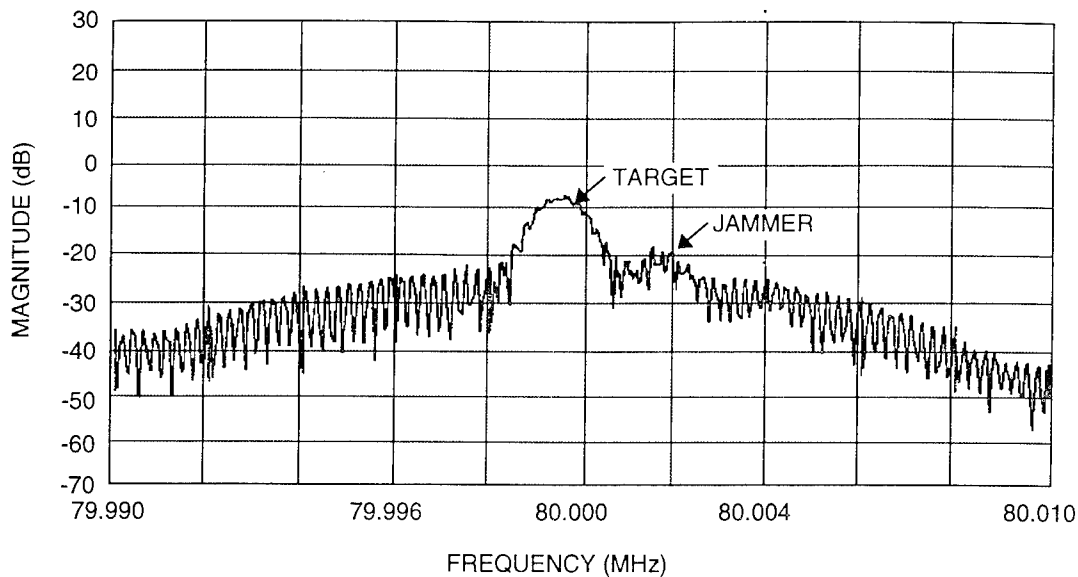
(a) Main Channel Signal Spectrum



(b) Auxiliary Channel Signal Spectrum

TR-94-3160-A003

**Figure 4-37. Results From the Fourth Set of C-Band Radar Tests - Tone Jammer, Tone Target, Both Signals From C-Band Radar**



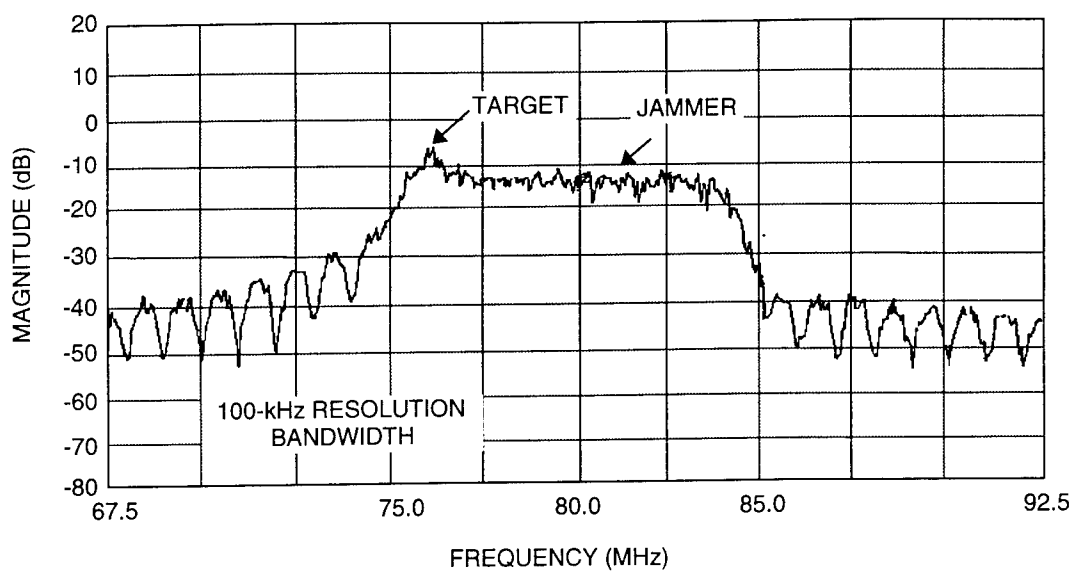
(c) Cancelled Signal Spectrum

TR-94-3162-A003

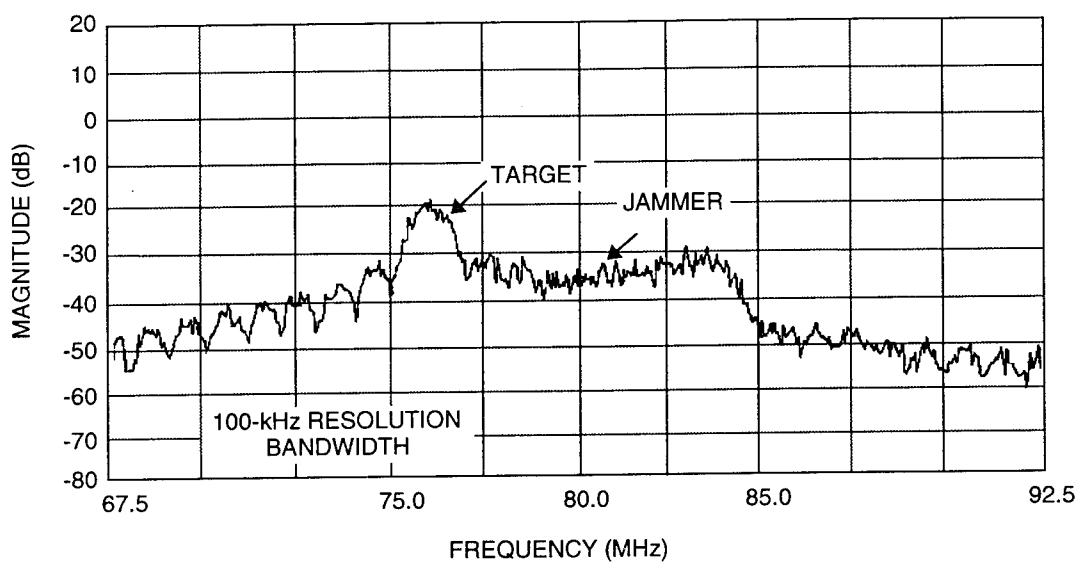
**Figure 4-37. Results From the Fourth Set of C-Band Radar Tests - Tone Jammer, Tone Target, Both Signals From C-Band Radar**

It will be noted that the dips due to T/R switching do not appear to be present in the spectra of **Figure 4-38**. The reason for this is also unknown.

Overall, the results of the first attempt to integrate and test the MADOP in the C-band radar were very encouraging. The MADOP generally achieved good cancellation of the jammer and appeared to function well throughout the test. The only significant problem encountered was with the frequency synthesizer in the computer, which tended to generate distorted waveforms.



(a) Main Channel Signal Spectrum



(b) Cancelled Signal Spectrum

TR-94-3163-A003

**Figure 4-38. Results From the Fourth Set of C-Band Radar Tests - Noise Jammer, Pulse Target, Both Signals From C-Band Radar**

## **5. CONCLUSIONS AND RECOMMENDATIONS**

All of the key objectives for this 1-year ESE program were successfully achieved, culminating in the demonstration of the MADOP within the C-band radar testbed. The prospects for further improvement are strong, given the significant progress made during this effort.

Results to date have demonstrated approximately 15- to 20-dB cancellation of wideband jamming interference and 25- to 35-dB cancellation of narrowband jamming. This performance was demonstrated in both the laboratory during the first two onsite support periods, and integrated with the C-band radar testbed during the third period of onsite support.

It is recommended that follow-on activities be partitioned into three primary technical areas corresponding to each of the specific subsections below. In order to extend the performance capability of the MADOP and continue to demonstrate this processor within the C-band radar testbed or other RL testbed, the three major tasks to be accomplished include concept evaluation in realistic jammer scenarios, MADOP hardware improvements, and further testing of the MADOP in a phased array radar, as detailed in Subsections 5.1, 5.2, and 5.3, respectively.

### **5.1 CONCEPT EVALUATION IN REALISTIC JAMMER SCENARIOS**

It is recommended that this activity be pursued to continue to evaluate the MADOP algorithm performance in realistic jamming environments using computer simulation. This will further detail the analysis of the MADOP algorithm as described in Section 2 of this report. Parameters that drive these simulations should be based on the measured and achievable MADOP performance and on the specific parameters of the radar selected for MADOP insertion.

Results of this concept evaluation should drive further improvements to the MADOP and its electronic interfaces, including: 1) the possible use of multiple MADOP systems in an IIR filter configuration, as described in Section 2 of this report; 2) the development of digital interface algorithms to more effectively select the filter tap weighting functions; 3) requirements for weight update time as a function of jammer environment; and 4) the possible benefits and limitations of using discrete tap weighting schemes using vertical cavity surface emitting laser (VCSEL) arrays (see Subsection 5.2 below).

### **5.2 MADOP HARDWARE IMPROVEMENTS**

As part of the on-going MADOP hardware improvements, there are several activities that should be pursued. They include: 1) the design, development, and integration of an in-line correlator

to the MADOP for increased stability; 2) analysis of VCSEL arrays as applicable to the AOTDL filter subsystem; and 3) improvements in the MADOP electronics. The specific subtasks are further detailed in the following subsections.

In order to increase the overall stability of the MADOP system and to reduce the complexity of the optical correlator system, a multichannel in-line (multiplicative) AO correlator should be inserted into the MADOP system. The existing MADOP AO correlator is based on a two-path (additive) architecture and is therefore very sensitive to mechanical vibrations and temperature gradients. After fabrication, this system should be characterized in terms of dynamic range, stability, and size. Other desirable improvements for the AO correlator include the insertion of a new linear CCD camera for the signal integration. Desirable characteristics include low electrical noise, high dynamic range, high readout rates, and user-friendly readout capability (i.e., analog output port for easy output viewing).

Having demonstrated the capability to cancel a jammer in the C-band radar testbed, it is desirable to study the extension of this capability to multiple jammers by investigating the use of laser diode arrays to provide multiple, independently addressable inputs to the AOTDL filter. This will capitalize on work already initiated by RL, and may also benefit from Dynetics' experience in developing the Continuously Variable Delay Line product (References 11 and 12). This approach provides potential for achieving faster system speed, which is currently limited by the electronic interfaces. This should include the possible use of VCSEL arrays as a means of obtaining multiple, separately addressable inputs to the AOTDL filter.

The improvement of the single-loop electronic canceller circuit hardware and the digital weight calculation algorithms are also recommended. The electronic canceller should be modified to replace the current phase comparator and vector modulator, which appear to be limiting performance. The circuit should also be compacted to reduce cable lengths, and impedance should be matched to reduce the reflections and the frequency-dependent performance trends that are currently observed. Digital algorithms to determine the appropriate weights may include carrier demodulation and filtering prior to weight calculation to improve stability of the algorithms.

### **5.3 FURTHER TESTING OF THE MADOP IN A PHASED ARRAY RADAR**

One of the ultimate goals of this development is the integration and demonstration of the MADOP system in a phased array radar. This has, in part, been achieved during this ESE activity, but the scope of this testing can be greatly increased. The continued availability of the C-band radar testbed is uncertain at this time. However, plans for utilizing an alternative radar should be considered. This should include the following activities: 1) the development of a test plan that

clearly identifies the interfaces to the phased array radar, integration schedule, calibration procedures, specific testing to be performed, and the measures of performance to be used in evaluating the MADOP; 2) the integration of the MADOP into the phased array radar, including the development of any signal conditioning electronics necessary to provide an adequate interface between the MADOP and the radar; and 3) tests of the MADOP to include radar transmission/target tracking in the presence of narrowband and also wideband (8 MHz) multipath interference.

**APPENDIX A:**

**LISTING OF DATAPLOT MATLAB PROGRAM FOR CORRELATION  
TESTING**

```

%DATAPLOT
% Input is XL data file collected from 386 PC and converted to Mac file.

load mztst6.xls
mzdata=mztst6;

% "a"= fir filter based on "wideband" input file (wideband correlation at given
% spatial carrier.

a=abs(fft(fir1(511,[40/256,70/256])));

clg

% XL file contains raw detector data in column 1, and background illumination/
% AO cell information for each channel in columns 2 and 3.
% "y" performs background subtraction.

y=mzdata(1:512,1);
%y=mzdata(1:512,1)-mzdata(1:512,2)-mzdata(1:512,3);

%subplot(211)
%plot(y)

%subplot(212)

% Filter weighting application
%Y=a'.*fft(y);
Y=fft(y);

TEST=Y;
Y=abs(Y);
Y(1:5)=ones(5,1)*1e-6;
Y=Y/max(Y);
Y=20*log10(Y);

axis([1,512,-60,0]);
plot(Y),grid
axis;
pause

% SNR calculation based on "wideband" input file.

sig=real(ifft(TEST));
rms=std(sig(350:450));
maxsig=max(sig);
minsig=min(sig);
SNR=20*log10(maxsig/rms)
axis([1,512, minsig, maxsig]);
plot(sig);
axis;

```

**APPENDIX B:**  
**MATLAB SIMULATION OF THE ELECTRONIC CANCELLER**

```

% Program to check compensation loop for MADOP
% Feb 9, 1994 M. C. Budge, Jr.
n=500; %Number of steps in iteration
K=10; %loop gain
fr=1; fi=1; %Scale factors for unequal real and
           %Imaginary loop gains
li=30; lr=30; % Limits on real and imaginary control voltages Kr=K*fr; Ki=K*fi; %Real
and imaginary loop gains phierr=40; % phierr is the phase error in the correction
           % portion of the loop
k=[1:n]; %timer index
% AOTDL channel signals
Jamag=1.0; % AOTDL channel magnitude
Japh=180*pi/180; %AOTDL channel phase
Ja=Jamag*exp(j*Japh); %AOTDL signal
T=0.05/(K*Jamag^2)/2; %Sample spacing
t=T*(k-1); % time vector
% main channel signals
Jmmag=2.; % Main channel magnitude
Jmph=30*pi/180; % Main channel phase
Jm=Jmmag*exp(j*Jmph); %Main channel signal %
Set up plot arrays
voiqplt=zeros(k)+j*zeros(k); eplt=voiqplt;
% initialize loop parameters
voiqr=0; voiqi=0;
voiq=voiqr + j*voiqi;
% Main computation loop
for l=1:n
    Jd=voiq*Ja*exp(j*phierr*pi/180); % Phase shifted version of
           % AOTDL signal. phierr is
           % the phase error in the
           % phase correction part of
           % the loop.
    e=Jm-Jd; eplt(l)=e; %error signal
    viq=e*conj(Ja); %input to integrators - mixing of Ja and e
    voiqr=voiqr+Kr*T*real(viq); % real part of integrator output
           % control voltage
    voiqr=min(lr,max(voiqr,-lr)); % limited form of voiqr
    voiqi=voiqi+Ki*T*imag(viq); % imaginary part of integrator
           % output - control voltage
    voiqi=min(li,max(voiqi,-li)); % limited form of voiqi
    voiq=voiqr+j*voiqi; % put into complex form for later
    voiqplt(l)=voiq; % save for plotting
end
clg
subplot(221)
plot(t,abs(eplt))
xlabel('time (s)')
ylabel('error')
subplot(222)
plot(t,real(voiqplt))
xlabel('time (s)')
ylabel('R ctl volt')
subplot(223)
plot(t,imag(voiqplt))
xlabel('time (s)')
ylabel('I ctl volt')

```

```
subplot(224)
txt=['loop gains: Kr=',num2str(Kr),' Ki=']; txt=[txt,num2str(Ki)];
text(0.6,0.4,txt,'sc')
txt=['Control voltage limits: lr=',num2str(lr)]; txt=[txt,'
li=',num2str(li)]; text(0.6,0.35,txt,'sc')
txt=['phase error=',num2str(phierr),' deg'];
text(0.6,0.3,txt,'sc')
```

## **REFERENCES**

1. Berinato, R. J., M. C. Zari, and M. C. Budge, "Alternate Optical Architectures for Multichannel Adaptive Optical Processing," Dynetics, Inc., Final Technical Report, RL-TR-93-34, April 1993.
2. Budge, M. C., R. J. Berinato, and M. C. Zari, "Acousto-Optic Applications for Multichannel Optical Processor," Dynetics, Inc., Final Technical Report, RL-TR-92-160, June 1992.
3. Zari, M. C., R. J. Berinato, M. J. Ward, and H. G. Andrews, "Multichannel Optical Time-Integrating Correlator for Adaptive Jamming Cancellation," Advances in Optical Information Processing V, SPIE Proceedings Vol. 1704, Orlando, 1992.
4. Ward, M. J., C. W. Keefer, and S. T. Welstead, "Adaptive Optical Processor," In-house Report, RL-TR-91-270, August 1991.
5. Welstead, S. T. and M. J. Ward, "Hybrid Electro-Optic Processor," Final Technical Report, RL-TR-91-164, July 1991.
6. Welstead, S. T., "Optical Processor Evaluation," Final Technical Report, RL-TR-91-34, March 1991.
7. Ward, M. J., C. W. Keefer, D. J. Grucza, and S. T. Welstead, "Comparison of Spatial Light Modulators for Multipath Delay Estimation," OSA Technical Digest, Vol. 14, p. 149, 1990.
8. Mansour, D., and A. H. Gray, Jr., "Unconstrained Frequency Domain Adaptive Filter," IEEE Trans. Acoustics, Speech, and Signal Processing, Vol. ASSP-30, No. 5, October 1982.
9. Cioffi, J. M., "The Block-Processing FTF Adaptive Algorithm," IEEE Trans. Acoustics, Speech, and Signal Processing, Vol. ASSP-34, No. 1, February 1986.
10. Shynk, J. J., "Frequency Domain and Multirate Adaptive Filtering," IEEE Signal Processing Magazine, p. 14, January 1992.
11. Anderson, C. S. and M. C. Zari, "Variable Delay Lines Offer Continuously Variable Range Selection for Radar Target Simulators," Microwave Journal, April 1994.
12. Anderson, C. S. and M. C. Zari, "Design and Characterization of a Long Time Aperture Acousto-Optic Delay Line," Optical Engineering, Vol. 34, No. 1, January 1995.

Rome Laboratory  
Customer Satisfaction Survey

RL-TR-\_\_\_\_\_

Please complete this survey, and mail to RL/IMPS,  
26 Electronic Pky, Griffiss AFB NY 13441-4514. Your assessment and  
feedback regarding this technical report will allow Rome Laboratory  
to have a vehicle to continuously improve our methods of research,  
publication, and customer satisfaction. Your assistance is greatly  
appreciated.

Thank You

\_\_\_\_\_  
\_\_\_\_\_  
Organization Name: \_\_\_\_\_ (Optional)

Organization POC: \_\_\_\_\_ (Optional)

Address: \_\_\_\_\_

1. On a scale of 1 to 5 how would you rate the technology  
developed under this research?

5-Extremely Useful      1-Not Useful/Wasteful

Rating \_\_\_\_\_

Please use the space below to comment on your rating. Please  
suggest improvements. Use the back of this sheet if necessary.

2. Do any specific areas of the report stand out as exceptional?

Yes \_\_\_ No \_\_\_\_\_

If yes, please identify the area(s), and comment on what  
aspects make them "stand out."

3. Do any specific areas of the report stand out as inferior?

Yes\_\_\_ No\_\_\_

If yes, please identify the area(s), and comment on what aspects make them "stand out."

4. Please utilize the space below to comment on any other aspects of the report. Comments on both technical content and reporting format are desired.

***MISSION  
OF  
ROME LABORATORY***

**Mission.** The mission of Rome Laboratory is to advance the science and technologies of command, control, communications and intelligence and to transition them into systems to meet customer needs. To achieve this, Rome Lab:

- a. Conducts vigorous research, development and test programs in all applicable technologies;
- b. Transitions technology to current and future systems to improve operational capability, readiness, and supportability;
- c. Provides a full range of technical support to Air Force Materiel Command product centers and other Air Force organizations;
- d. Promotes transfer of technology to the private sector;
- e. Maintains leading edge technological expertise in the areas of surveillance, communications, command and control, intelligence, reliability science, electro-magnetic technology, photonics, signal processing, and computational science.

The thrust areas of technical competence include: Surveillance, Communications, Command and Control, Intelligence, Signal Processing, Computer Science and Technology, Electromagnetic Technology, Photonics and Reliability Sciences.